PFC/RR-83-33 DOE/ET/51013-104

Safety and Protection for Large Scale Superconducting Magnets — FY1983 Report

by

R.J. Thome, J.M. Tarrh, R.D. Pillsbury, Jr., W.G. Langton, W.R. Mann, H. Becker, A. Hatch, P.G. Marston, Y. Iwasa, A.M. Dawson, J. Borzikowski, and T. Ishigohka
Plasma Fusion Center
Massachusetts Institute of Technology
Cambridge, MA. 02139

December 1983

Submitted to Idaho National Engineering Laboratory

TABLE OF CONTENTS

1.0 INTRODUCTION

R.J. Thome

The rapid increase in size, stored energy, and complexity of the magnet systems required for advanced energy conversion applications such as fusion demands a thorough understanding of safety and protection for personnel and other systems. Toward this end, MIT has been carrying out a program for INEL oriented toward safety and protection in large scale superconducting magnet systems. The program involves collection and analysis of information on actual magnet failures, analyses of general problems associated with safety and protection, and performance of safety oriented experiments. This report summarizes work performed in FY83.

In December 1982, a massive structural failure occurred in a large magnet at the Arnold Engineering Development Center (AEDC). The magnet utilized about 8.4×10^4 kg of copper conductor, 5.4×10^4 kg of aluminum structure, and 5×10^5 kg of steel in a flux return frame. The failure occurred at a field level of 4.1 T and led to brittle fractures in most of the structural components, significant displacements of some portions of the iron frame, and substantial deformation of the winding with some conductor fracture. Chapter 2 describes this system before and after failure and summarizes the structural failure analyses which were performed by MIT in parallel with the investigation by a team from AEDC.

The magnet failure was catastrophic in the sense that most structural components were fractured and the winding suffered extensive plastic deformation. However, operating procedures prevented possible injury to personnel and the rugged nature of the winding limited deformations to

large but safe values, and restrained conversion of magnetic to kinetic energy of failed components. This suggests that it may be desirable to limit operating current densities in magnet design to levels whereby the winding could act in this structurally fail-safe manner even if it sustained substantial deformation in the event of a failure in its primary structure. A general analysis of this problem was, therefore, performed and is presented in Chapter 3.

The model and examples in Chapter 3 are based on an infinitely long solenoid configuration. Although the geometry is simple, this shape allows the important parameters to become apparent. The preliminary conclusions are:

(a) A protective circuit reaction involving dissipation in resistive elements following a major structural failure is unlikely to be effective on a fast enough time scale to limit the mangetic to kinetic energy conversion process in magnets using high current density windings.

(b) Windings with low enough current densities can absorb the total load following structural failure, thus limiting the kinetic energy conversion process, although this might involve substantial yielding and deformation of the winding. This is not usually a design requirement, but might form the basis for one criteria for large magnet design.

(c) Protective circuits involving inductive energy transfer can respond fast enough to limit the kinetic energy conversion process in high or low current density configurations. The range of coupling coefficients and time constants to allow this method to be effective are under study. This is the source of our interest in the use of multiple circuits for discharge of a TF coil system as begun this year and as discussed in Chapter 4.

Chapter 3 closes with a simple model which illustrates the ability of an inductively coupled secondary circuit to be effective in restraining magnetic to kinetic energy conversion in the event of a structural failure in a primary circuit. In Chapter 4, the use of multiple circuits in a TF

coil system was studied since it presents a means for limiting another process, that is, the magnetic to thermal energy conversion in a superconducting winding in the event of a quench. Typically, results show that only a small fraction of the total energy needs to be removed if only one of k circuits is discharged because the bulk of the energy is retained by the (k-1) circuits which maintain constant flux throughout the transient. This procedure allows the first circuit to be discharged more rapidly for a given initial voltage and final temperature limit, thus allowing for a longer delay time before the dump is initiated or for operation at a higher current density. The remaining coils could then be discharged on a longer time scale. However, if the remaining circuits require rapid discharge shortly after the first, then the necessary voltage per coil may or may not be higher than that required for the first circuit depending on the discharge sequence, number of coils and aspect ratio. The voltage to ground can be considerably lower than if a single system circuit was used. The general criteria governing the different reactions will be developed further next year.

Chapter 5 describes the experimental activity under this program during FY83. This involved a continuation of earlier activity regarding measurements of arc extinction voltages between electrodes in 300 K and 4.2 K (Section 5.1). Section 5.2 describes a small "football" experiment involving internally cooled cable conductor. Because of delays in delivery of the conductor the test was not carried out in FY83 as planned, but will be performed in FY84 together with another small football test as originally planned for FY84. Section 5.3 gives an update on the hybrid magnet status at FBNML as a continuation of our interest in the short

circuit in the superconducting section of that system. In summary, the short persists, but has minimal impact on operations because of the well cooled, highly stable design of this coil. Other types of design could experience a much more serious impact.

The report closes with a summary of safety related activities partially supported by this program. In FY83 this included participation in a Fusion Safety Workshop in Japan and involved a presentation regarding programs in magnet safety in the United States, participation in workshop discussions on other fusion systems, and tours of the fusion facilities at JAERI.

2.0 HPDE MAGNET FAILURE

(Subject to review and update in FY84)

2.1 System Description and Summary - R.J. Thome and J.M. Tarrh

The High Performance Demonstration Experiment (HPDE) at the Arnold Engineering Development Center (AEDC) employed a large (active bore approximately 1 m square x 7 m long) iron-bound copper magnet designed to operate in either of two modes: (1) as a 3.7 T (continuous) water cooled magnet, or (2) as a 6 T (long pulse) nitrogen precooled, cryogenic magnet. In either mode, coolant would flow through conventional hollow copper conductor windings. A unique force containment structure of 2219 aluminum alloy was selected on the basis of thermal considerations (77 to 350 K operating temperature range; coefficient of thermal expansion permitting dimensional matching to the coil) and cost. In December 1982 a catastrophic structural failure occurred at a field level of 4.1 T which led to massive brittle fractures and failure of most of the structural components, significant displacements of some of the iron frame components, and substantial deformation of the winding with some conductor fracture. Although the failure occurred at a fraction of the design field level, no personnel injury occurred because of the operating procedures in force at the time of the incident which restricted personnel access and required operating personnel to be in a remote control area. At present, the structure is considered beyond repair. The windings are considered to be reparable without prohibitive time and effort assuming a reduced performance requirement (single mode, pulsed from room temperature).

Following the incident a detailed investigation was performed by AEDC personnel.[1] In parallel with this effort, MIT carried out a preliminary failure analysis which is summarized in Section 2.2. Although there is general agreement,

more than one failure scenario is possible from the standpoint of the early sequence of events. The evidence indicates a localized structural failure leading to sequential overloading and fracture of other structural components. The primary cause appears to have been design flaws relative to structural details and the load distribution in localized areas. A contributing factor was utilization of structural materials having low ductility. The conversion of the stored magnetic energy to kinetic energy of the fractured components was limited because of the large cross-section of the winding and the ability of the windings to deform to a configuration which could accept the magnetic loads while the coil discharged. This has led to the simplified modeling and analyses for magnets in general which is described in Chapter 3.0.

The remainder of this section will describe the system characteristics before and after failure. Section 2.2 will describe the failure analyses and summarize the fault scenarios. Further analyses of effects such as the deflection limiting nature of the clamping between components of the iron flux return frame will be carried out in FY84 together with a review of the preliminary failure analysis. This chapter, will therefore, be updated in our FY84 report.

The HPDE magnet utilized a saddle coil pair typical of an MHD experiment in which a magnetic field is required in a direction perpendicular to the axis of a long channel. The shape of the coils is shown in Fig. 2.1 which also indicates the direction and magnitude of the electromagnetic loads on the coils at the design field level. The scale of the device is indicated by Fig. 2.2 which shows the coils before addition of the aluminum structure or side and top

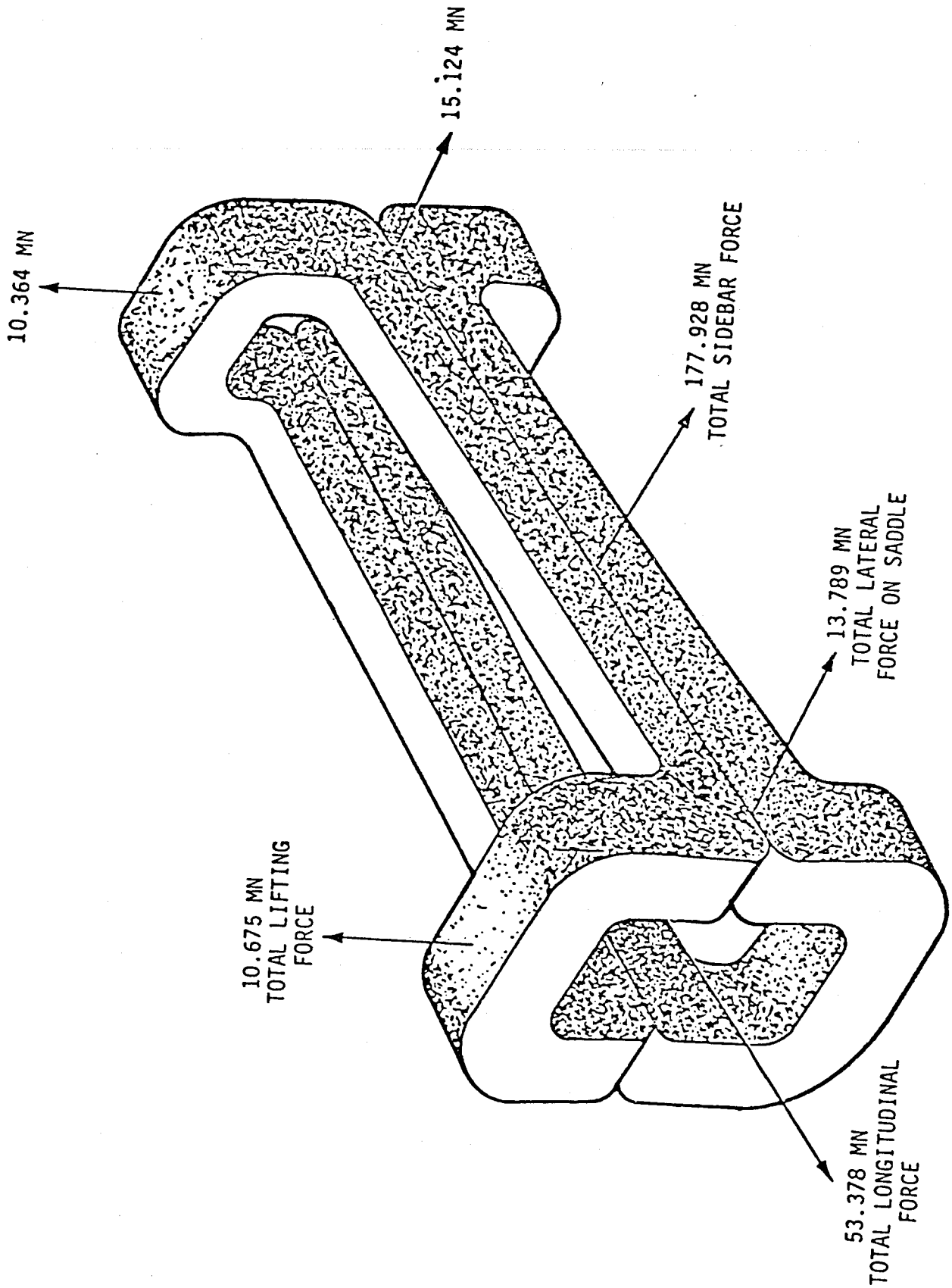

Figure 2.1 HPDE Saddle Magnet Coils

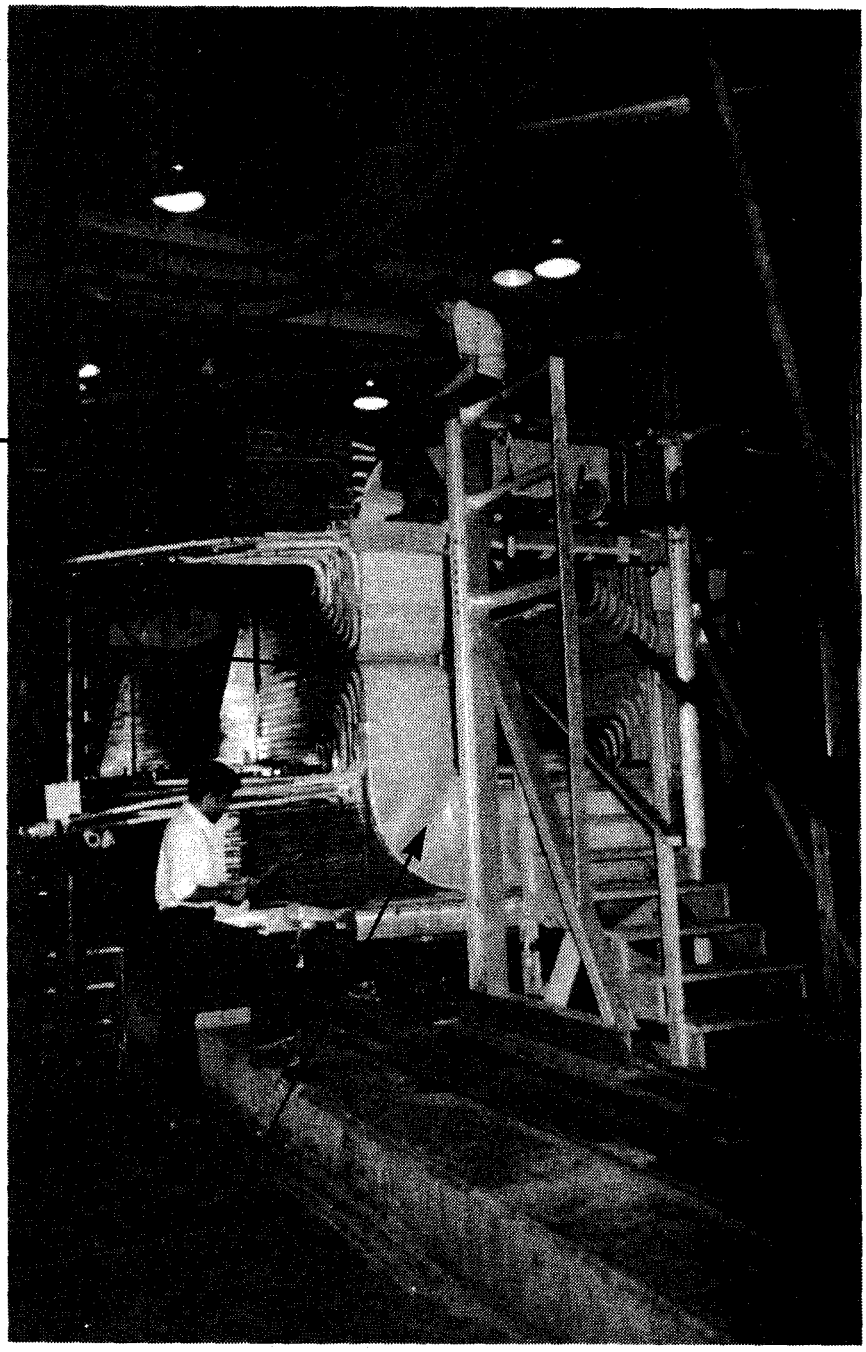

Figure 2.2 HPDE Magnet Coils before addition of structure or top and side components of iron flux return frame.

components of the iron flux return frame. The figure indicates the longitudinal section of the windings which lie parallel to the MHD channel axis and the end turns of the saddle coils which pass over and under the MHD channel (not shown).

The structure was composed of aluminum plates which enclosed the windings as shown in Fig. 2.3 and were primarily held in place by a system of keys and bolts. The "sidebar loads" in Fig. 2.1 were carried by the vertical beam modules on each side of the magnet. These modules were held in place by the transverse tension members. Near the ends of the coils, portions of this load were carried by the collars which were composed of four plates at each end, held together with keyed fingers.

The longitudinal forces in Fig. 2.1 were carried partly by the longitudinal windings but predominantly by the longitudinal tension members (LTM). These plates (having cross-sections of 1.0 x 0.13 m each) ran the length of the windings and had fingers at their ends which passed through the face plates to pick up a portion of the loads from the face plates. Figure 2.4 shows details of the fastening approach which uses keyblocks between the LTM fingers on the outside of the face plate. The fingers and keys between the collar components are also evident in this view. Analyses indicate that one or the other of these finger areas failed as the initiating event, followed by failure of the other area and subsequent sequential overload and failure of the transverse tension members and their connections to the vertical side beam modules along the entire length of the magnet. Table 2.1 summarizes the fractured structural components based on a visual inspection.

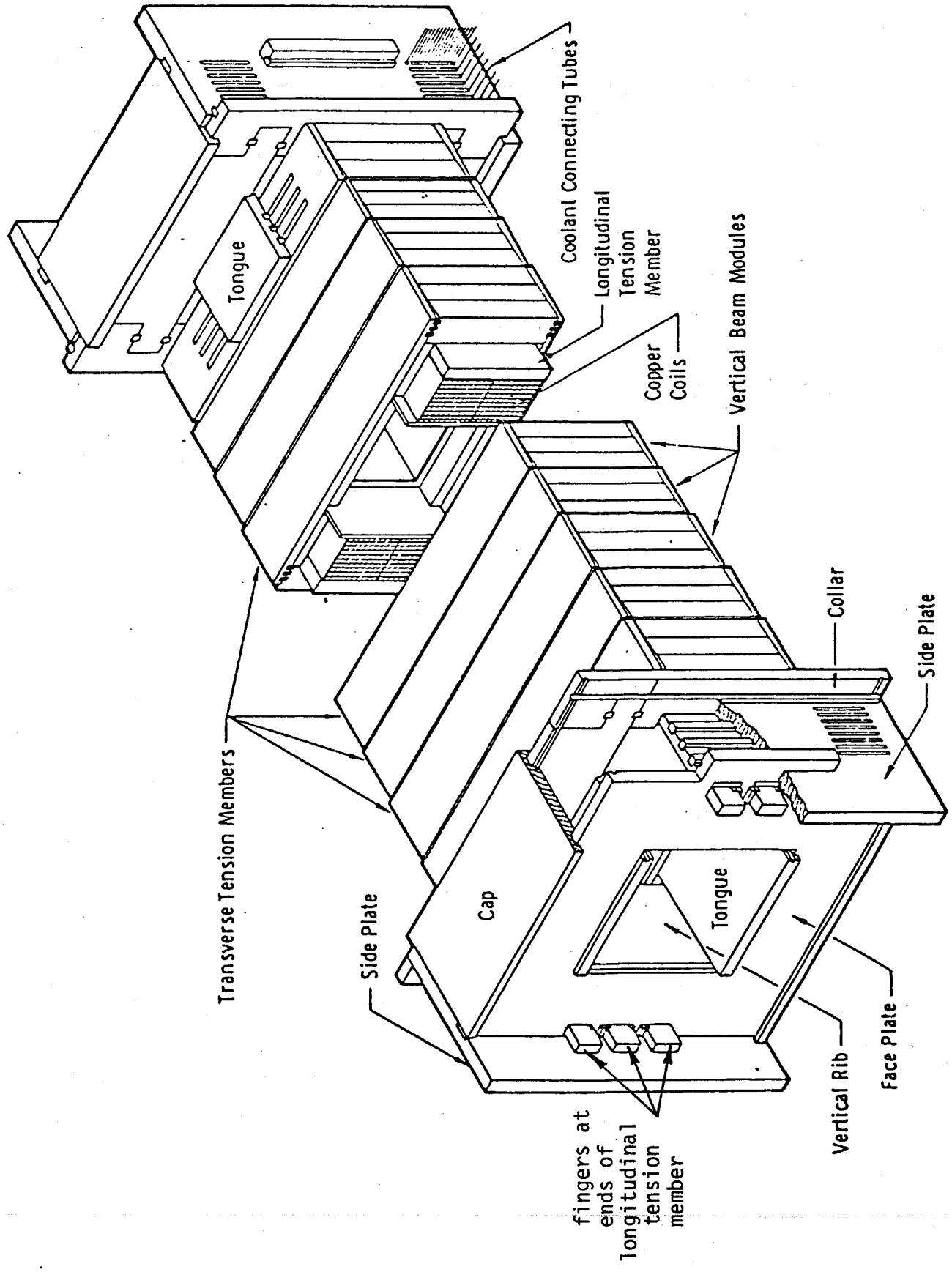

Figure 2.3 Aluminum Force Containment Structure (FCS)

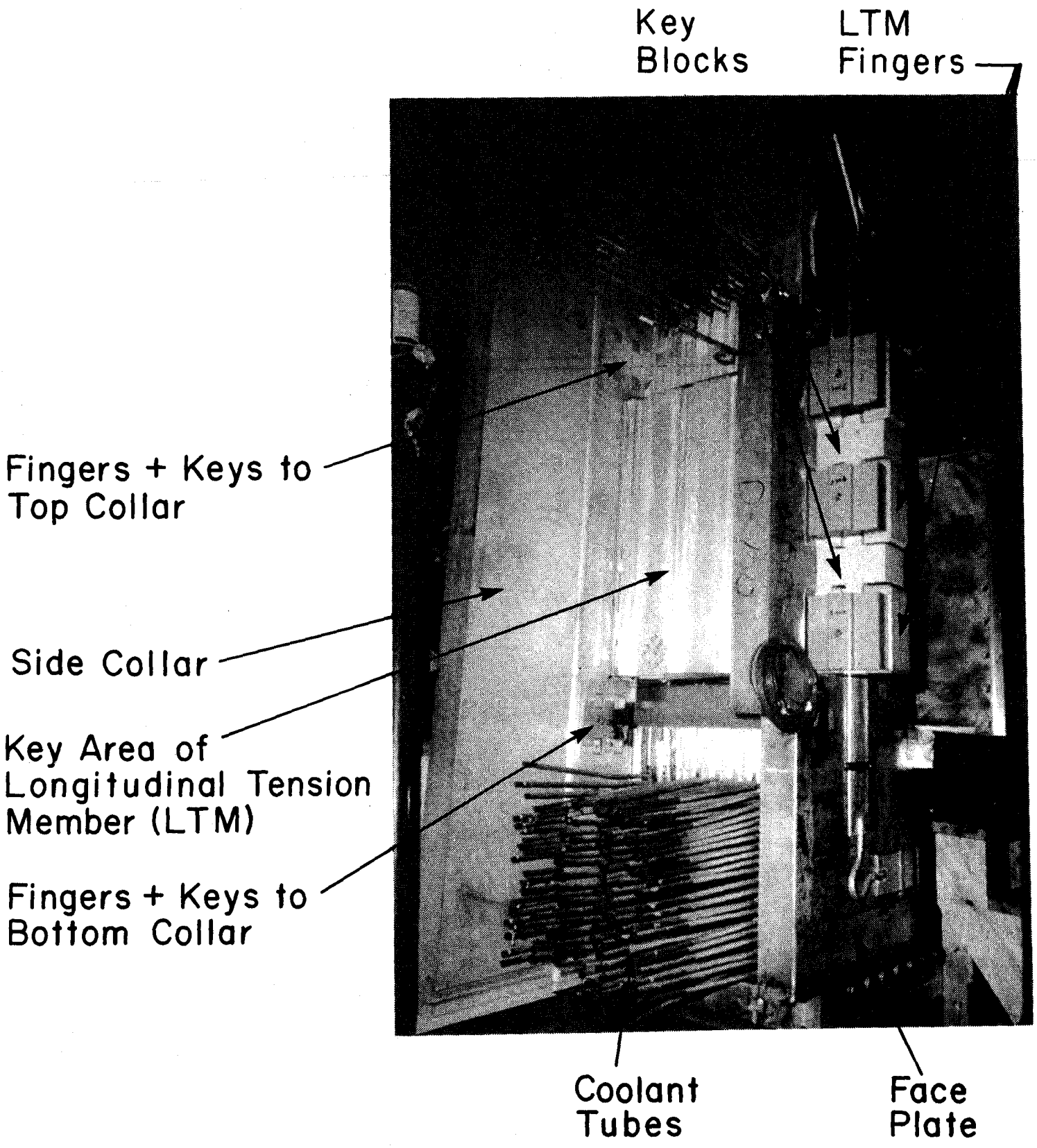

Figure 2.4 Partial Structure in the end turn region; LTM fingers and fingers and keys on the collar components are evident in this view (note: sideplate not in place).

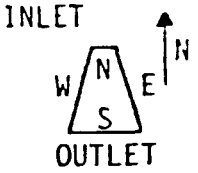

TABLE 2.1
HPDE MAGNET FCS

Damage Status Based on Visual Inspection

COMPONENTS	LOCATION	CONDITION
Face Plates	N, S	No failures
Side Plates	SW, NW	Failed through slotted regions
	SE, NE	No failure
Longitudinal Tension Members	W	Fingers failed at both ends. Plate fractured and separated at N collar region. Bend at S collar region.
	E	No failure evident at present
Collars	SW, NW	All fingers failed
	SE	Fingers failed at bottom
	NE	No failure
Vertical Side Beams	W	All connections to transverse tension members failed at top and bottom. Central regions intact.
	E	Failed along bottom at connections to the transverse tension members at ends.
Transverse Tension Members	W	All failed, top and bottom, at or near side beam connections.
	E	All failed or cracked along bottom except for one in center. Failure in several top members at each end.
Saddle Caps	N S	No failure, top or bottom
Tongues	S	Rotated about fore - aft axis but no failure
	N	Lips broken off
Vertical Edge Stiffeners	N S	No failure Failed

The relationship and scale of the iron flux return frame (magnet steel yoke) relative to other magnet components is shown in Fig. 2.5 and an overall view of the fully assembled magnet is shown in Fig. 2.6. The outer case (also called the thermal enclosure) in the end turn region was provided for thermal isolation. Overall characteristics of the magnet system prior to failure are summarized in Table 2.2.

TABLE 2.2
HPDE MAGNET CHARACTERISTICS

Copper conductor weight	83,500 kg
Aluminum structure weight	54,100 kg
Steel weight	500,000 kg
Pole length	7.1 m
Entrance aperture	0.89 m wide x 0.71 m high
Exit aperture	1.40 m wide x 1.17 m high
Half-coil height	0.50 m
Coil width	0.53 m
Space factor	0.8 m
Turns (total)	720
Length of average turn	22 m
Conductor dimensions	.025 m x .025 m
Cooling passages	.0068 m dia.
Overall length of coil	8.72 m
Cooling requirements	
LN_2 for initial cooldown	64,000 liters
LN_2 for recooling	<10,000 liters
Water (27 megawatts)	12.8 m^3/min
Peak axial fields	
Cold mode at pulse peak	6.0 tesla
Warm mode	3.7 tesla

On December 9, 1983 the magnet was being charged in a routine manner prior to an MHD channel test. It had been cooled to 105 K which was lower than any previous run. The coil was energized for 39 seconds and the field strength had reached 4.1 T (several earlier runs had attained or approached this level) when the force containment structure failed.

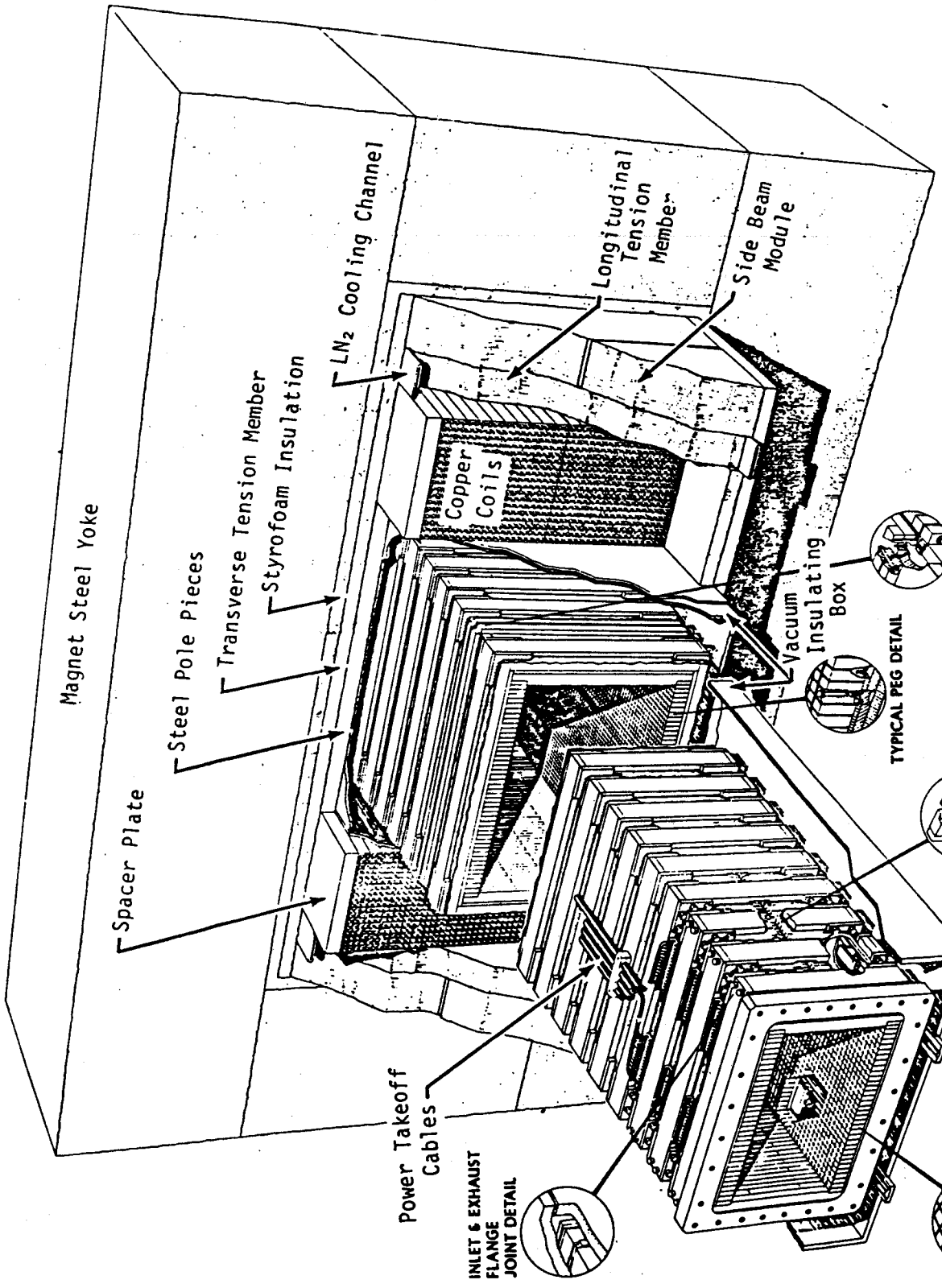

Figure 2.5 Schematic of HPDE magnet and MHD channel.

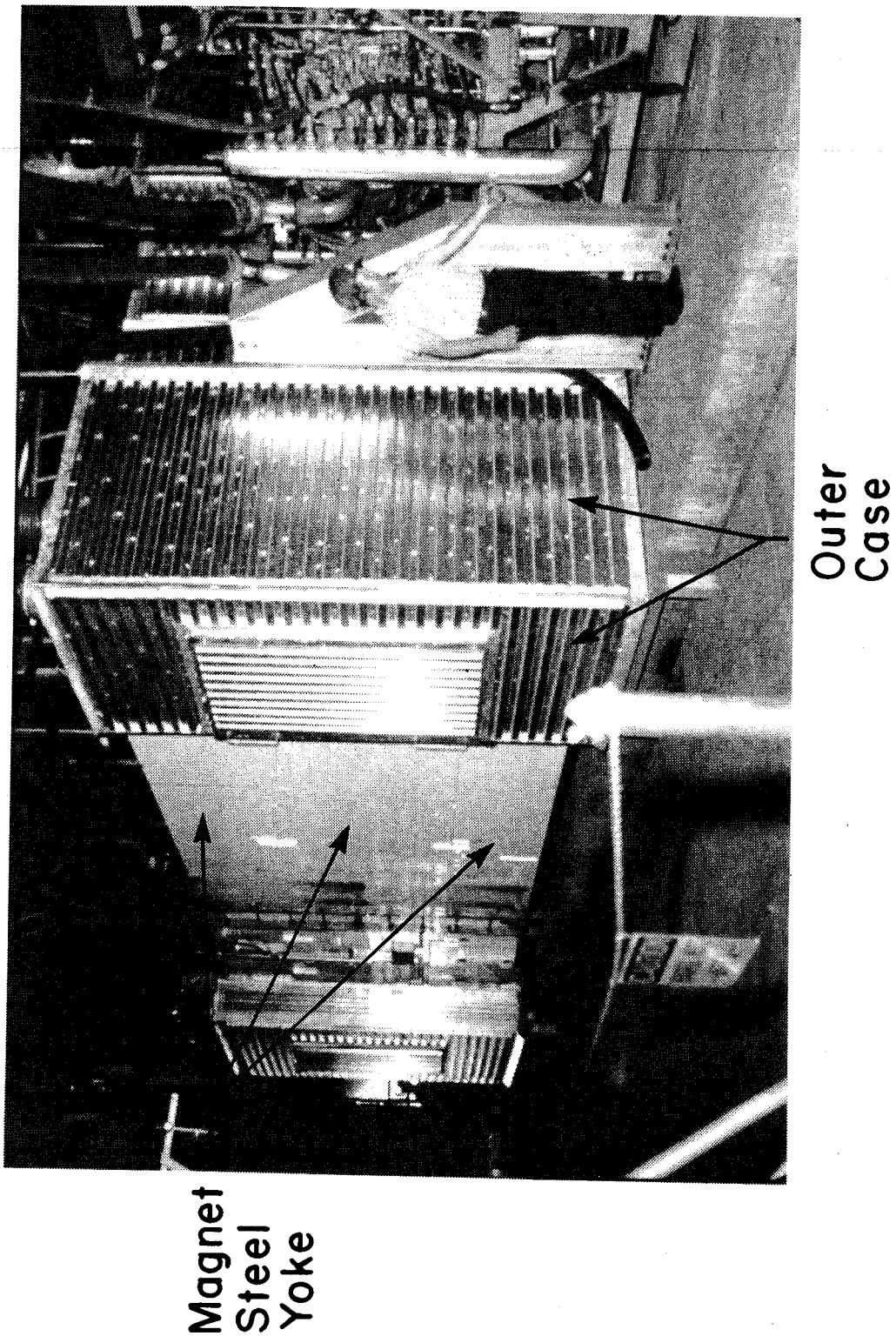

Figure 2.6 Overall View of the assembled magnet system.

The sequence of events during the failure is shown in Fig. 2.7, as reconstructed from the data systems and witnesses.[1] The time scale of the failure is shown to be very short in comparison to the electrical time constant (inductance divided by resistance) of the magnet. Observers described the failure as earthshaking and producing a loud boom which, although short, had a perceptible duration (time) and contained two peaks. A discussion of the sequence of events and the time scale of the failure based on analysis is given in Section 2.2.4.

The figures described in the following were taken at various stages in the disassembly process. Figure 2.8 shows the fracture at the base of the LTM fingers. A closeup of the fracture at the base of a finger is shown in Fig. 2.9. Note that the presence of the finger and the keyways in the finger represent significant stress concentrations and a significant reduction of the LTM load carrying ability relative to its full size cross-section which existed over most of its length. The failure in this region was accompanied (either immediately before or immediately after) by failure of the fingers which key the four components of the collar assembly together.

Failure of the collar in the end turn region led to a sequential overload and failure of each transverse tension member and vertical side beam subassembly along the length of the magnet. Figure 2.10 shows several fractured vertical side beam modules after removal and placement side-by-side on the floor.

After failure of the transverse support structure, the longitudinal coil windings moved outward under the action of the sidebar forces. Figure 2.11 schematically illustrates the manner in which the outward deformation was

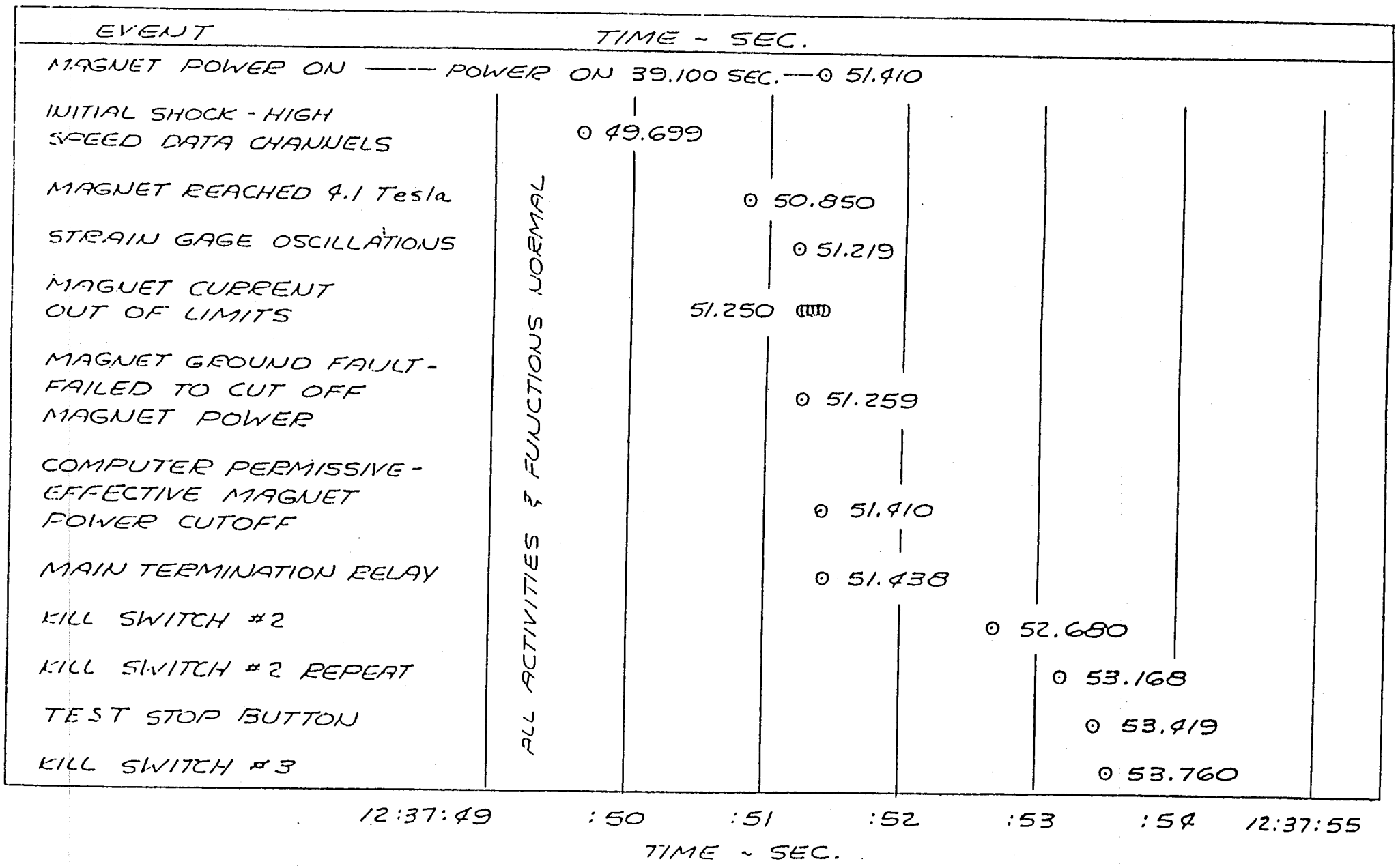

Figure 2.7 Reconstruction of events HPDE run 007-018

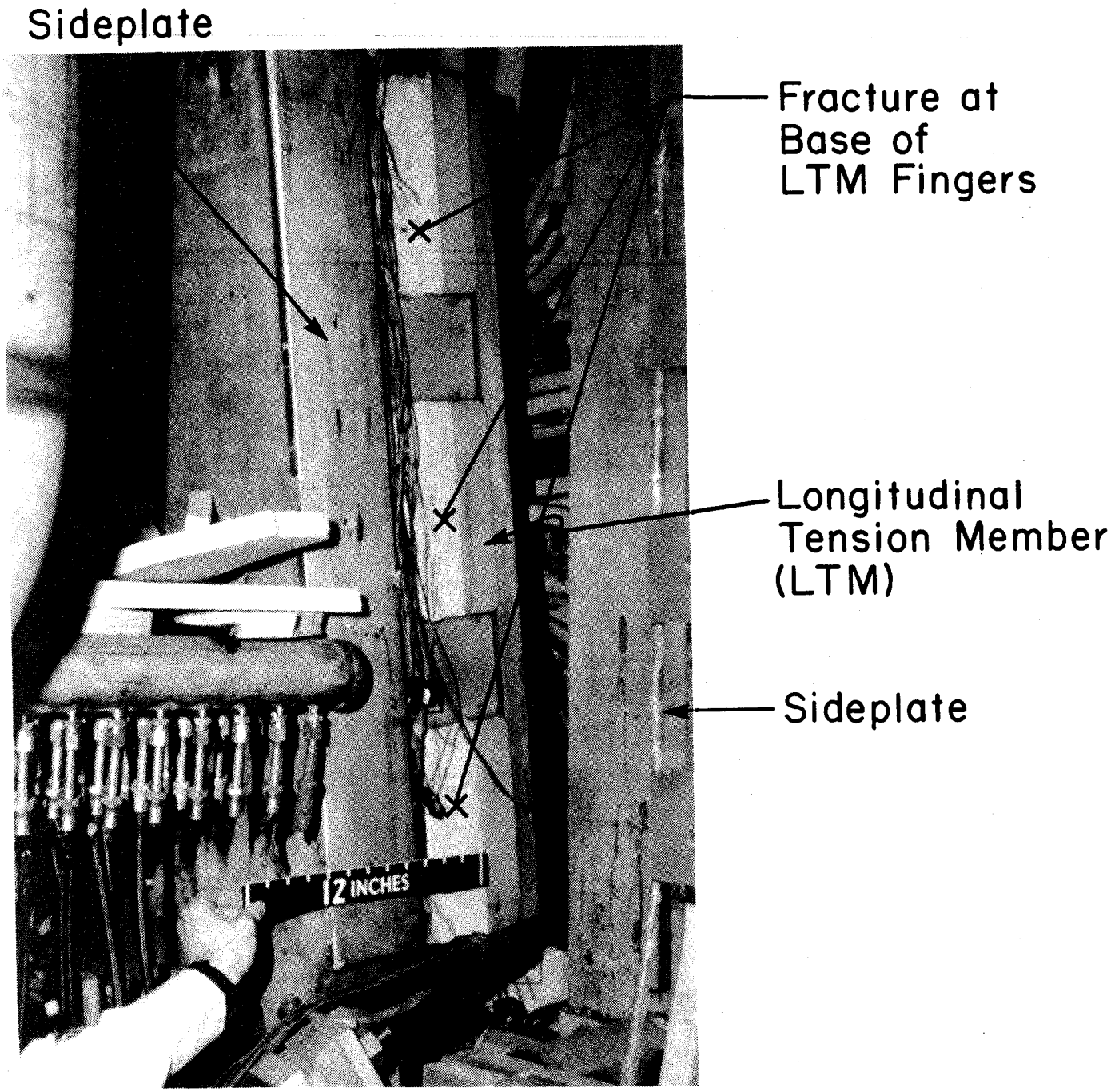

Figure 2.8 Fractures at base of LTM fingers.

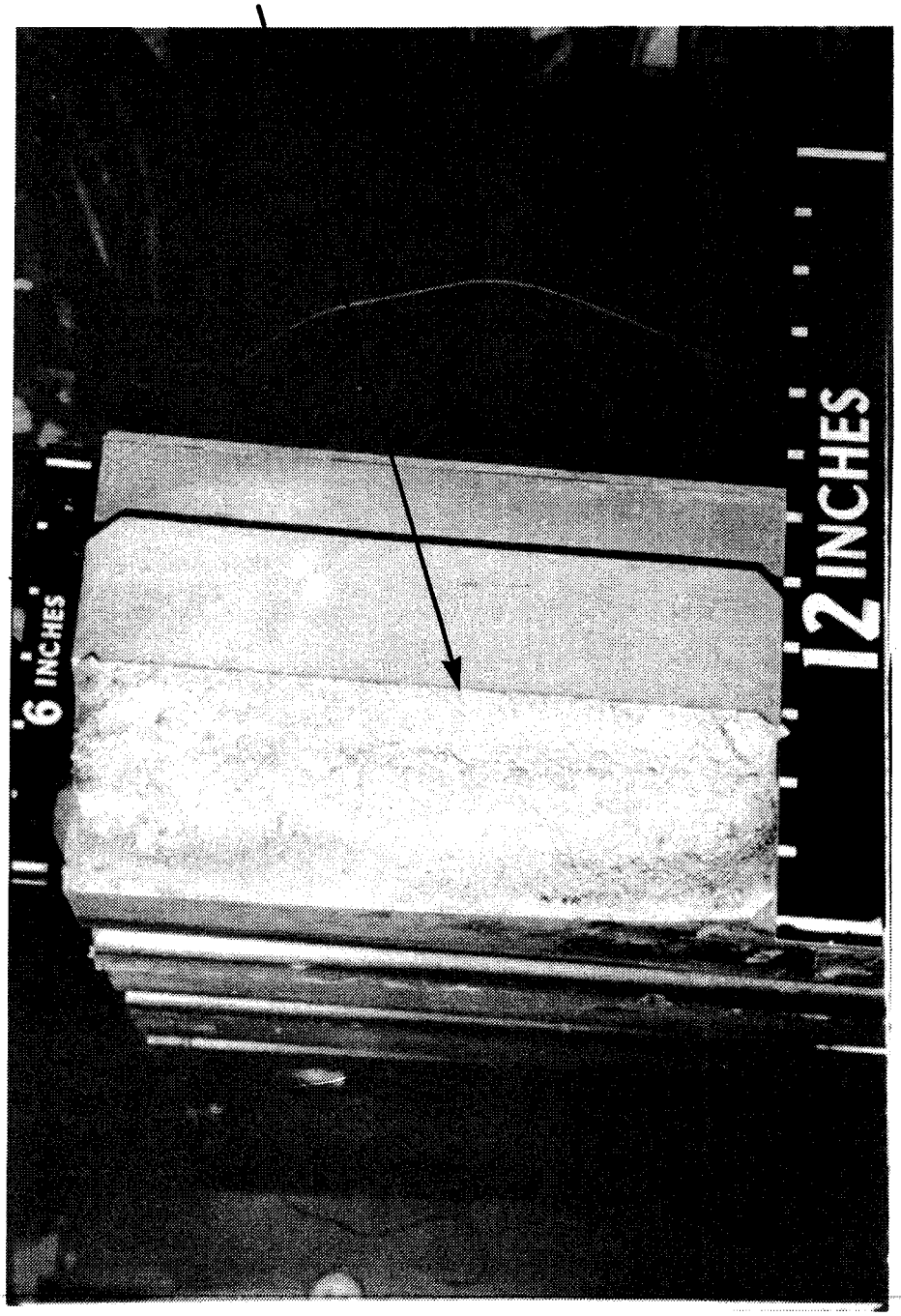

Figure 2.9 Close-up of the fracture of an LTM finger.

Figure 2.10 Several vertical side beam modules with typical fractures at locations where they connect to the transverse tension members.

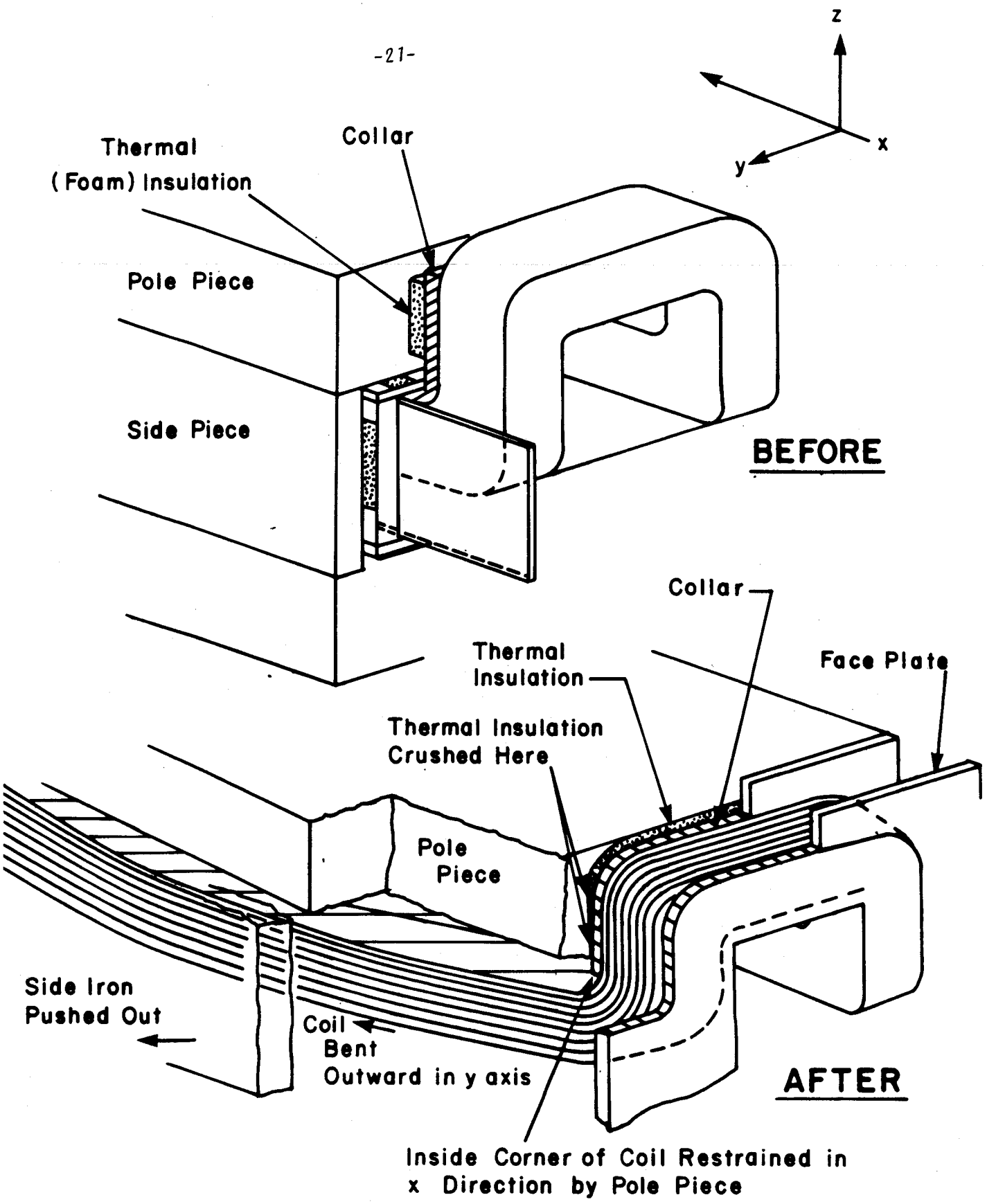

Figure 2.11 Schematic illustrating manner in which coil outward displacement was restrained by pole piece.

ultimately restrained. This occurred because the coil cross-section was large enough to carry the load as an outwardly loaded arch anchored at its ends by the end turns pulling in towards the pole piece. In a winding designed with a high enough current density (i.e., small cross-section), the windings would not necessarily be capable of this restraint and could have fractured. This effect is studied with a simplified model in Chapter 3.0 to illustrate the ability of a winding to absorb the load and restrain the conversion of magnetic to kinetic energy.

Figures 2.12 is a view looking down the side of the magnet from the top before removal of side components of the iron flux return frame. The view indicates the displacement of the iron from between the top and bottom magnet steel yokes by the outward movement of the windings. The displacement and arch formed by the windings as well as the anchoring of the windings at the ends is shown in Fig. 2.13.

Despite the relatively large winding deformation, very few turns were actually severed. Damage to the winding was most severe in the ends of the top and bottom two layers which were adjacent to the steel yokes and subjected to substantial loading as a reaction to the arch formed by the windings when they moved outward. A view in this region is given in Fig. 2.14.

Figure 2.15 shows the winding deformation at the "far" end of the magnet from the point where the failure initiated. Note the broken LTM fingers lodged in the faceplate and the winding deformation relative to the flatness of the faceplate.

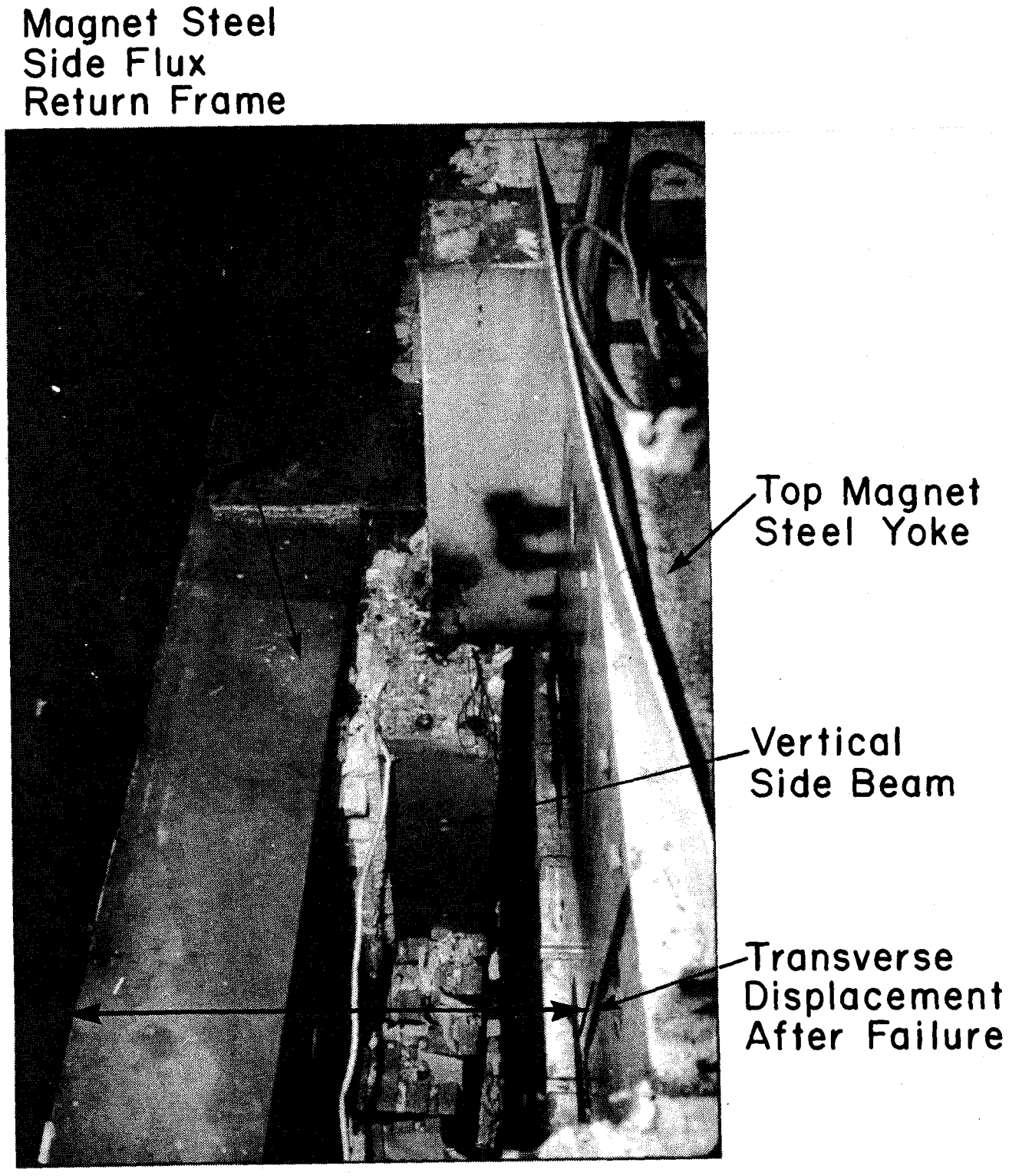

Figure 2.12 View looking down the side of the magnet from the top.

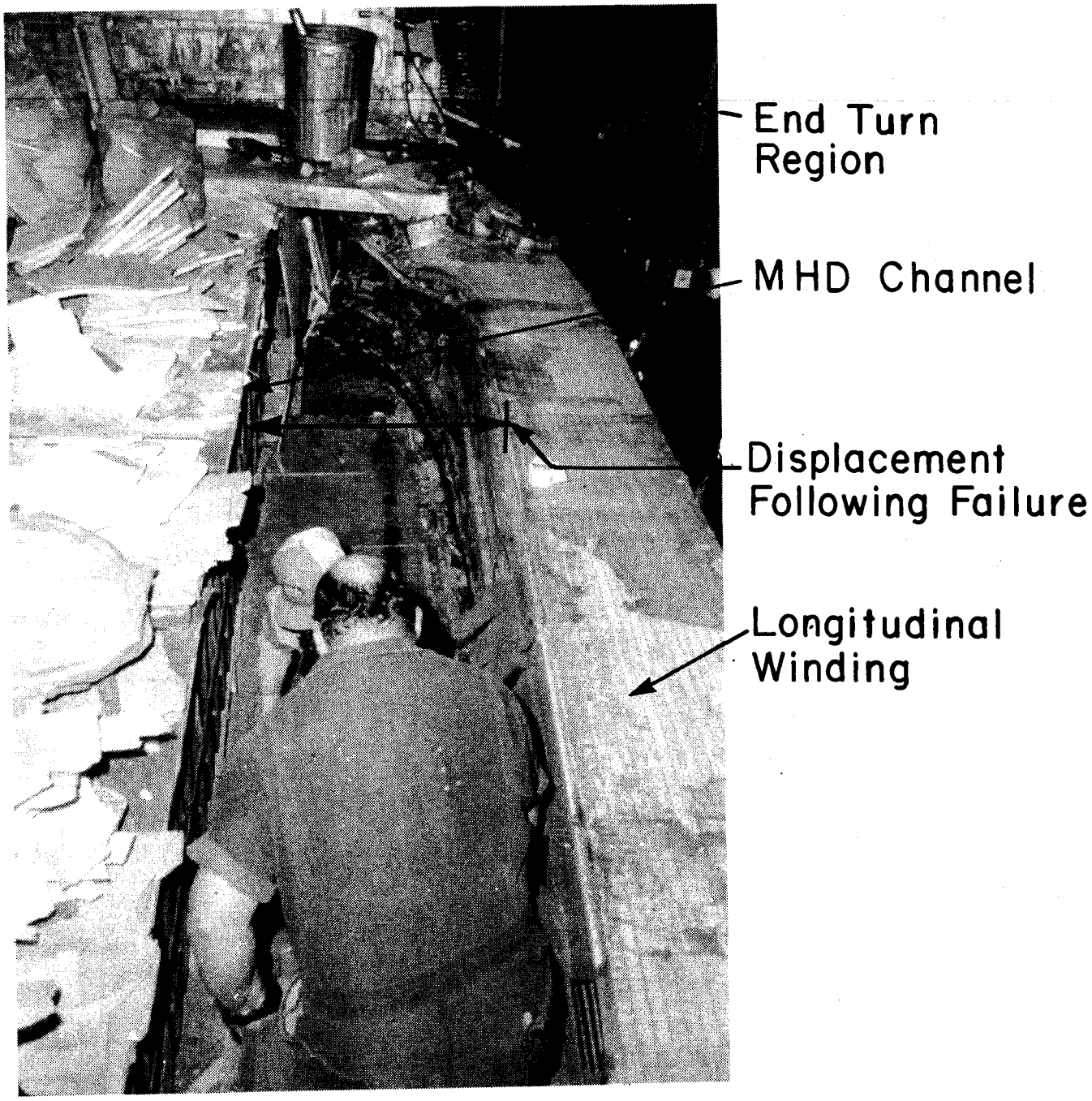

Figure 2.13 View showing outward movement and arch formed by winding.

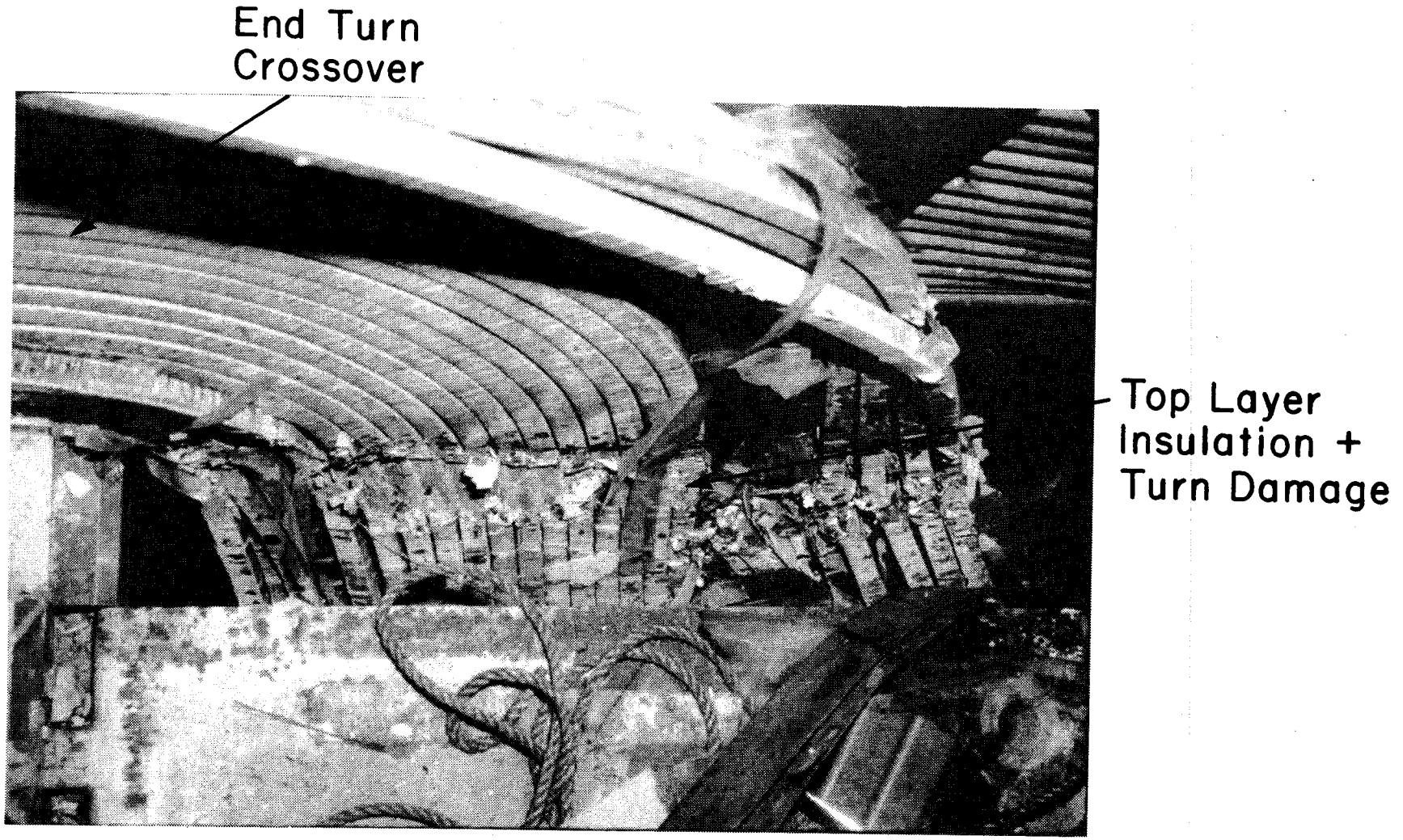

Figure 2.14 Turn and insulation damage in top layer adjacent to steel yoke.

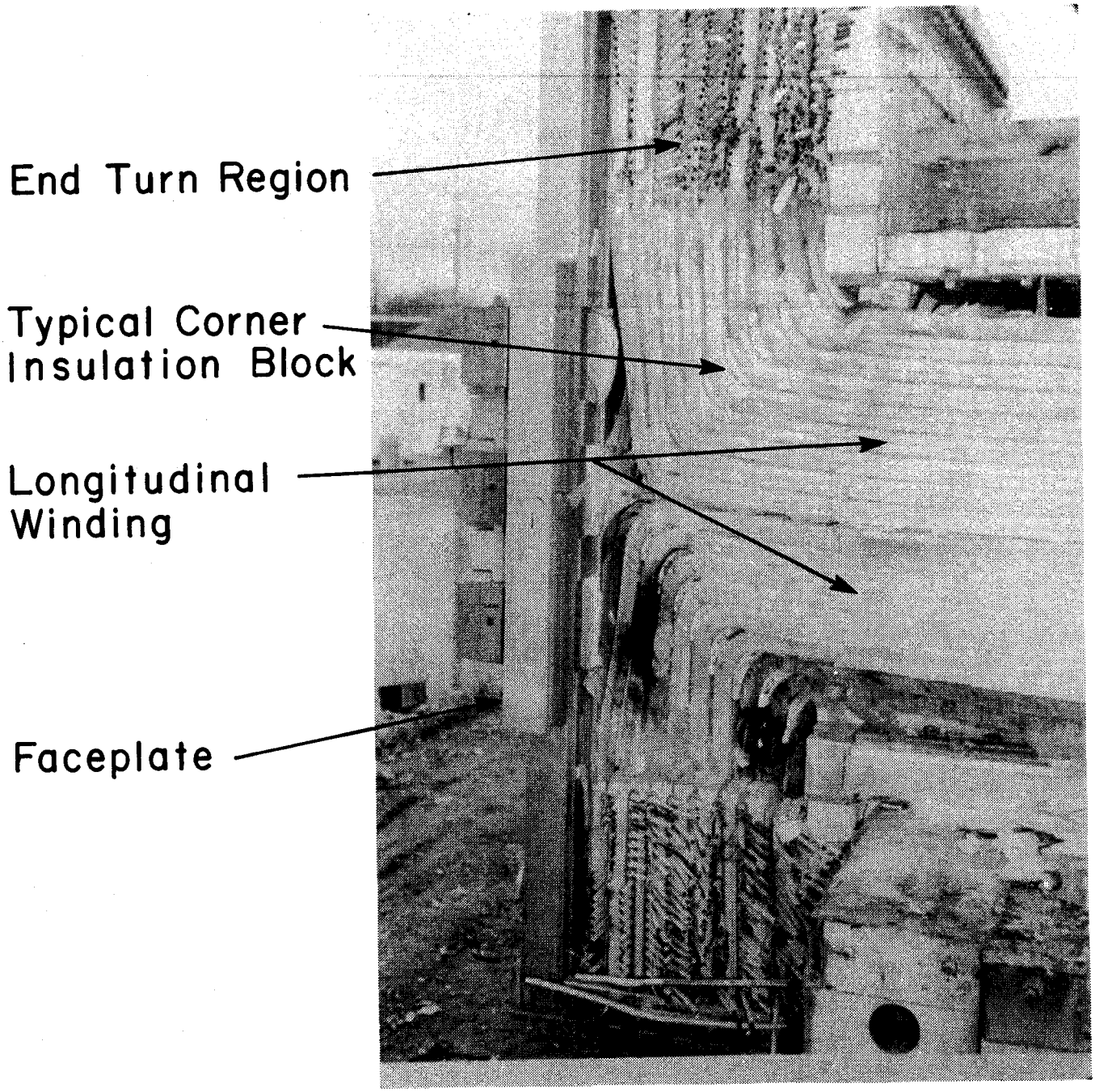

Figure 2.15 End turns with iron side structure removed. Note LTM fingers entrapped in faceplate.

The HPDE magnet failure was catastrophic in the sense that most structural components were fractured and the winding suffered extensive plastic deformation. However, operating procedures prevented possible injury to personnel and the rugged nature of the winding limited deformations to large but safe values, and restrained conversion of magnetic to kinetic energy of failed components. This suggests that it may de desirable to limit operating current densities in magnet design to levels whereby the winding could act in this structurally fail-safe manner even if it sustained substantial deformation in the event of a failure in its primary structure.

2.2 Preliminary Structural Failure Analysis (May 1983) - H. Becker, A. Hatch, P. Marston and J. Tarrh

Strength-of-materials calculations have been performed on the HPDE magnet at AEDC to assist in determining the nature and cause of the failure that occurred in the force containment structure (FCS) on December 9, 1982. From a structural standpoint, the broad basis for the failure appears to have been design flaws, particularly of structural details. Initiation of the failure was the result of severe overloading of the fingers in the ends of the "longitudinal tension members" where they penetrate the "face plate" and also of the fingers in the collar" (See Fig. 2.16). These very high local stresses were not detected in either of the previous stress analyses performed. The use of materials having low ductility may have contributed to the extent of the failure.

The results of the calculations are summarized and the most probable failure scenario is identified based on the calculations. The conclusions must be considered tenetative since they are founded on structural mechanics only,

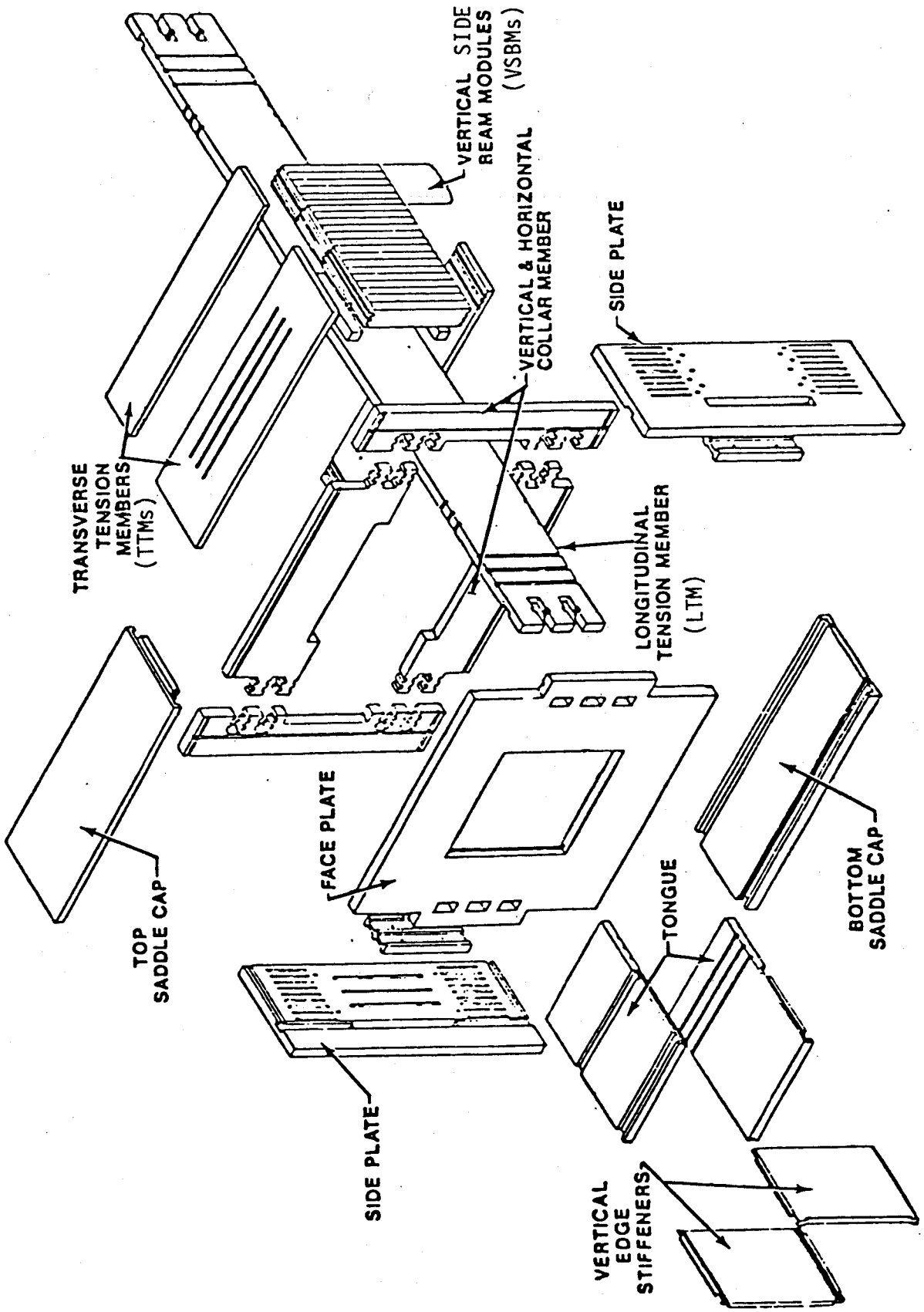

Figure 2.16 Expanded view of force containment structure (FCS) and key to abbreviations

although at present the locations and shapes of the visible fracture surfaces appear to substantiate the conclusions.

2.2.1 Failure Sources

The structural failure of the magnet, which occurred at only 2/3 of design field (less than half load), may be attributed to inadequate structures engineering. Four related aspects are discussed in this section: the design concept, the stress analysis, inspection, and the materials selection.

Design Concept

One of the design criteria for the force containment structure was ease of assembly and disassembly. One of the results of this criterion was the use of the vertical notches that cut through the fingers at the ends of the longitudinal tension members (LTMs). The consequent reduced section is among the prime candidates for the failure initiation site; however, a thorough analysis of the stresses in these areas had not been done previously.

The basic concept for the force containment structure requires the use of four load paths to transmit the major portion of the axial Lorentz load from the end structural plate/collar system into the LTMs, which react the axial forces. None of these load paths was considered stiff enough (by analysis) to transmit more than 40 percent of the axial force. Furthermore, the stiffest axial path would not begin to act until the remainder of the system were to deform to half the design value. Since the magnet never was loaded beyond that value, it is possible that the stiffest load path was inactive at the time of failure. However, this axial load condition appears to have had little influence on the mode of failure initiation.

Lorentz loads in all directions are transmitted through fingers, keys and key blocks. Tolerances among these structural elements and deformations during loading could alter the design load paths. As a result, local structural behavior could have become the most important factor in controlling the magnet's structural integrity.

Stress Analysis

Prior to this analysis, no calculations appear to have been made of the stresses induced by the transverse Lorentz forces on the LTMs and the surrounding structure at the magnet ends. That is, the longitudinal force supports were thoroughly analyzed, but no consideration was given to the effects of the transverse deflections of the structure (due to the transverse Lorentz loads) on the stresses in the longitudinal force supports. As will be shown, the axial stresses in the LTM fingers due to longitudinal forces alone are trivial compared with the actual stresses when the transverse deflections are taken into account. Conclusions about fatigue life were drawn from a fatigue curve constructed using an artificial procedure instead of test data. No fracture mechanics studies were performed.

Inspection

There is no record of inspection of critrical areas identified in the previous stress analyses, although ice formation was observed in areas where a crack might have been initiated. While the magnet was extensively instrumented, the strain gauges were located in such a way that critical stresses were not detected.

Material Selection

Aluminum alloys, which have low fracture toughness, were used for the force containment structure. They tend to propagate a fatigue crack rapidly when the crack length is of the order of 1/10 inch (a nominal minimum observable size) if the peak theoretical elastic stress exceeds 100,000 psi, as predicted would occur. In addition, the high strength 2000 series aluminum alloys commonly are corrosion sensitive.

All of these areas were working together against successful operation of the magnet. However, had adequate stress analysis of the structural details been performed, the inadequacy of the structure would have been apparent.

2.2.2 Stress Analysis

Summary

An analysis was conducted by MIT primarily to identify regions of high stress, the conditions that induced that stress, and the possible impact upon a failure scenario. Hand calculations were used since high precision was unnecessary. A number of dimensions were scaled from drawings. The results of the analysis appear to indicate the probable structural failure site and failure mode.

The dynamic behavior following failure initiation also was considered. In addition, a structural energy budget was prepared. A simplified fracture mechanics analysis was performed to supplement a fatigue life calculation.

The calculations were performed for nominal 4 tesla forces. Loads were actually assumed to be approximately 45 percent of the calculated forces shown in Fig. 2.1 (from Reference 2). The same fraction was used for the pressure

distributions given in Reference 3.

The structural behavior was assumed to be symmetric from side to side and from top to bottom.

The highest stresses were found at the outlet end of the magnet in the fingers of the LTMs and in the fingers at the corners of the collar (Figs. 2.17 and 2.18). The numerical magnitudes of the calculated stresses in these locations were of the order of twice the measured ultimate strengths of the aluminum alloys used in the FCS. Stresses at selected other locations were found to be in the range between yield and ultimate.

The presence of stress concentrations, ice pressure (if present), and temperature gradients would amplify these stresses. However, these effects were not included in the stresses calculated by MIT and reported herein.

The axial load paths were assumed to follow those shown in Reference 2. As mentioned above, however, calculations indicate that small tolerances at the various keys in the system could alter the Lorentz load distribution and possibly, in an extreme case, eliminate one or more thereby overloading the others. Furthermore, the use of a gap in the spacer bar (between LTM and TTM) indicated that below 4 T the potentially stiffest load path for longitudinal forces was out of action.

Results of Calculations

The peak stresses were found to occur in the downstream fingers of the LTMs (Fig. 2.17) and in the corner fingers of the collars (Fig. 2.18).

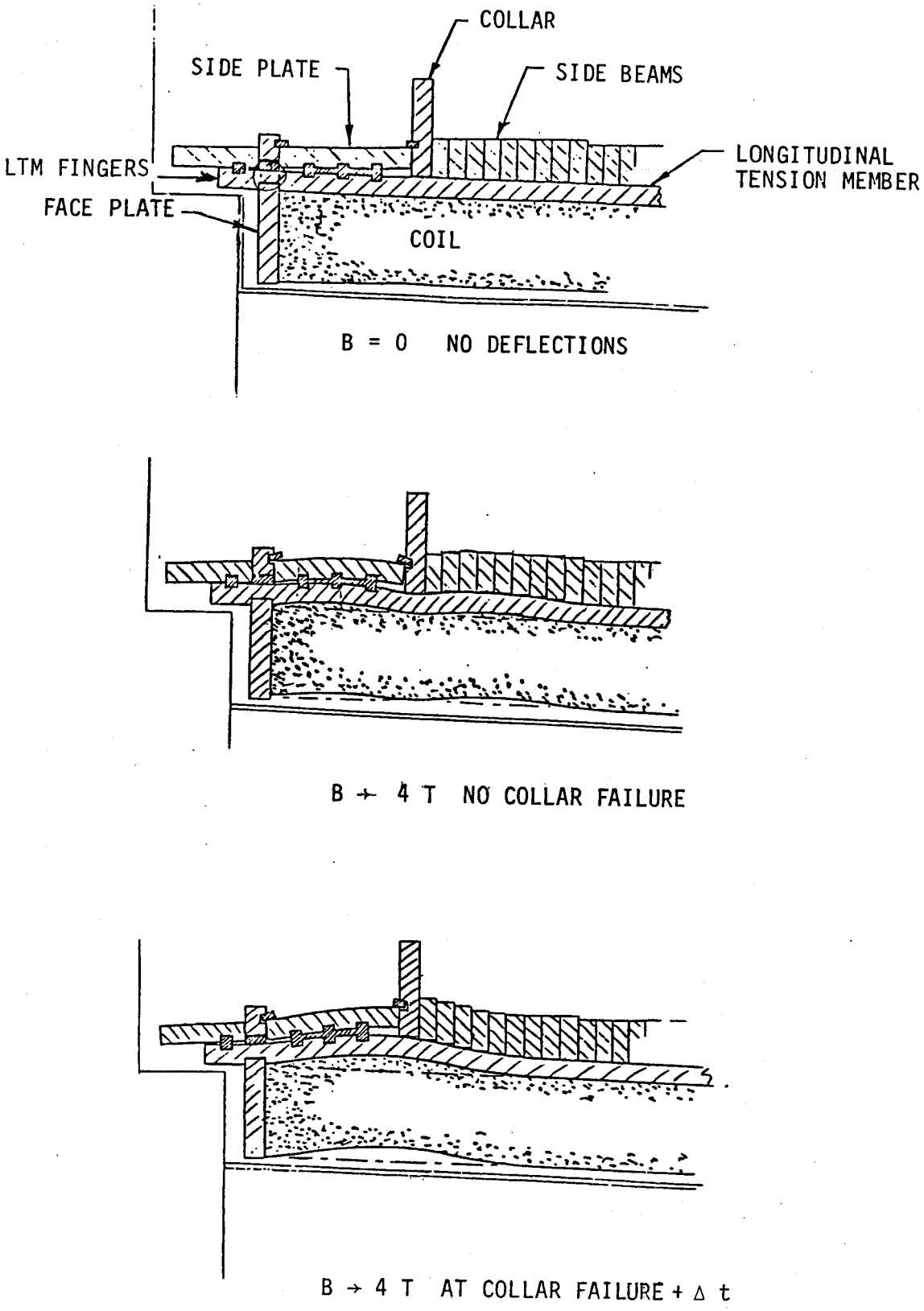

Figure 2.17 Exaggerated depiction of LTM-related deflections at the magnet midplane

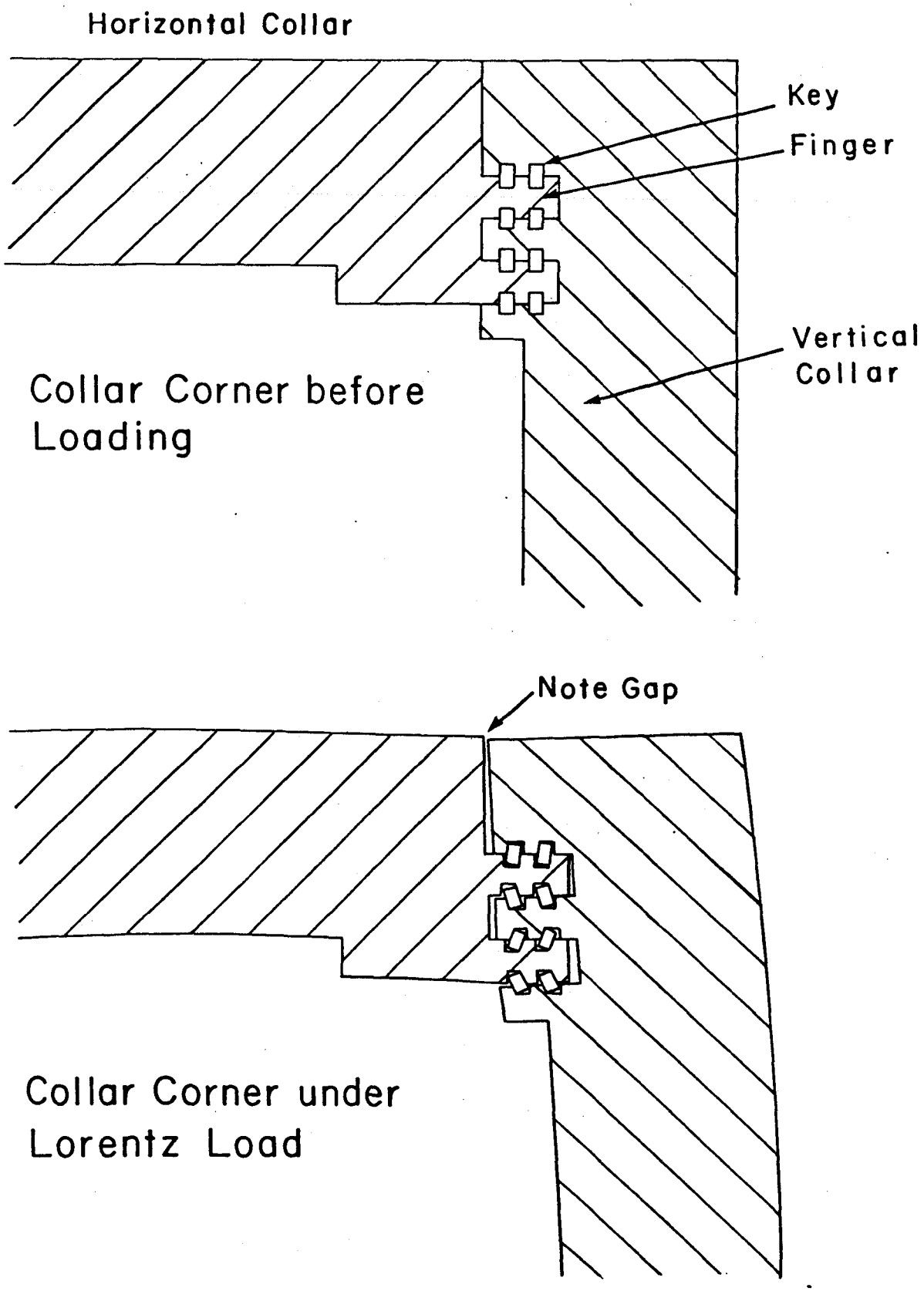

Figure 2.18 Collar corner behavior

The major stresses in the LTM fingers were due to sidewise bending of all the fingers about a vertical axis and vertical bending about a horizontal axis in the top and bottom fingers only. As mentioned herein above, the axial tension was small. Figure 2.19 depicts the stresses due to each component. Combined values appear in Fig. 2.20.

In addition to the high normal stresses (nominally twice the 86 ksi ultimate tensile strength of 2219 aluminum alloy at 77 K) a twisting shear stress of the order of the ultimate strength can act on the plane of the nominal fracture surface. It would arise from resistance to the anticlastic (saddle shape) curvature induced by the horizontal bending of the LTM (Fig. 2.21). (It should be noted that anticlastic curvature was observed at the LTM downstream end where the fingers broke.)

The neutral axis orientation in each finger is shown in Fig. 2.20. Each is rotated slightly from the vertical. The sense of rotation is different from that measured at AEDC (Fig. 2.22). However, the discrepancy is slight and may be due to the torsional shear and to details of the key/block/faceplate fitup at each finger.

The sidewise deflection shape of the LTM is shown in Fig. 2.17. The cause of the large horizontal bending stress is depicted. It arises from LTM bending (induced by the transverse Lorentz forces) between the faceplate and collar, together with bending from the outward deflection of the collar. The sideplate was found to be too flexible to support more than 20 percent of the Lorentz pressure on the LTM. Furthermore, the collar was found to react some of the transverse Lorentz pressure that would be expected to act on the VSBM/TTM

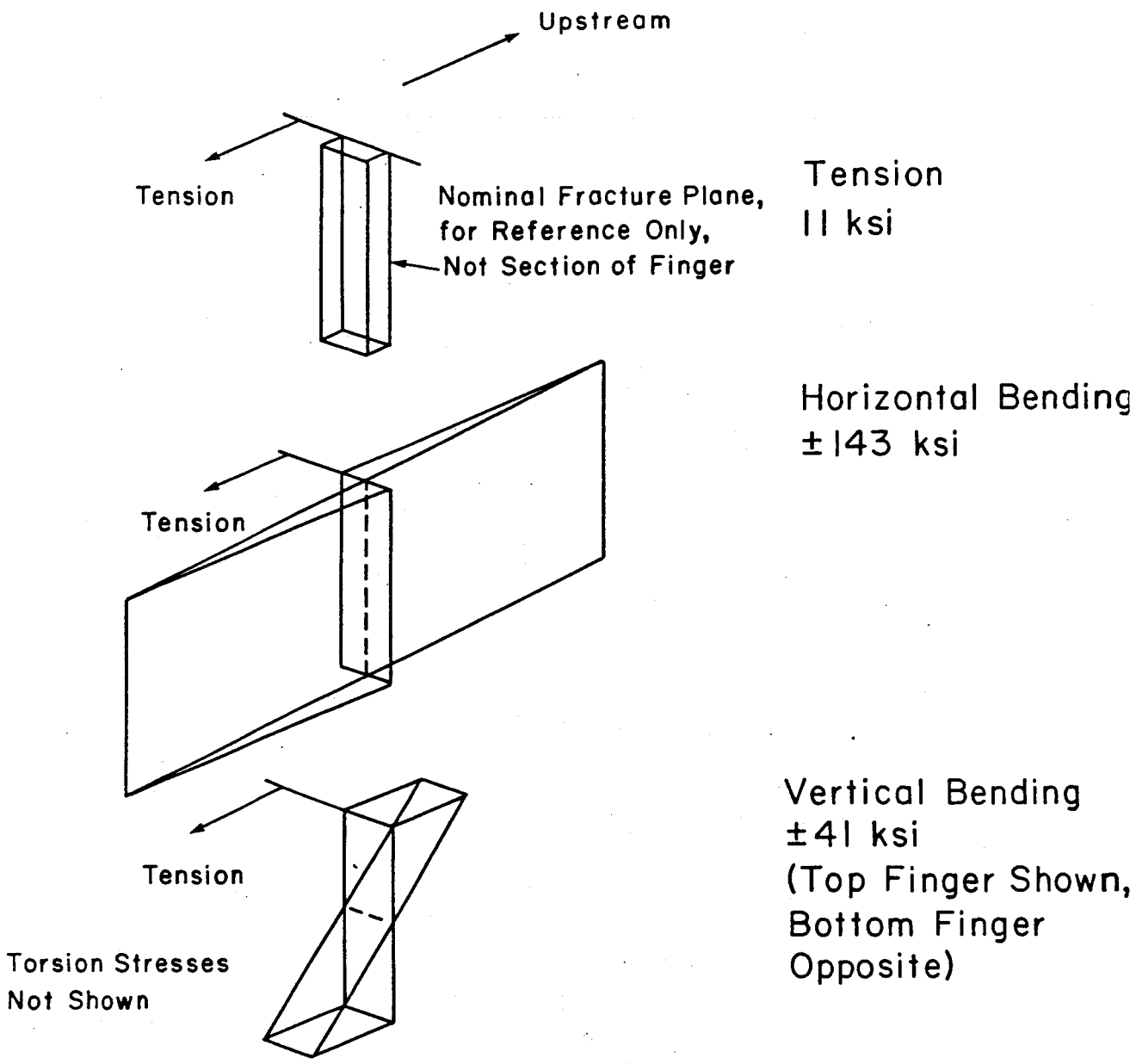

Figure 2.19 Stress components acting perpendicular to nominal fracture plane of LTM downstream fingers at groove.

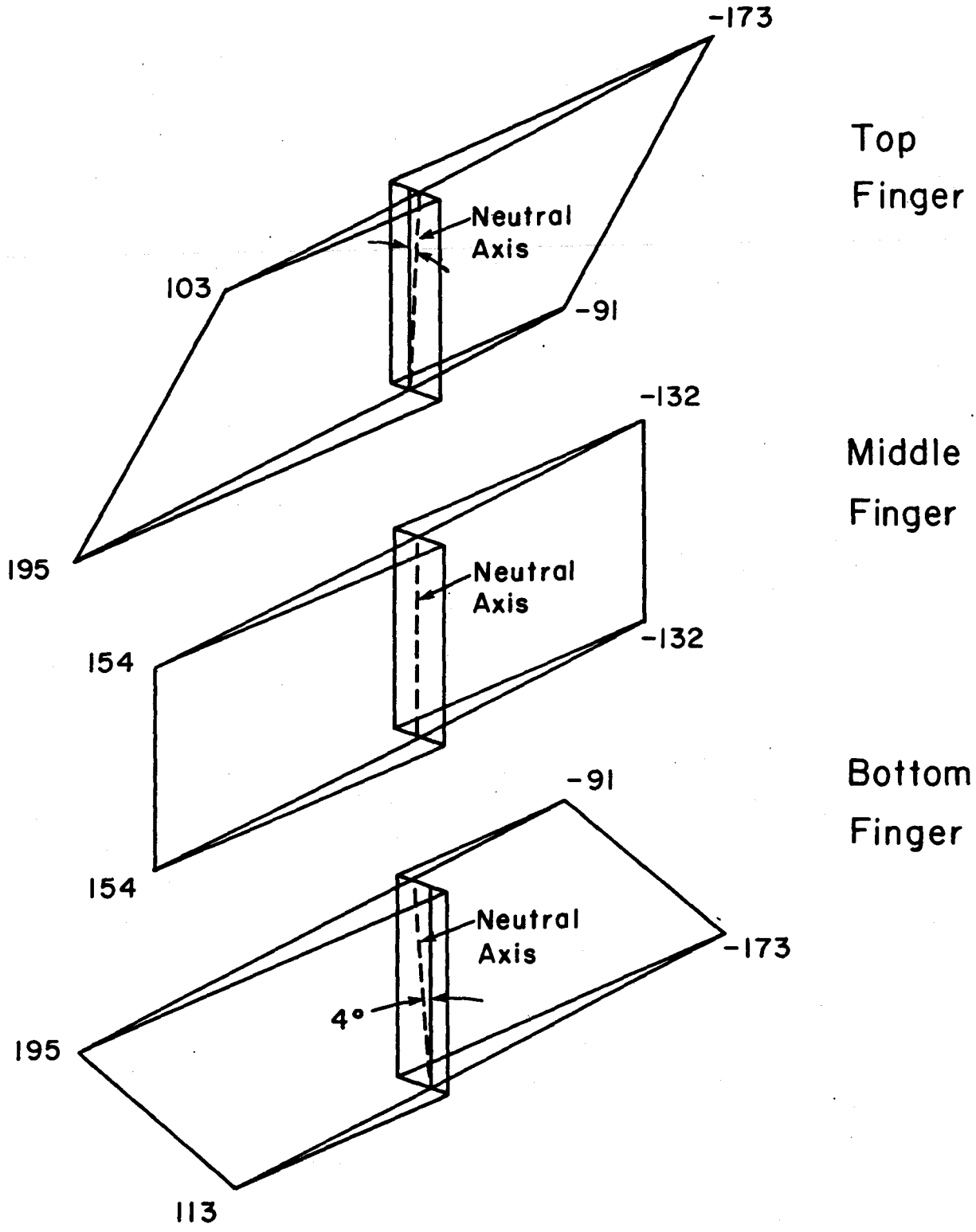

Figure 2.20 Combined stresses (ksi) in sections of LTM downstream fingers

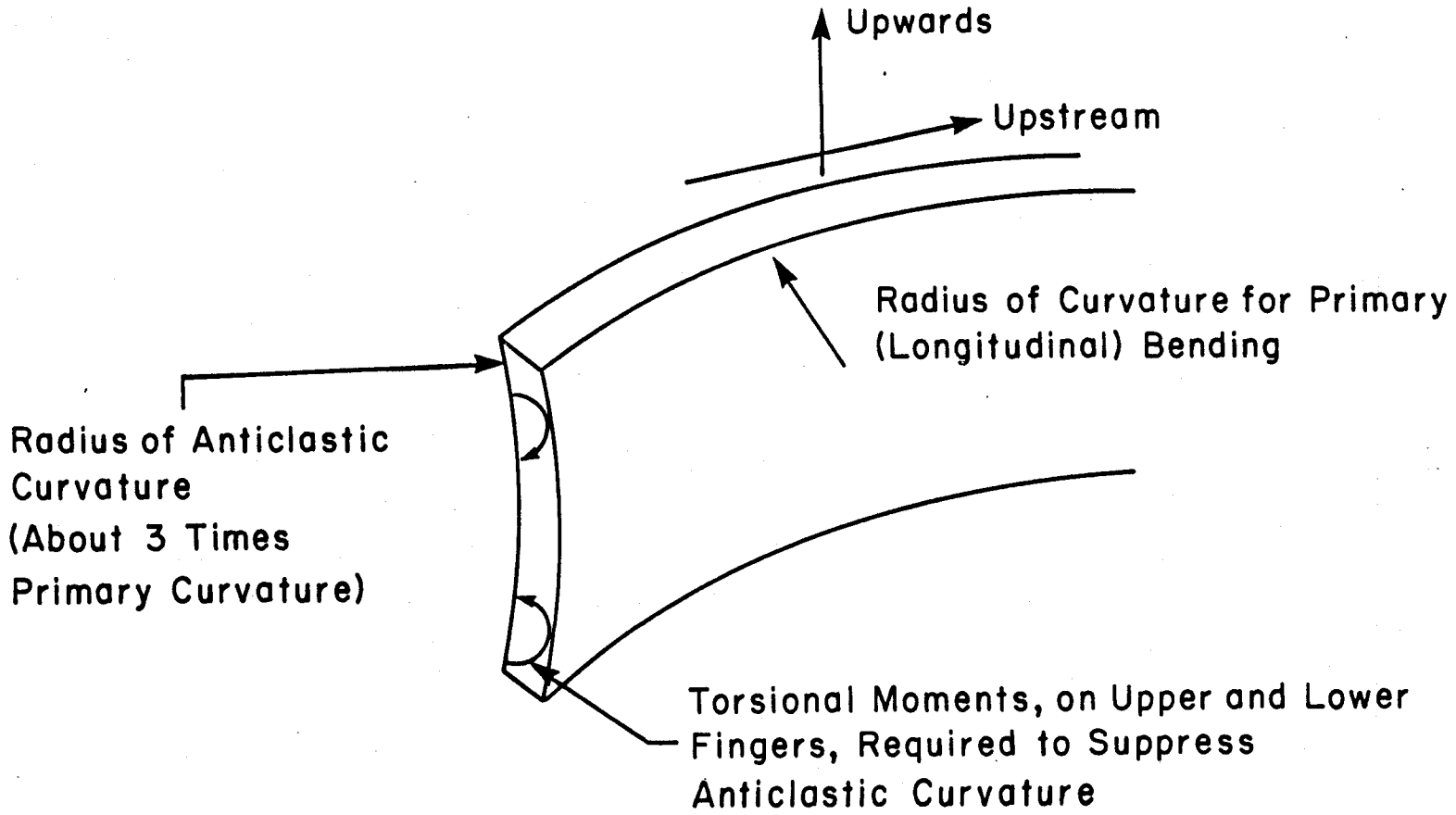

Figure 2.21 Anticlastic curvature effects at ends of LTM

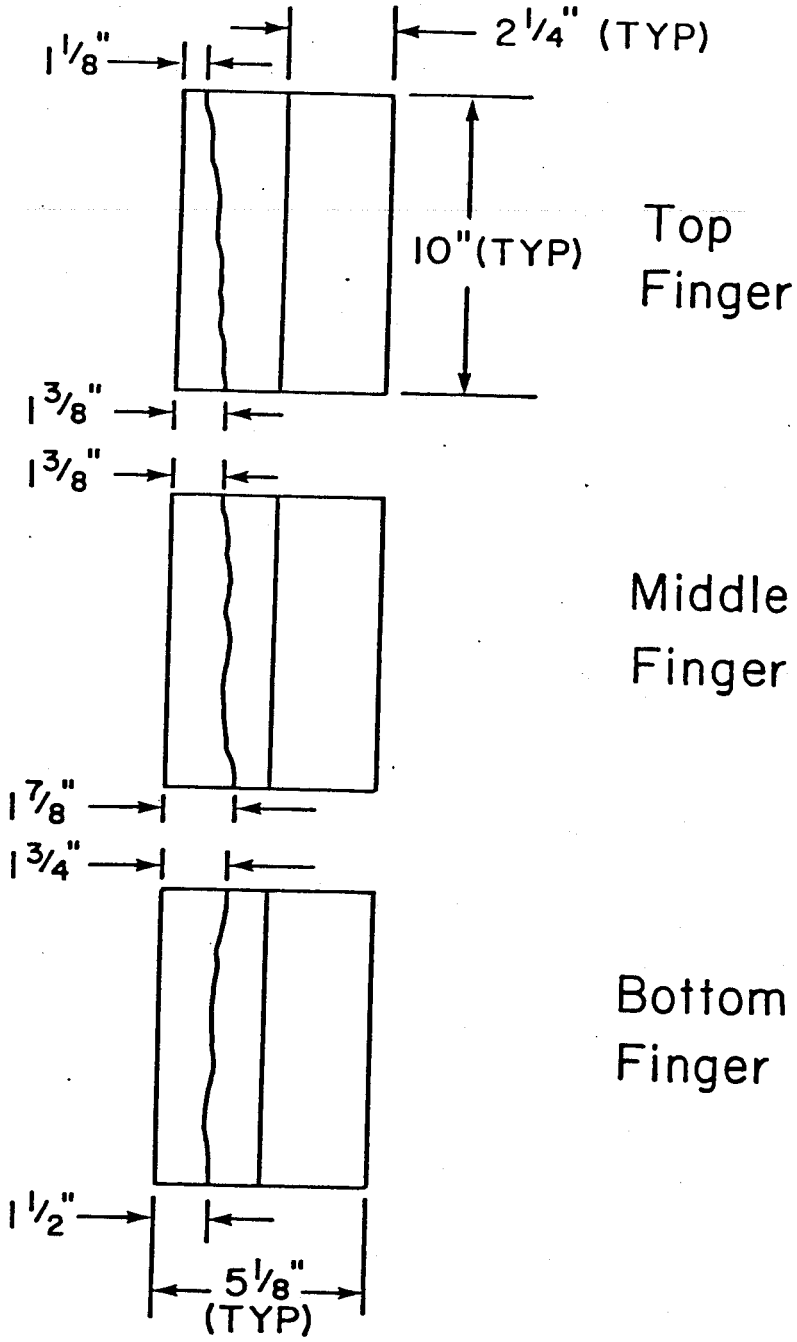

Figure 2.22 Approximate center of fracture "valley" to edge of LTM

subsystem. The local load distribution was found from assuming the VSBM/TTM combination to act as an elastic foundation for the LTM, taking the finite rigidity of the collar into account.

The calculations indicate that the large transverse force on each vertical collar causes the corner fingers to stretch far enough to prevent contact of the vertical faces of the horizontal and vertical collars (Fig. 2.18). Therefore, the local rotations could be resisted only by the fingers in vertical bending. The axial forces on the collars induced bending about a vertical axis thereby inducing a stress field similar to that in the LTM fingers (Figs. 2.19 and 2.20) and at a comparable level of combined stress.

The calculated numerical values of stress in the fingers of the LTMs and the collars differ somewhat but are of the same order of magnitude (twice the ultimate tensile strength of 2219). Precise comparisons would be of little value at present considering the indeterminate factors mentioned above. Most important, however, is the fact that the calculated stresses do not include concentration factors.

Fatigue Life Estimate

An estimate was made of the fatigue life to be expected for the HPDE FCS at a peak field of 4 T with most pulses at much lower values. For this purpose, the alternating stress was chosen arbitrarily at 86 ksi since most of the fatigue damage would occur at the higher stresses, and concentrations would tend to increase the stresses (or resultant strains) mentioned above. The curves of Fig. 2.23 were used for the prediction. They indicate 36 cycles using Reference 3 data and 10 times that for the assumed AEDC curve.

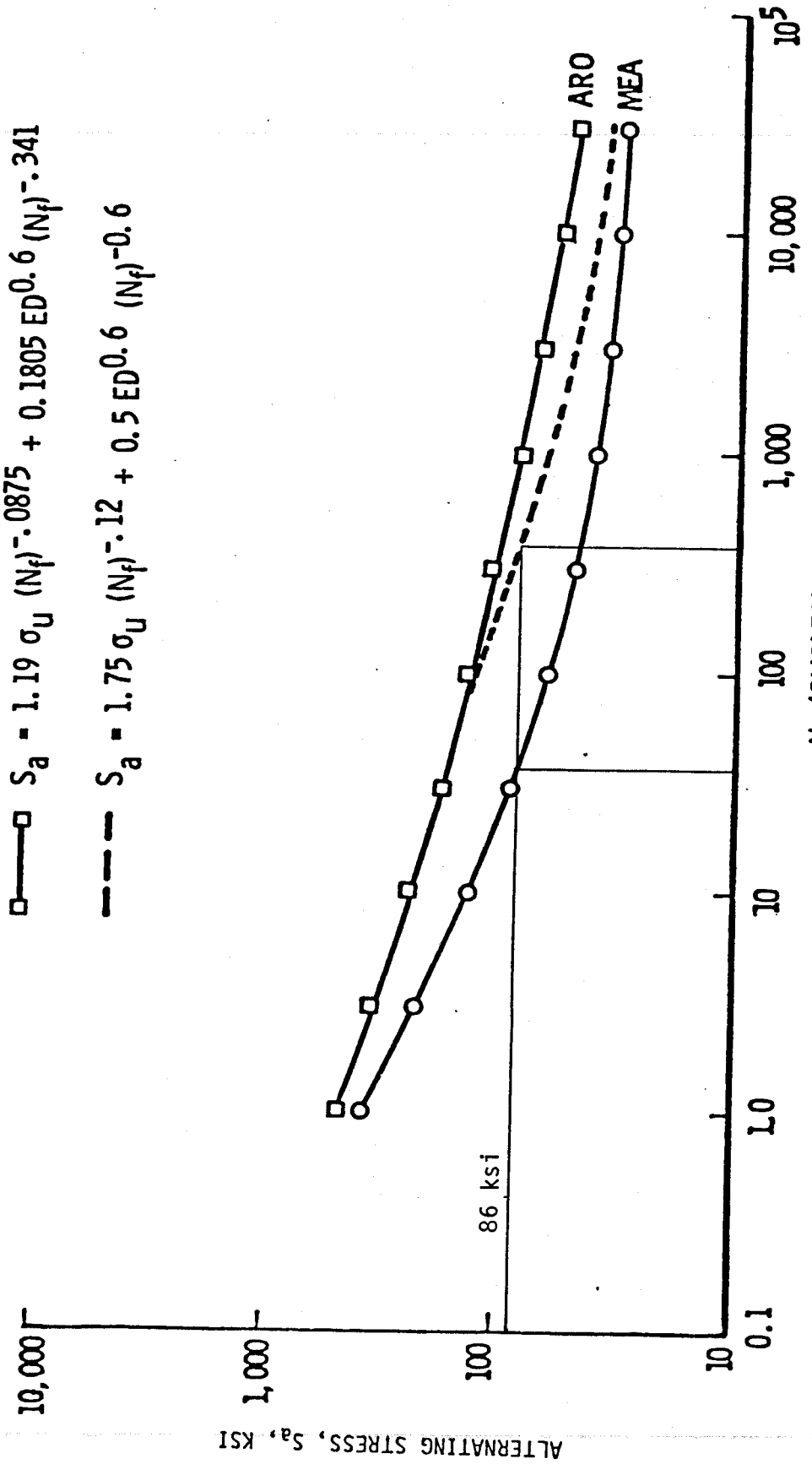

Figure 2.23 Comparison of life cycle curves used in magnet design and force containment structure calculations

These results raise the question of possible cracking at the LTM and collar fingers at early stages in the life of the system. However, the small critical crack size (of the order of 1/32 inch at 83 ksi from a linear elastic fracture mechanics calculation) also indicates the potential difficulty of observing cracks during a casual inspection. A dye penetrant procedure, for example, would have been required.

2.2.4 Failure Scenarios

Sites and Modes

The calculated high stresses in the fingers of the LTMs and collars indicate that either could have been the site of initial failure (Figs. 2.17 and 2.18). Furthermore, if either set of fingers was to break suddenly, failure of the other set would be expected to follow within fractions of a millisecond.

After the LTM fingers broke, the axial stress wave resulting from the unloading traveled upstream. The mass of the LTM behind the front was moving upstream at 10 to 15 miles per hour. The wavefront reached the aluminum mass at the inlet in 2 milliseconds and the LTM applied an impact load to the components. During that time, and subsequent to it, the Lorentz side forces used the coil and LTM as a crowbar to provide enough additional overload to break the collar. The LTM then "unzippered" the VSBM/TTM subsystem.

In spite of the 0.13 m thickness, the sideplate is flexible and weak because of the vertical grooves cut into it. As a result, it might not affect the unloading process that would follow fracture of the LTM fingers. The sideplate also has a plane of weakness through the vertical groove at the

faceplate notch. The sudden upstream movement of the LTM would tend to break the plate along that groove. Also, the lateral pressure on the broken LTM would tend to throw it and the sideplate sideward. That could disengage the three vertical keys between the LTM and sideplate.

If the collar failed first then the sideplate would have been thrown free as the LTM fingers failed. The time differences involved are of the order of microseconds.

When the sideward VSBM/TTM stripping action reached the inlet region, the laternal force would tend to break the upstream collar. The LTM finger failure would occur shortly thereafter because of the sideways loading that would build up a large bending moment on the LTM with a peak at the observed fracture site. Furthermore, the compression load from the inlet end wave reflection would tend to maintain contact on the LTM at the upstream faceplate. As the LTM deflected sideward, the downstream compressive force would act on that deflection to increase the bending moment. The combination probably led to the observed upstream failure of the LTM.

The impact of the LTM on the faceplate could also account for the fracturing of the lips on the upper and lower tongues.

Lateral Lorentz forces on the bowed coil would be resisted by sideward components from tension forces in the conductors at the inlet and outlet saddles. The axial component would be resisted by the steel. The observed final position of the coil can be accounted for by that mechanism as the means of stopping the dynamic action. The copper stress would be 27,000 psi and the strain would be 0.015. The combination would be reasonably close to a representative

stress-strain curve for annealed copper at 100 K.

Using that type of stopping action, calculations were made that indicate the entire failure event occurred within 50 to 100 milliseconds.

Energy Budget

The stored magnetic energy at 4 T is approximately 160 MJ. The total fracture energy is estimated at 0.7 MJ. Plastic deformation of the copper coil could account for 7 MJ. Sliding friction of the steel masses could dissipate another 0.5 MJ. That total is approximately 8 MJ or 5 percent of the stored magnetic energy. On the other hand, the entire stored energy could be accounted for by an 8 K temperature rise in the copper coil (starting at 100 K) subsequent to the structural failure.

Future Work

The analysis leading to the above conclusions will be reviewed, refined and documented. These results will be presented as part of a workshop on the structural design basis for large superconducting magnets.

It is also interesting to consider the extent of the structural damage to a comparable superconducting magnet wherein the coils remained superconducting during the event and the total stored energy was available for mechanical deformation. This consideration will be incorporated into on-going safety and protection studies and will also be discussed at the aforementioned workshop.

REFERENCES

1. R.M. James, et al., "Investigation of an Incident During Run M1-007-018 MHD High Performance Demonstration Experiment (PWT) on December 9, 1982", ARVIN/CALSPAN Field Services, Inc. AEDC Division, Arnold Air Force Station, TN., April 1983.

2. H.J. Schmidt, et al., "Report on the MHD Performance Demonstration Experiment". For the Period October 1, 1976 to September 30, 1977. FE-1542-35. Sverdrup/Aro, Inc., March 1978.

3. Anon, "Dual Mode MHD Magnet, Vol. 2, Appedices". Magnetic Engineering Associates Report.

3.0 MAGNETIC TO KINETIC ENERGY CONVERSION FOLLOWING STRUCTURAL FAILURE

R.J. Thome and W.G. Langton

3.1 Summary

In this section, an idealized magnet structural failure problem will be analyzed to develop insight into the governing parameters, the sequence of events, and the time scale over which the events occur. The analysis is then applied to examples which show the dramatic difference in character if the coil is driven beyond its ultimate strength after the structure fails versus the case where the coil can absorb the total load without rupture even though some yielding is necessary.

The model and examples are based on an infinitely long solenoid configuration. This simple shape allows the important parameters to become apparent. The preliminary conclusions are:

(a) A protective circuit reaction involving dissipation in resistive elements following a major structural failure is unlikely to be effective on a fast enough time scale to limit the magnetic to kinetic energy conversion process in magnets using high current density windings.

(b) Windings with low enough current densities can absorb the total load following structural failure, thus limiting the kinetic energy conversion process, although this might involve substantial yielding and deformation of the winding. This is not usually a design requirement, but might form the basis for one criteria for large magnet design.

(c) Protective circuits involving inductive energy transfer can respond fast enough to limit the kinetic energy conversion process in high or low current density configurations. The range of coupling coefficients and time constants to allow this method to be effective are under study. This is the source of our interest in the use of multiple circuits for discharge of a TF coil system as begun this year and as discussed in Section 4.

The preliminary conclusions will be evaluated further as part of next years Large Magnet Safety and Protection Effort. Consideration will be given to model alteration to include non-solenoidal effects.

3.2 Model Description - Resistive Protection

Figure 3.1 shows a long thin solenoid consisting of a coil and an external structure. The coil produces a magnetic field B within the bore and has a radial build t_c and length ℓ_o. The magnetic field produces an outward radial pressure, $B^2/(2\ \mu_o)$ which is reacted by hoop tension F_c in the coil and F_s in the structure. The structure is assumed to be composed of a series of alternating strong and weak links where the latter are the conceptual equivalent of fasteners, welds or other stress concentrators in the structural material. In the model, the strong members have a radial build t_s and the weak members have a radial build, t_w. A force balance on the element shown requires:

$$F_s + F_c = \left(\frac{B^2}{2\ \mu_o}\right) r\ \ell_o \tag{3.1}$$

The stresses in the coil and structural components are related to the loads by:

$$F_s = \sigma_s\ t_s\ \ell_o = \sigma_w\ t_w\ \ell_o \tag{3.2}$$

$$F_c = \sigma_c\ t_c\ \ell_o \tag{3.3}$$

where

σ_j = hoop stress, $\quad j = s,w,c$

The coil and structure expand the same amount when the load is applied so geometric compatibility requires

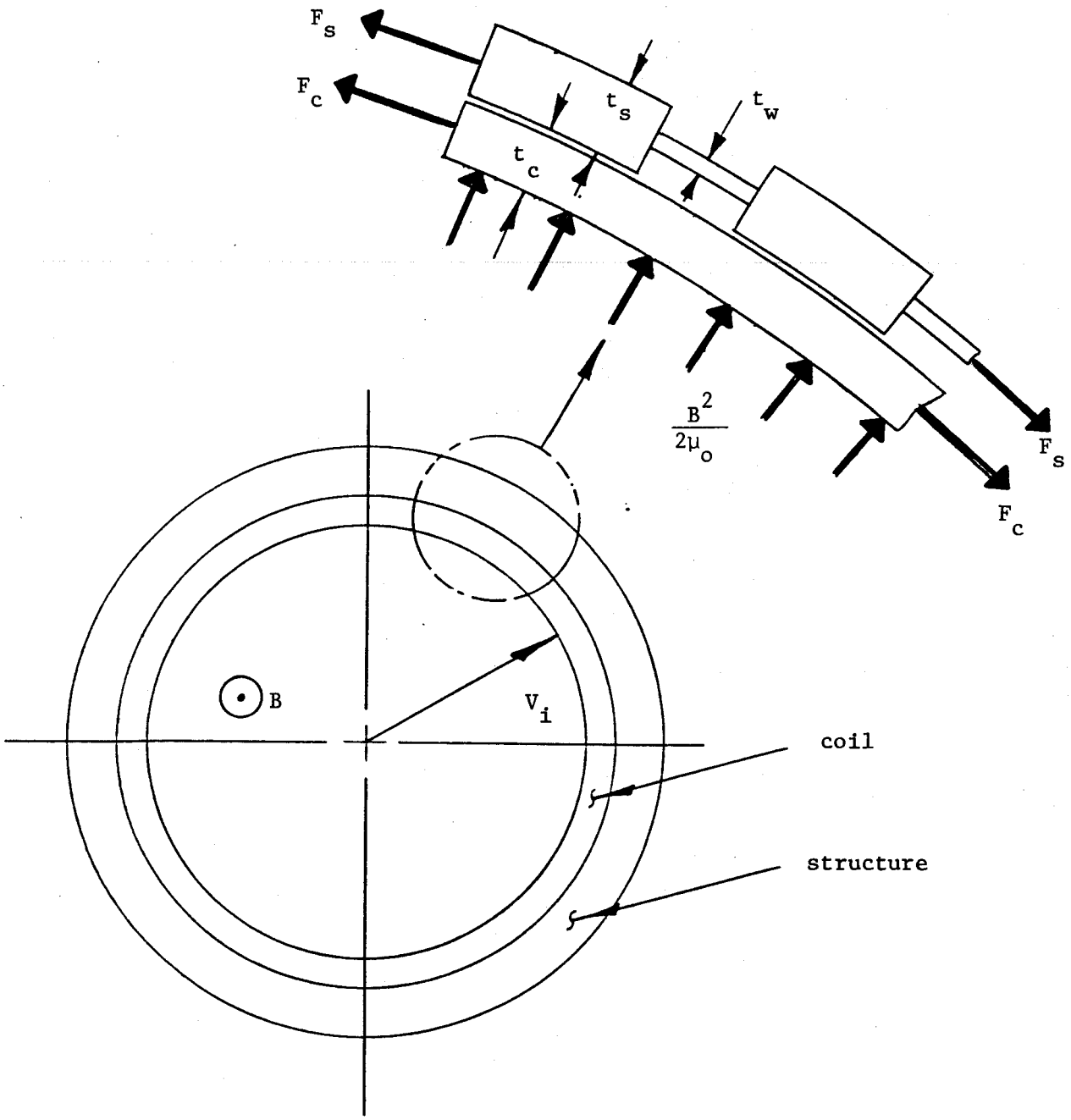

Fig. 3.1 Idealized Model of Solenoid with External Structure Having Weak Links

$$\varepsilon_c = f\,\varepsilon_w + (1-f)\,\varepsilon_s \qquad (3.4)$$

where:

ε_j = strain, $\quad j = s,w,c$

f = fraction of circumference occupied by weak links

The stress and strain in the materials are determined by the constituent relations. In this case, we will assume the ideal elastic stress-strain curves shown in Fig. 3.2a. The yield strengths for the structure and coil materials are σ_{wy} and σ_{cy}, respectively, and the ultimate strain capability of the coil corresponding to rupture is ε_u.

Figure 3.2b illustrates a typical design point without weak links where the coil and structure have the same strain and operate at some fraction of their respective yield strengths. Figure 3.2c, on the other hand, shows a possible condition for the first charge to the operating level when links are present which are weak enough (i.e., - t_w is small enough in the model) so that the links are loaded beyond yield and stretch plastically. The strain at each of the three points may be shown to be

$$\varepsilon_s = \frac{\sigma_{wy}}{E_s} \quad \frac{t_w}{t_s} \qquad (3.5)$$

$$\varepsilon_c = \left(\frac{B^2}{2\,\mu_o}\, r - \sigma_{wy}\, t_w \right) / \left(E_c\, t_c\right) \qquad (3.6)$$

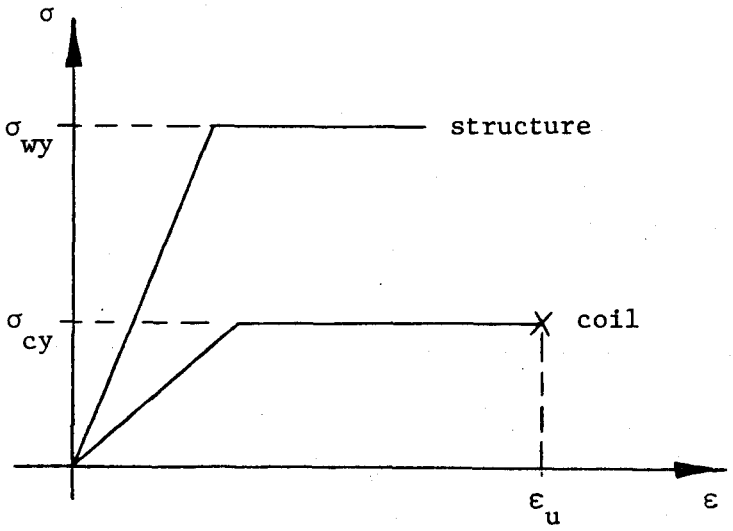

Fig. 3.2a Ideal elastic-plastic stress strain curves for the coil and structure

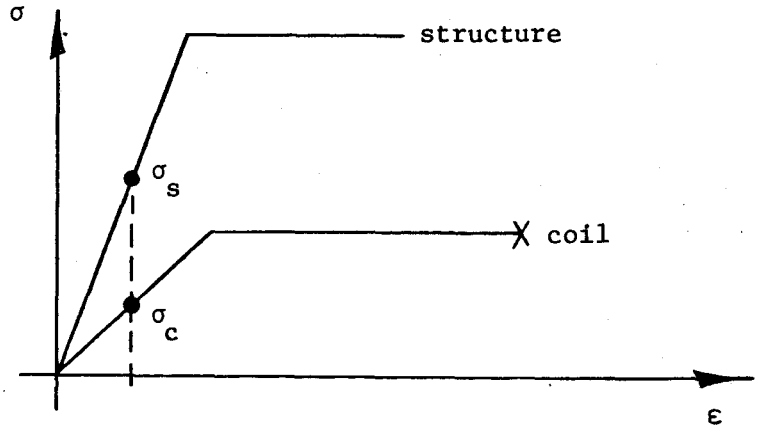

Fig.3.2b Typical design without "weak" links

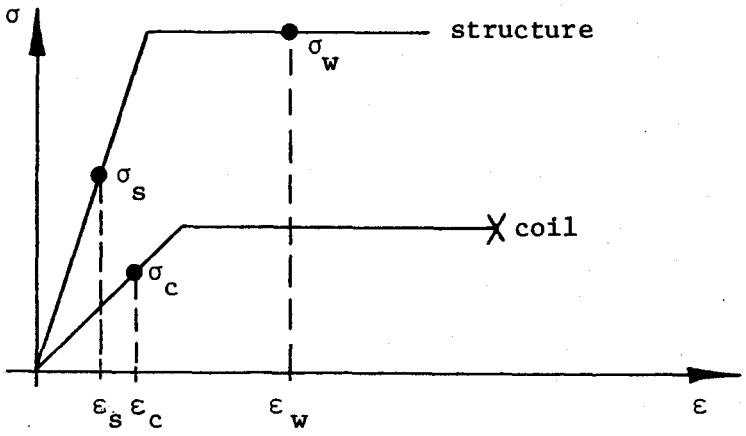

Fig. 3.2c Possible design with "weak" links

$$\varepsilon_w = f^{-1} \left[\varepsilon_c - (1-f) \ \varepsilon_s \right] \tag{3.7}$$

where

E_j = modulus of elasticity, j = s,c

If the coil is discharged, the coil and strong components of the structure recover along the same curves, but, because of the yielding at w, the weak structure recovers along a different path. This is illustrated in Fig. 3.3 . The final state is represented by points c', s', and w' in the figure which assumes that the coil cannot pull away from the structure. The coil is left with a residual tension and the structure with a residual compression such that:

$$\sigma_{c'} = \frac{\left(\varepsilon_w - \frac{\sigma_{wy}}{E_s} \right) f}{\left[\frac{1}{E_c} + \frac{(1-f)\ t_c}{E_s\ t_s} + \frac{f t_c}{E_w\ t_w} \right]} \tag{3.8}$$

$$\sigma_{s'} = - \ \sigma_{c'} \frac{t_c}{t_s} \tag{3.9}$$

$$\sigma_{w'} = \sigma_{s'} \frac{t_s}{t_w} \tag{3.10}$$

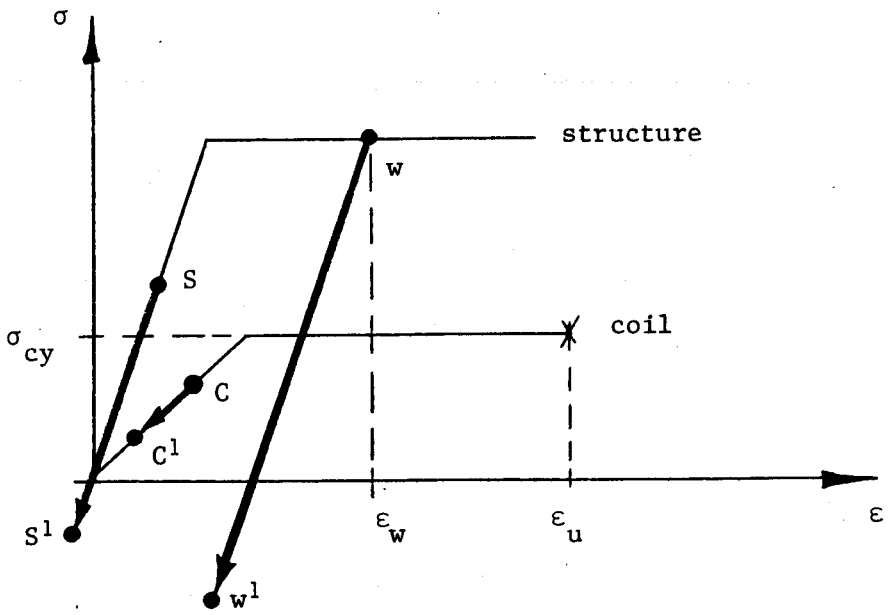

Fig. 3.3 On the first charge, the materials start at the origin and are loaded to c, s and w. On discharge s and c recover along the same curves, but because of the yielding at w, it recovers along a new curve.

If the coil is then repeatedly charged to the original point and discharged, the material will cycle between the primed and unprimed states in Fig. 3.3. Assume that, after a number of cycles, the weak links fail at t = 0 with the materials in the charged state, c, s and w, at $t = 0^-$. At t = 0 the entire electromagnetic load transfers to the coil and subsequent events depend strongly on whether the load is of sufficient magnitude and maintained for a long enough time interval to strain the coil material into the plastic range and up to its ultimate strain, ε_u, at which point the coil material also ruptures.

For simplicity, the weak links will be assumed to break simultaneously and uniformly around the periphery. Figure 3.4 then illustrates the force balance in which the electromagnetic load is accelerating the mass outward, but is restrained by the hoop tension in the coil. The force balance may be written as follows:

$$\frac{B^2}{2\mu_o} r \ell_o d\theta - 2F_{cr} \sin\left(\frac{d\theta}{2}\right) = \frac{M}{(2\pi r \ell_o)} r \ell_o d\theta \frac{d^2r}{dt^2} \qquad (3.11)$$

where:

M = total mass of coil and structure

As the coil expands radially, its cross section necks down such that

$$t_{cr} = t_c \left(\frac{r_i}{r}\right) \qquad (3.12)$$

where:

t_c = initial coil thickness when at radius, r_i

t_{cr} = coil thickness when expanded to a radius r

The restraining force, F_{cr}, provided by the coil depends on whether the coil material is in the elastic range, plastic range or beyond its

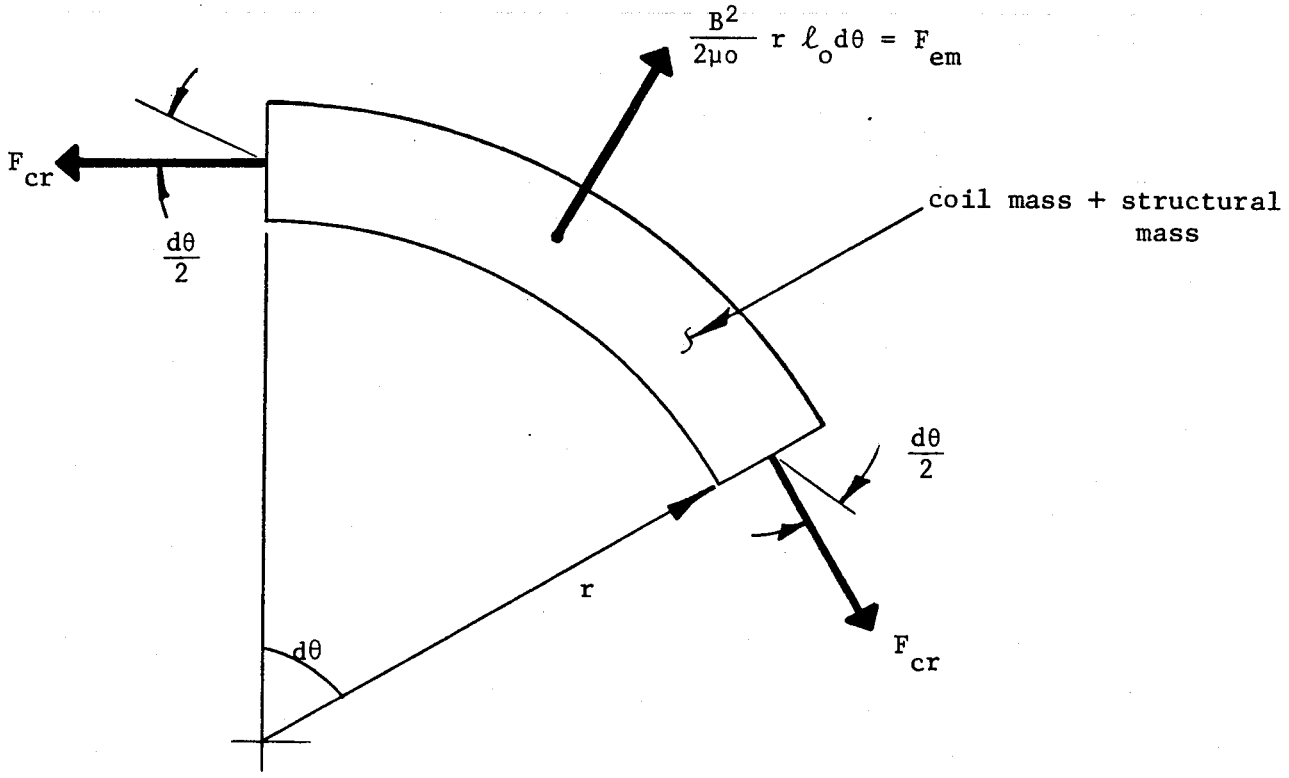

Fig. 3.4 Element of Coil and Structure Being Accelerated Radially by the Electromagnetic Force, F_{em} and Restrained by the Hoop Tension, F_{cr}, in the coil.

ultimate strain. Following the nomenclature in Fig. 3.3, this becomes

$$F_{cr} = \begin{cases} E_c\,(r/r_i-1)\,t_c\,\ell_o & \text{, if } (r/r_i-1) < \sigma_{cy}/E_c \\ \sigma_{cy}\,t_c\,\ell_o & \text{, if } (r/r_i-1) > \sigma_{cy}/E_c \\ 0 & \text{, if } (r/r_i-1) > \varepsilon_u \end{cases} \tag{3.13}$$

The electromagnetic force is determined by B which is dependent on the current in the coil and the circuit characteristics. Assume the circuit to be the coil with an initial inductance, L_o, in series with a resistor R(t) which can be later specified to characterize a superconducting coil with a discharge resistor or a conventional resistive coil. For an infinitely long coil, the inductance is proportional to the bore area, hence, as the coil expands its inductance changes such that

$$L = L_o \frac{r^2}{r_i^2} \tag{3.14}$$

where:

L_o = coil inductance when its radius is r_i

The circuit equation is given by

$$\frac{d}{dt}(LI) + IR(t) = 0 \tag{3.15}$$

Equations (3.11) to (3.15) may now be combined and normalized to produce the following governing equations.

$$\eta^2 \frac{dI_n}{d\tau} + 2I_n \eta \frac{d\eta}{d\tau} + I_n R_n = 0 \qquad (3.16)$$

$$\eta I_n^2 - F_o \gamma = \frac{d^2 \eta}{d\tau^2} \qquad (3.17)$$

where:

η = r/r_i

I_n = I/I_o

I_o = initial current

τ = t/τ_o

$$\tau_o = \sqrt{\frac{M r_i}{2 \pi r_i \ell_o B_o^2/(2 \mu_o)}} \qquad (3.18)$$

L_o = initial inductance

R_o = characteristic resistance = L_o/τ_o

R_n = $R(t)/R_o$

$R(t)$ = coil resistance as f(t)

$$\gamma = \begin{cases} \dfrac{E_c}{\sigma_{cy}} (\eta - 1) & \text{if } (\eta - 1) < \sigma_{cy}/E_c \\ 1 & \text{if } (\eta - 1) > \sigma_{cy}/E_c \\ 0 & \text{if } (\eta - 1) > \varepsilon_u \end{cases} \qquad (3.19)$$

$$F_o = \frac{\sigma_{cy} t_c \ell_o}{\left(\dfrac{B^2}{2 \mu_o}\right) r_i \ell_o} \qquad (3.20)$$

The independent variable in (3.16) and (3.17) is τ, the normalized time, the dependent variables are η, the normalized radius and I_n, the normalized current; R_n is a normalized resistance which can be a specified function to allow different discharge characteristics to be studied; γ is a function of η which determines if the restraining force supplied by the coil is in the elastic or plastic range or if the coil has been strained to rupture. F_o is a parameter determined by the characteristics of the coil structural system. It is a measure of the maxiumm load carrying capabilities of the coil relative to the initial magnetic load. The characteristic time, τ_o, is a measure of the time required to accelerate the entire mass of the system a distance r_i under the action of the total magnetic force initially available.

The resistance function R_n is normalized to $R_o = L_o/\tau_o$. If, for example, the coil were superconducting without a dump resistor and with its terminals essentially short circuited through its power supply then $R_n = 0$; if the coil were superconducting with a dump resistor, R_i in the circuit or if it were a conventional coil with a constant resistance then $R_n = R_i \tau_o/L_o$; if the coil were an expanding conventional solenoid with an initial resistance R_i and its cross-section necking down uniformly according to (3.12) then $R_n = (R_i \tau_o/L_o)(r/r_i)^2$. Since L_o/R_i would be the usual discharge time constant for these cases, we can define $\tau_d = L_o/R_i$ and rewrite these different cases as follows:

$$R_n = \begin{cases} 0 & \text{, if circuit resistance is zero throughout transient (eg - superconducting)} \\ \tau_o/\tau_d & \text{, if circuit has constant resistance } R_i \text{ throughout transient} \\ (\tau_o/\tau_d)\,\eta^2 & \text{, if coil has initial resistance } R_i \text{ and "necks down" during transient according to (3.12)} \end{cases} \tag{3.21}$$

Note that τ_o is determined by the mass and initial magnetic condition of the system and that the system circuit resistance cannot have much effect on the transient if $\tau_o \ll \tau_d$. This is illustrated in Section 3.3 together with the effect of the parameter F_o which determines whether the system strains beyond the ultimate strain and fractures or whether it is contained.

If $\tau_o \ll \tau_d$, then the resistance is ineffective and the coil current changes during the coil expansion so as to maintain constant flux linkage. Hence, for the solenoid in Fig. 3.1, the final field in the coil just before fracture is given by:

$$B_f = B/(1 + \varepsilon_u)^2 \tag{3.22}$$

and the stored magnetic energy per unit length just before fracture which is available for conversion to kinetic energy is:

$$E_f/\ell_o = (B_f^2/2\mu_o)\,\pi\, r_i^2\,(1 + \varepsilon_u)^2 \tag{3.23}$$

For the general case, the governing equations are non-linear but can be solved numerically by writing them in finite difference form and integrating forward in time. The approach assumes that the net force is constant during any interval $\Delta\tau$ and may be summarized as follows:

$$\left.\frac{d\eta}{d\tau}\right|_{m+1} = \left.\frac{d\eta}{d\tau}\right|_{m} + \Delta\tau \left[I_m^2 \eta_m - F_o \gamma_m\right] \tag{3.24}$$

$$\eta_{m+1} = \eta_m + \Delta\tau \left.\frac{d\eta}{d\tau}\right|_{m} \frac{(\Delta\tau)^2}{2} \left[I_m^2 \eta_m - F_o \gamma_m\right] \tag{3.25}$$

$$I_{m+1} = I_m \left\{ 1 - \Delta\tau \left[\frac{2}{\eta_{m+1}} \left.\frac{d\eta}{d\tau}\right|_{m+1} + R_{m+1} \left(\frac{1}{\eta_{m+1}}\right)^2 \right] \right\} \tag{3.26}$$

The initial conditions required to start the iteration are $I = 1$, $\eta = (1 + \varepsilon_c)$ and $\dfrac{d\eta}{d\tau} = 0$ at $\tau = 0$.

Equations (3.24) to (3.26) are in finite difference form and utilize simple forms for R_n (see 3.21) and γ (see 3.19). Since the procedure is numerical, more complex forms could be used if desired. For example, γ could be based on more realistic stress-strain relationships than the "ramps" shown in Fig. 3.3. The simplified model, however, is easier to visualize and illustrates the underlying physical interactions.

3.3 Model Description - Inductive Protection

The previous section considered the possibility of restraining the magnetic to kinetic energy conversion process by dissipating the magnetic energy in a resistor in the main coil circuit. This requires that the usual

discharge time constant, τ_d be of the same order as τ_o, the characteristic time for the magnetic force to accelerate the system mass. In many (perhaps most) cases this will be impractical because of the rapid response time and/or high voltages required to effect the discharge. In this section, therefore, we consider the possibility of restraining the energy conversion process by transferring some of the magnetic energy to another circuit which is inductively coupled to the first.

The presence of the secondary circuit alters (3.15) as follows:

$$\frac{d}{dt}(LI) + IR(t) + \frac{d}{dt}(MI_2) = 0 \tag{3.27}$$

where

M = mutual inductance between the original winding and the second circuit or electrically conducting body

I_2 = current in second circuit

A second electrical equation is required because of the second circuit.

$$L_2 \frac{dI_2}{dt} + \frac{d}{dt}(MI) + I_2R_2 = 0 \tag{3.28}$$

where

L_2 = self inductance of second circuit

R_2 = resistance of the second circuit

Equation (3.28) may be written in normalized form.

$$\frac{dI_{2n}}{d\tau} + \frac{d}{d\tau}\left(\frac{M}{L_2} I_n\right) + I_{2n}\left(\frac{\tau_o}{\tau_2}\right) = 0 \tag{3.29}$$

where

$I_{2n} = I_2/I_o$

$\tau_2 = L_2/R_2$

If we now assume $(\tau_o/\tau_2) \ll 1$, that is, that the time constant of the secondary is long compared to the characteristic time τ_o then (3.29) implies;

$$\frac{dI_{2n}}{d\tau} = -\frac{d}{d\tau}\left(\frac{M}{L_2} I_n\right) \tag{3.30}$$

In general, the force balance given by (3.11) would require a term added to the left side of the form

$$\frac{I}{\ell_o} B_2 \, rd\theta\ell_o \tag{3.31}$$

where

B_2 = field at solenoid segment in Fig. 3.1 due to current in second circuit

However, for the special case shown in Fig. 3.5, the second circuit is a passive infinitely long conducting shell inside the bore of the infinite solenoid. In this configuration, any current in the shell produces no field outside the shell and, specifically, $B_2 = 0$ at the winding so (3.31) is zero and the governing mechanical equation is (3.17) as it was in the previous section.

Furthermore, the mutual inductance between the shell and the winding may be shown to be a constant for this configuration even if the winding is expanding in time. Equation (3.29) and (3.30) may then be combined to yield the following electrical equation for this case.

$$(1 - k^2 \eta^{-2}) \eta^2 \frac{dI_n}{d\tau} + 2 I_n \eta \frac{d\eta}{d\tau} + I_n R_n = 0 \tag{3.31}$$

where

$k^2 = \frac{M}{L_2 L_o}$ = coupling coefficient

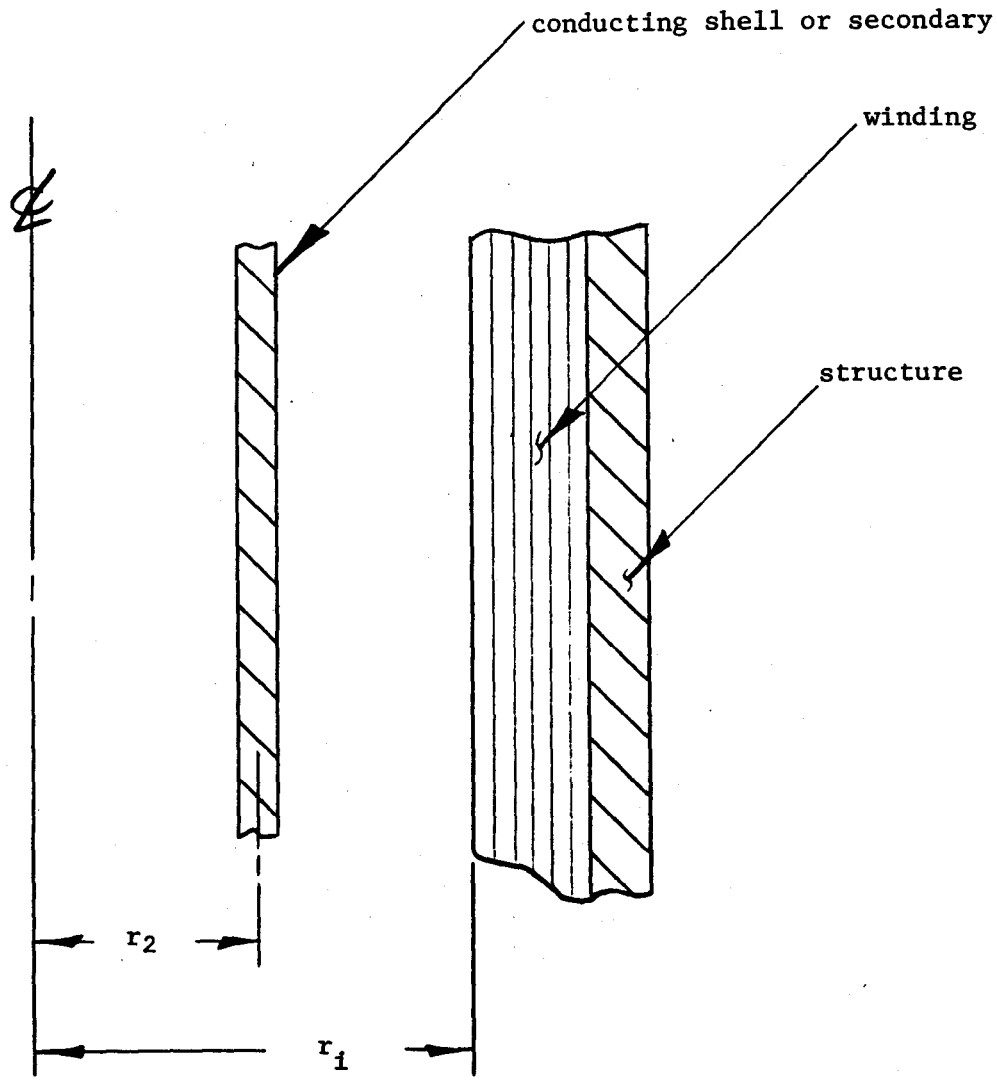

Fig. 3.5 Simple model of a conducting shell (or secondary) capable of trapping magnetic flux when the structure fails and winding expands radially.

Equation (3.31) is the same as (3.16) except for the multiplier on the leading term which causes a more rapid rate of change of I_n than if $k^2 = 0$ as it is in the previous section. Equation (3.30) then implies that this causes the current in the secondary to change at the same rate, hence, energy is transfered into the secondary.

The examples in Section 3.4 will show that the inductive energy transfer can be effective in restraining the conversion of the field energy to kinetic energy provided the coupling coefficient is sufficiently high. The model is simple but illustrates the basic concepts. Next year, consideration will be given to extending the analysis by relaxing some of the simplifying assumptions.

3.4 Solenoid Examples

3.4.1 Resistive Protection

As a hypothetical example, assume a long solenoid as in Figure 3.1 with a field B = 10 T and bore radius of 1 m. The winding build, t_c, and other characteristics are dependent on the overall current density, hence, consider two cases as outlined in Table 3.1.

Case 1 is for a relatively high current density and Case 2 is for a moderate to high level. They lead to substantially different values for t_c. The structural build, t_s, is based on a stress $\sigma_s = 4 \times 10^4$ psi. The total mass is that of the structure based on a steel density of 7.8×10^3 kg/m^3 and the winding based on 8.9×10^3 kg/m^3 with a packing factor of 0.7 applied to the latter. If a operating current level of 2×10^4 A is chosen then the inductance and stored energy per unit length can be shown to be 0.625 H/m and 125 MJ/m, respectively. The ratio of winding modulus to yield strength was

TABLE 3.1
SOLENOID CHARACTERISTICS

CASE	1	2
Magnetic Field, [T]	10	10
Bore Radius, [m]	1.0	1.0
Winding Current Density, [$10^7 A/m^2$]	3.3	1.86
Winding Radial Build, t_c	0.241	0.482
Structural Build, t_s [m]	0.168	0.182
Total Mass Per Unit Length, M/ℓ_o, [kg/m]	2.51×10^4	3.39×10^4
Operating Current, [kA]	20	20
Inductance Per Unit Length, L_o/ℓ_o, [H/m]	0.625	0.625
Stored Energy Per Unit Length, E/ℓ_o, [J/m]	1.25×10^8	1.25×10^8
Winding Modulus/Yield Stress, E_c/σ_{cy}	900	900
Winding Strain, ε_c	5×10^{-4}	5×10^{-4}
Characteristics Time, τ_o [s]	9.28×10^{-3}	1.17×10^{-2}
Load Characteristic, F_o	0.562	1.0
Winding Ultimate Strain, ε_u	0.2	0.2

assumed to be 900 and the ultimate winding strain at fracture was assumed to be 20%. In both cases the initial strain in the winding at operating current level was taken as 5×10^{-4}. The characteristic time may now be found using (3.18) and, as indicated in the table, is about 10 msec for each case. This is representative of the time required for the stored magnetic energy to accelerate the system mass and is quite rapid. The yield stress for the winding was assumed to be $\sigma_{cy} = 0.7\ (2 \times 10^4) = 1.4 \times 10^4$ psi. This value, together with some of the characrteristics found earlier, allow F_o to be found. Equation (3.20) indicates that F_o, the load characteristic, is a measure of the load carrying ability of the winding alone, at yield, relative to the magnetic load. Since it is substantially less than one for Case 1 and unity for Case 2, we expect the two cases to respond quite differently in the event of a structural failure.

Figures 3.6, 3.7 and 3.8 show the response for Case 1 following a structural failure at $t = 0$. The abscissa in each figure is time normalized to τ_o which is $\approx$ 10 ms as indicated in Table 3.1. Figure 3.6 shows the current in the coil normalized to the initial current and the transient which results for four different values of (τ_o/τ_d), the ratio of the characteristic time to the usual discharge time constant, $\tau_d = L_o/R_i$. The case of $(\tau_o/\tau_d) = 0$ corresponds to a zero resistance situation and increasing (τ_o/τ_d) implies circuitry with successively larger coil resistances. Note that the transient is well underway in only two times the characteristic time, τ_o. The normalized radial displacement is shown in Fig. 3.7 over the same time period and illustrates substantially different reactions depending on the value of (τ_o/τ_d). Higher values of (τ_o/τ_d) generate a condition where sufficient energy is dissipated rapidly enough in the resistance to limit the deformation. However, low values result in a deformation which is not limited. The critical condition

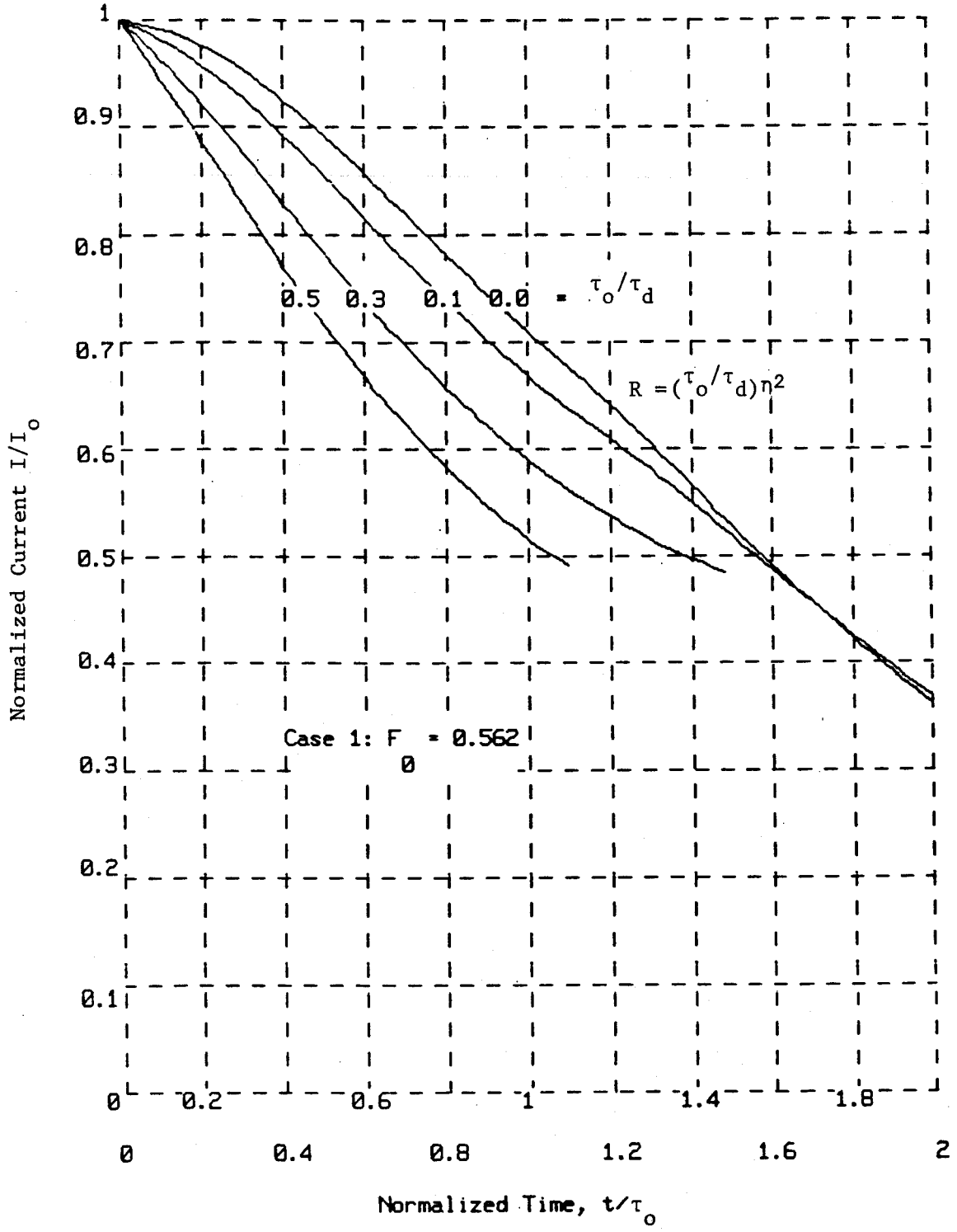

Figure 3.6 - Normalized Current vs Time for Case 1 and Selected Values of (τ_o/τ_d).

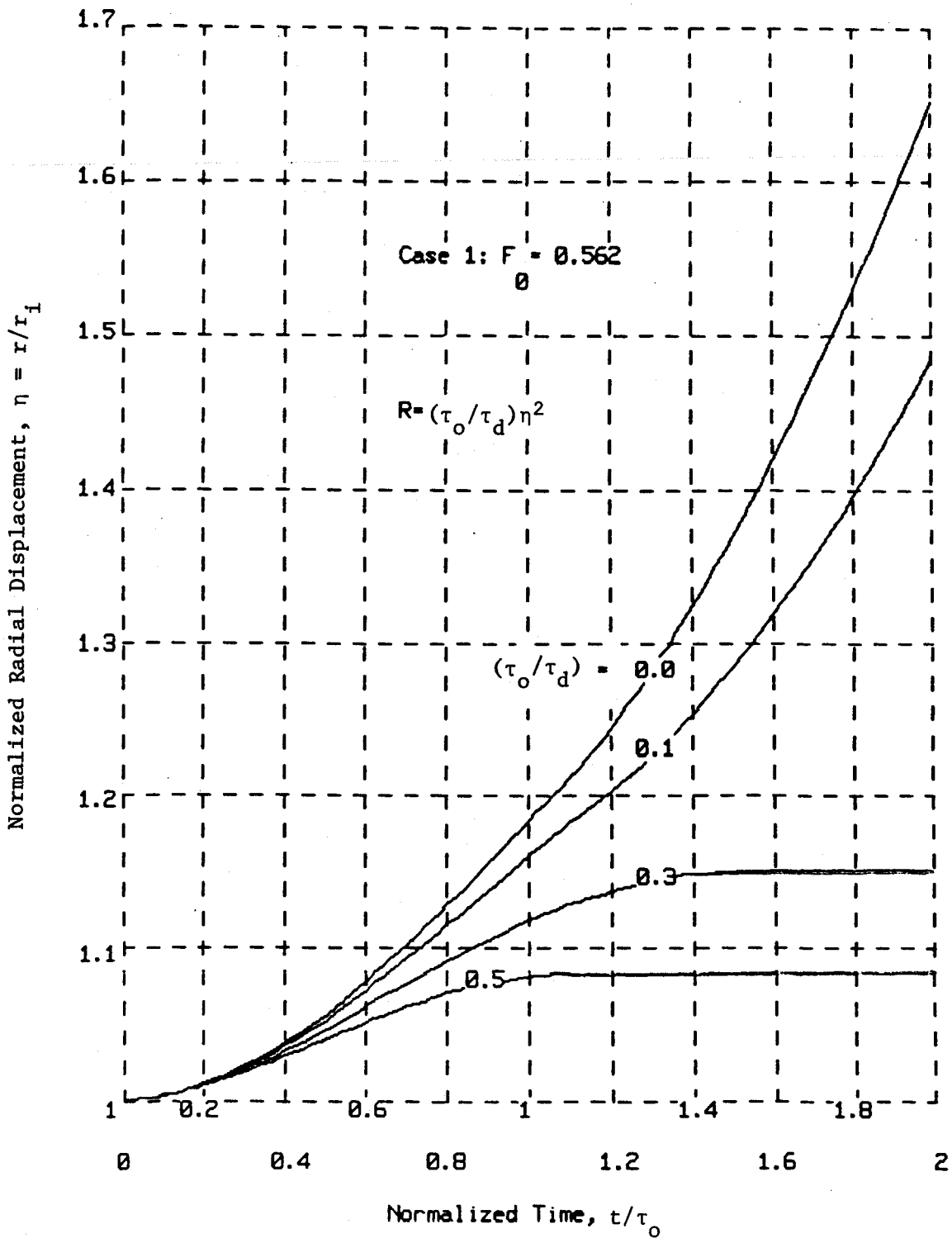

Figure 3.7 – Normalized Radial Displacement vs Time for Case 1 and Selected Values of τ_o/τ_d.

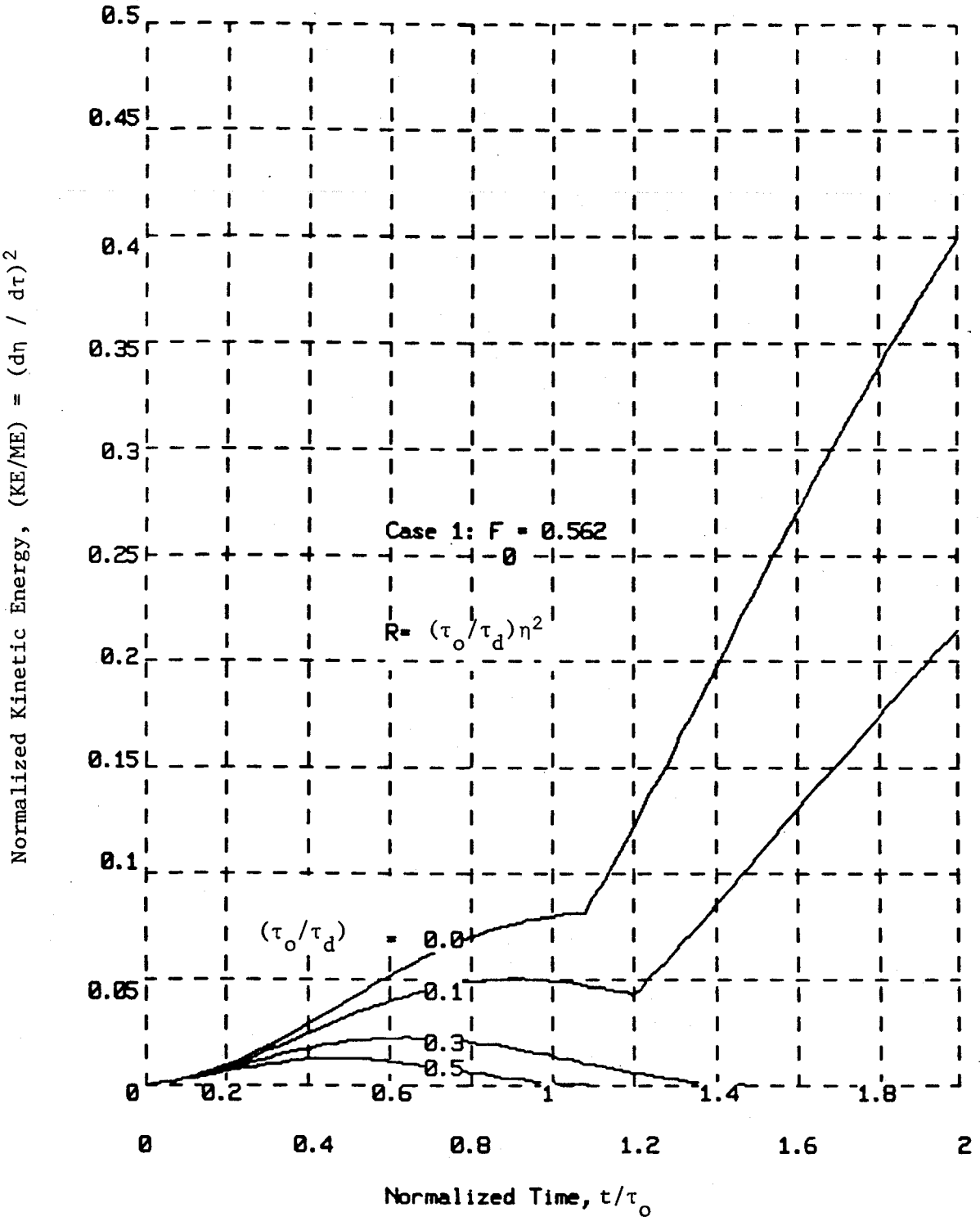

Figure 3.8 - Normalized Kinetic Energy vs Time for Case 1.

occurs when the ultimate winding strain, ε_u is exceeded. In these examples, $\varepsilon_u = 0.2$, therefore, if conditions are such that $\eta \approx 1 + \varepsilon_u \approx 1.2$ we would expect the winding to rupture and no restraint on conversion of the remaining magnetic energy to kinetic. This is shown in Fig. 3.8 which is a plot of the instantaneous kinetic energy per unit length normalized to the magnetic energy per unit length initially stored at $t = 0^-$. For high enough (τ_o/τ_d) the kinetic energy starts at zero, rises to a maximum and decreases to zero. However, if the energy is not dissipated fast enough, that is, if (τ_o/τ_d) is low enough, then the coil ruptures and the unrestrained magnetic to kinetic energy conversion occurs. Note that the sudden change in slope in Fig. 3.8 occurs at the time when the radial displacement in Fig. 3.7 passes through $\eta \approx 1.2$ where the ultimate winding strain is exceeded.

Case 1 illustrates that the unrestrained conversion of magnetic to kinetic energy can be averted even if $F_o < 1$ provided the usual discharge time constant is of the same order as τ_o. In many cases, however, this would require unrealistically high voltages and unrealisticially fast circuit response times since τ_o is likely to be small. As a result we will conclude preliminarily that a response involving resistive dissipation alone is not feasible. Next year this shall be investigated further to relate τ_o, τ_d and the required voltage to system characteristics.

It was noted earlier that a different response would be expected for Case 2 because $F_o = 1$. This is illustrated in Figs. 3.9, 3.10 and 3.11 which have axis labels corresponding to those discussed for Case 1. Figure 3.9 shows the normalized current transients for the same values of (τ_o/τ_d) as used in the previous case. Note from Table 3.1 that $\tau_o \approx 10$ msec for Case 2 also.

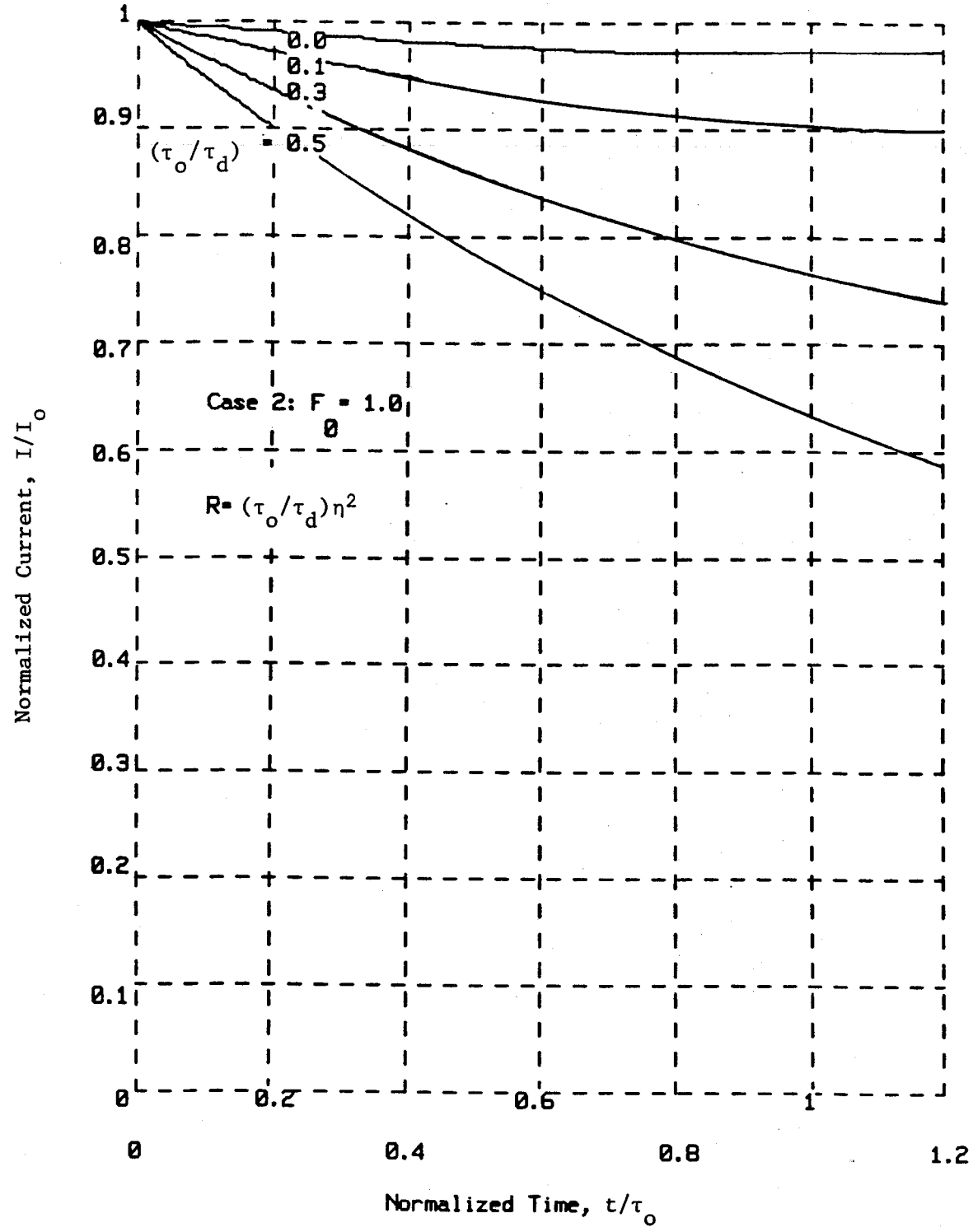

Figure 3.9 - Normalized Current vs Time for Case 2.

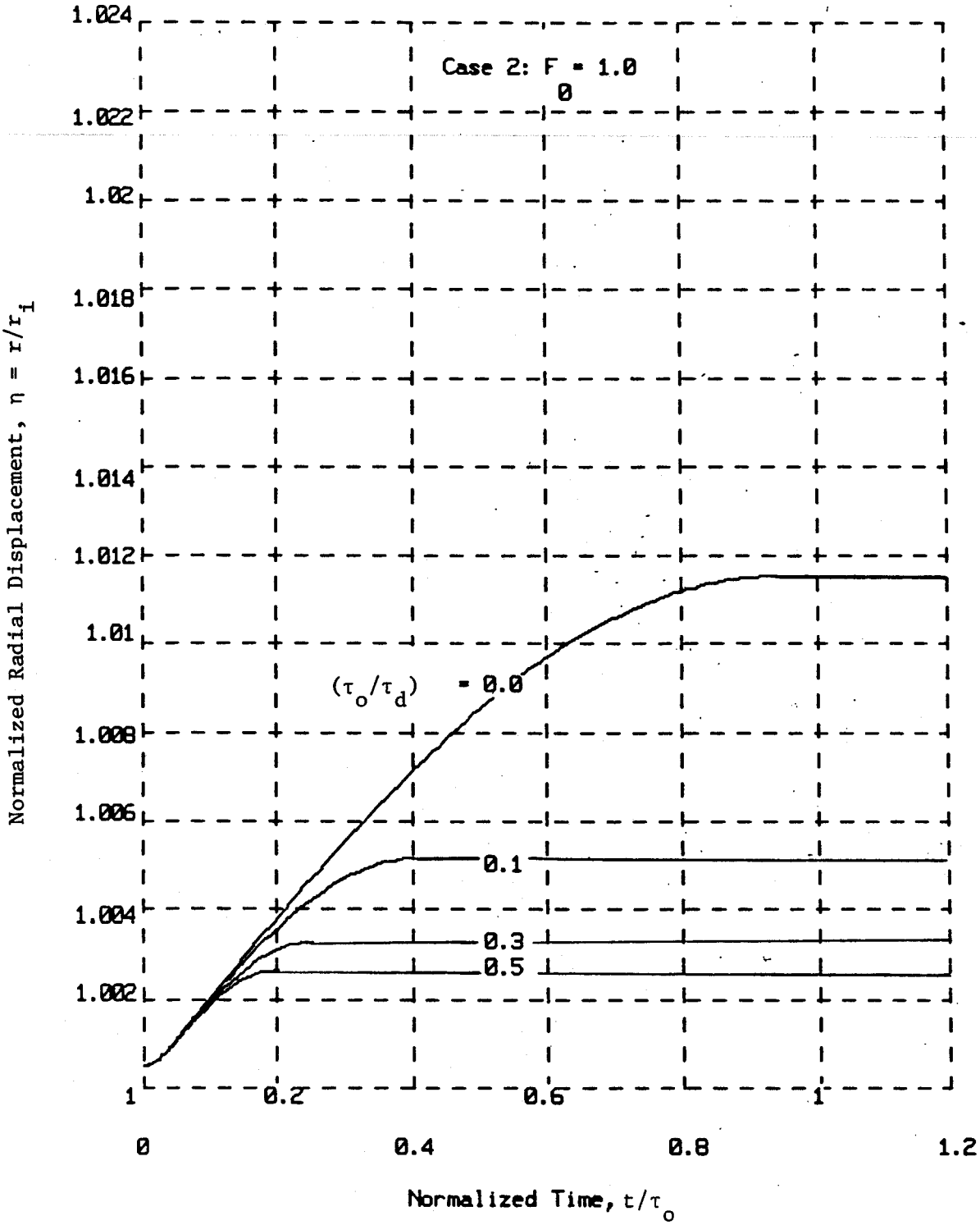

Figure 3.10 - Normalized Radial Displacement vs Time for Case 2.

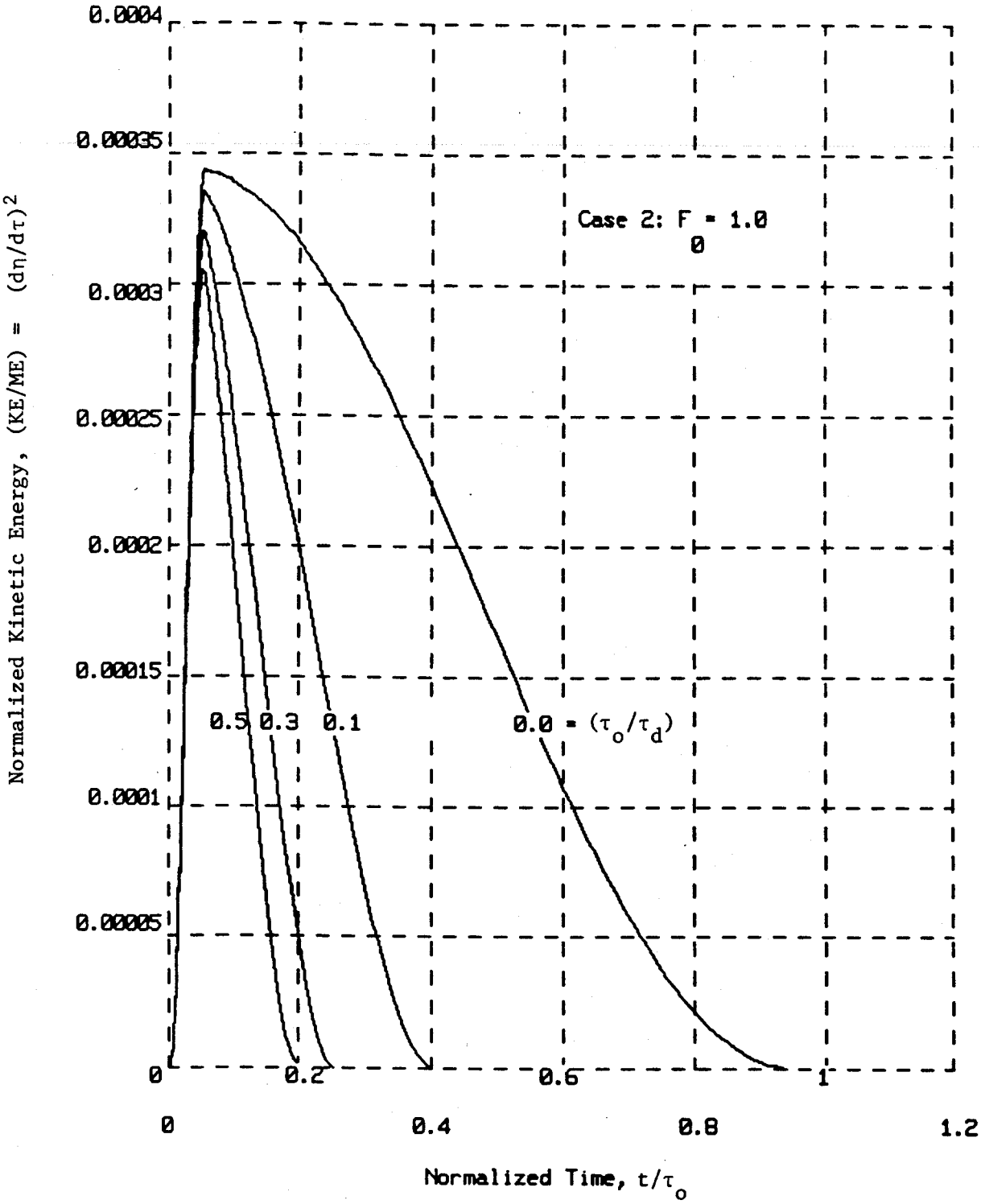

Figure 3.11 – Normalized Kinetic Energy vs Time for Case 2.

The normalized radial displacement is shown in Fig. 3.10 and is limited for all (τ_o/τ_d) because F_o is large enough for the winding to have sufficient strength to accept the load after the structure fails at t = 0. However, even though the winding strain does not reach the rupture condition (i.e. $\eta = 1 + \varepsilon_u \approx 1.2$), some yielding must occur at the levels indicated. Since $E_c/\sigma_{cy} = 900$, yielding would be expected at about $\eta = 1 + (900)^{-1} \approx 1.001$, hence all of the cases shown cause the winding to yield plastically. Figure 3.11 gives the normalized kinetic energy which returns to zero for all cases, including $(\tau_o/\tau_d) = 0$. The break in the kinetic energy curves occurs at the yield point where the functional form of the restraining force by the winding changes form (see (3.19)).

Case 2 shows that a coil with a high enough F_o can restrain the magnetic to kinetic energy conversion process even if the resistive dissipation is zero (i.e. $(\tau_o/\tau_d) = 0$) although yielding and winding deformation may take place. It may be possible to translate this into a safety oriented design criteria for coils of a more complex geomerty than the ideal solenoid, hence, this will be investigated next year.

Case 1 will now be reconsidered with successively larger values of F_o and with $(\tau_o/\tau_d) = 0$ to show the change in results as the load characteristic, F_o, is varied. Figures 3.12 and 3.13 show the normalized current and radial displacement vs time, respectively. Figure 3.13 indicates that the displacement corresponding to ultimate winding strain (i.e., $\eta \approx 1.2$) is exceeded for $F_o \leq 0.82$. This is confirmed in Fig. 3.14 which shows that the conversion to kinetic energy is unrestrained for $F_o \leq 0.82$. The case of $F_o = 0.8$ is particularly interesting since it represents a case where sufficient energy can be absorbed by the coil deformation to cause the kinetic energy to pass through a

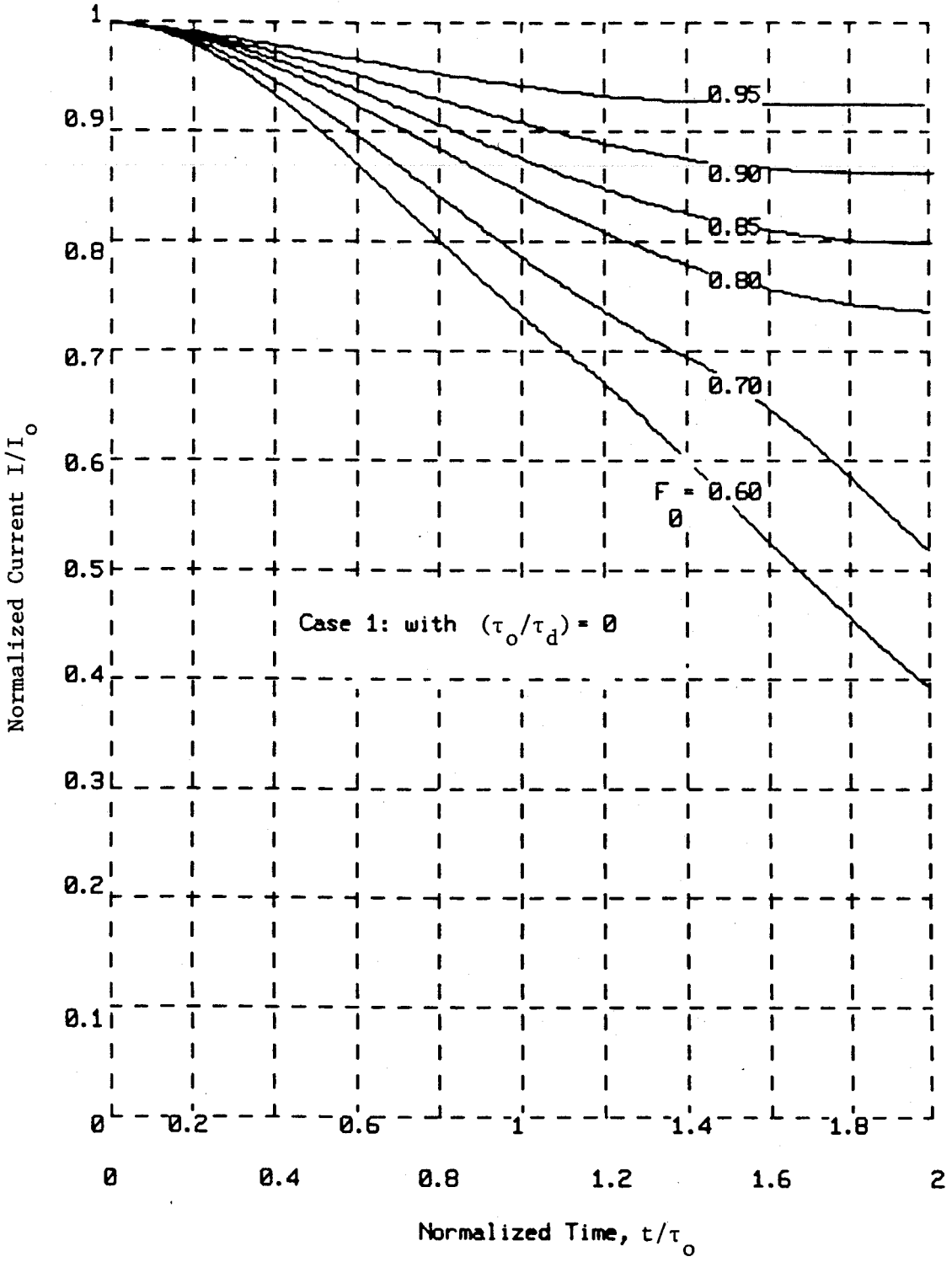

Figure 3.12 - Normalized Current vs Time for Case 1 with various Values of F_0 and $(\tau_o/\tau_d) = 0$

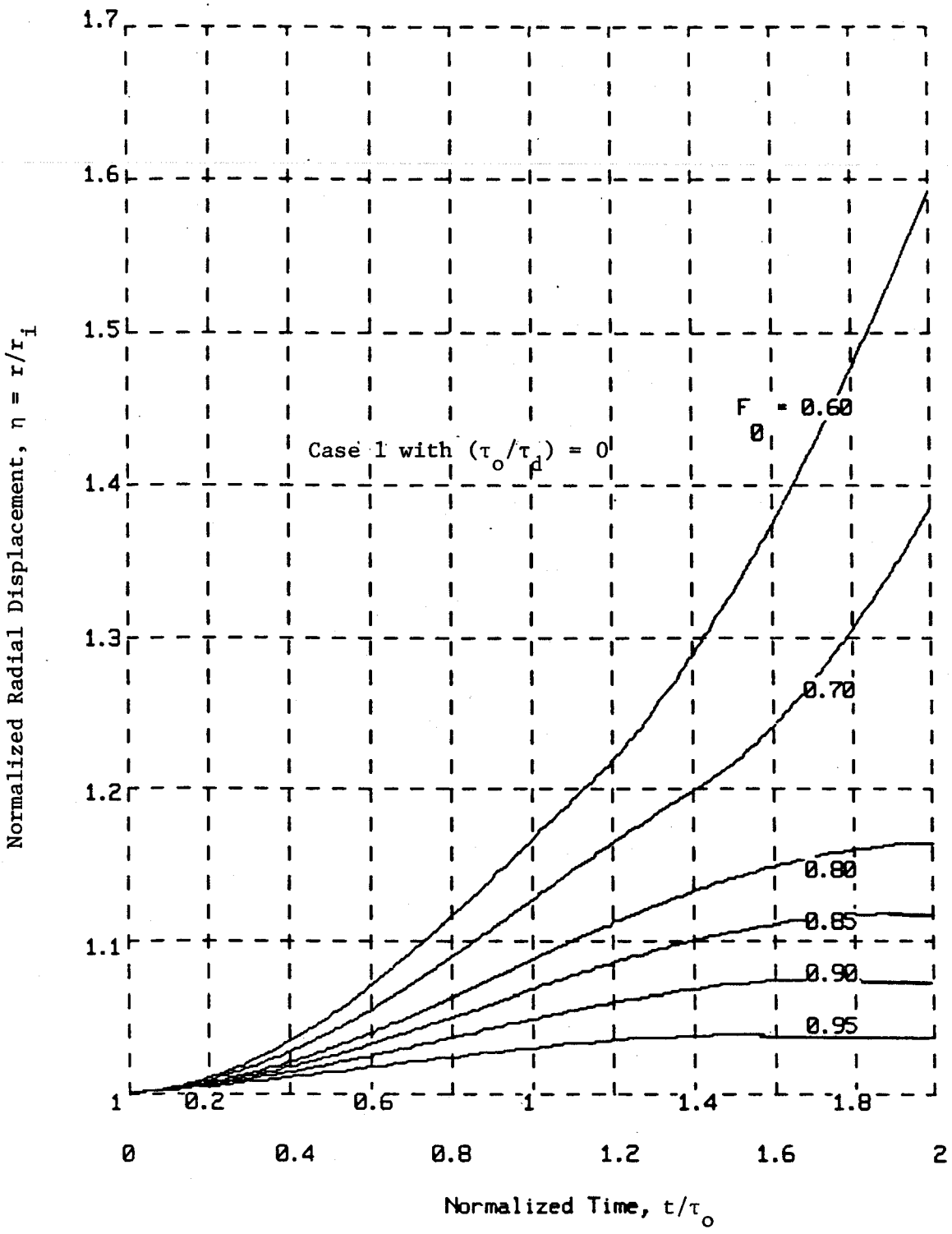

Figure 3.13 – Normalized Radial Displacement vs Time for Case 1 with Various Values of F_0 and (τ_o/τ_d) =0.

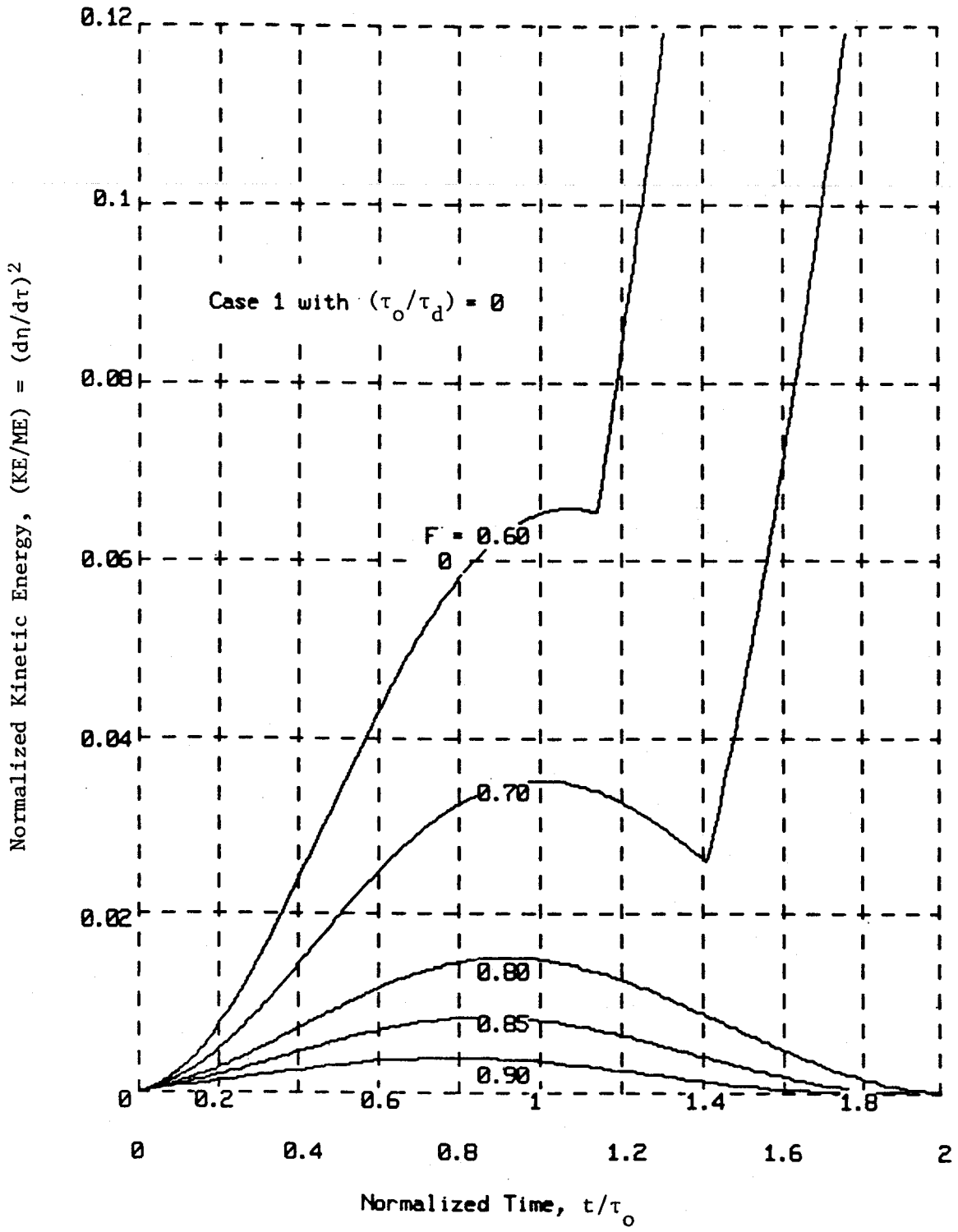

Figure 3.14 – Normalized Kinetic Energy vs Time for Case 1 with Various Values of F_0 and $(\tau_o/\tau_d) = 0$

local maximum and start to decrease, however, the ultimate strain is eventually achieved at the sudden change in slope on this curve and the winding ruptures.

3.4.2 Inductive Protection

This section will illustrate the ability of a secondary circuit to prevent unrestrained expansion even if $F_o < 1$ provided the coupling coefficient between the primary and secondary circuits is sufficiently high. The winding and structural characteristics in this example correspond to $F_o = 0.7$ and $R = 0$ for the primary circuit which leads to unrestrained conversion of magnetic to kinetic energy as shown in Fig. 3.14, which corresponds to a coupling coefficient of zero.

For the simple case shown in Fig. 3.5, the coupling coefficient may be shown to be

$$k^2 = \frac{M^2}{L_o L_2} \tag{3.32}$$

$$k^2 = \left(\frac{r_2}{r_i}\right)^2 \tag{3.33}$$

Equation (3.33) has a particularly simple form for this geometry and is limited to the range $0 < k^2 < 1.0$.

The results for this case are plotted in Figs. 3.15 to 3.17 for selected values of coupling coefficient, k^2. Figure 3.15 shows that the presence of the secondary ($k^2 \neq 0$) allows the current in the winding to fall faster initially and that this effect can occur on the fast time scale which is of the order of τ_o. Figure 3.16 shows that if k^2 is high enough (i.e., $k^2 > 0.4$ for this case) then the radial displacement is limited because the ultimate winding strain, corresponding to $\eta = 1.2$ in this figure, is not attained. This is also indicated in Fig. 3.17 which shows that the magnetic to kinetic energy conversion

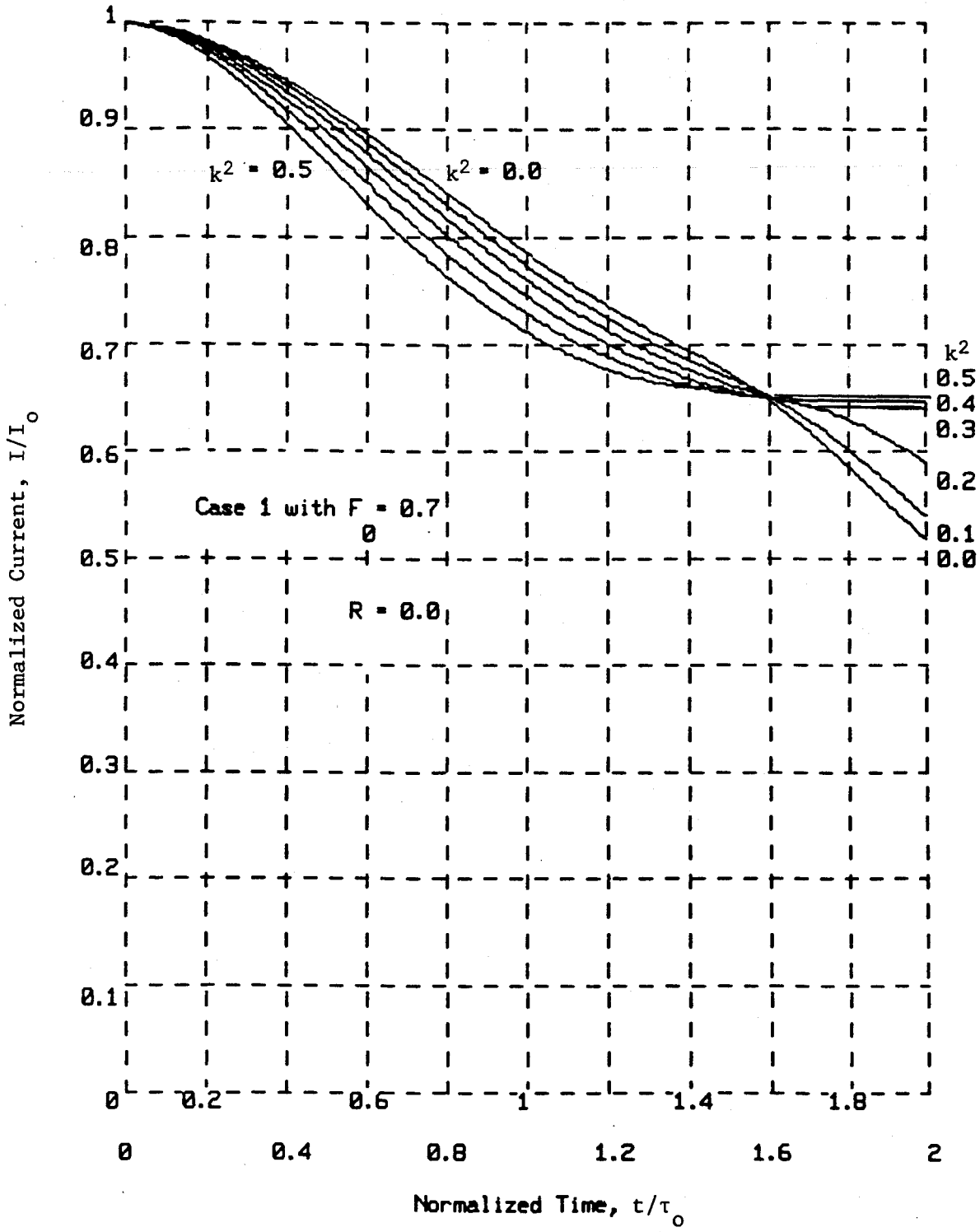

Figure 3.15 – Normalized Current vs Time for F_0 = 0.7, R = 0 and Selected Coupling Coefficients, k^2.

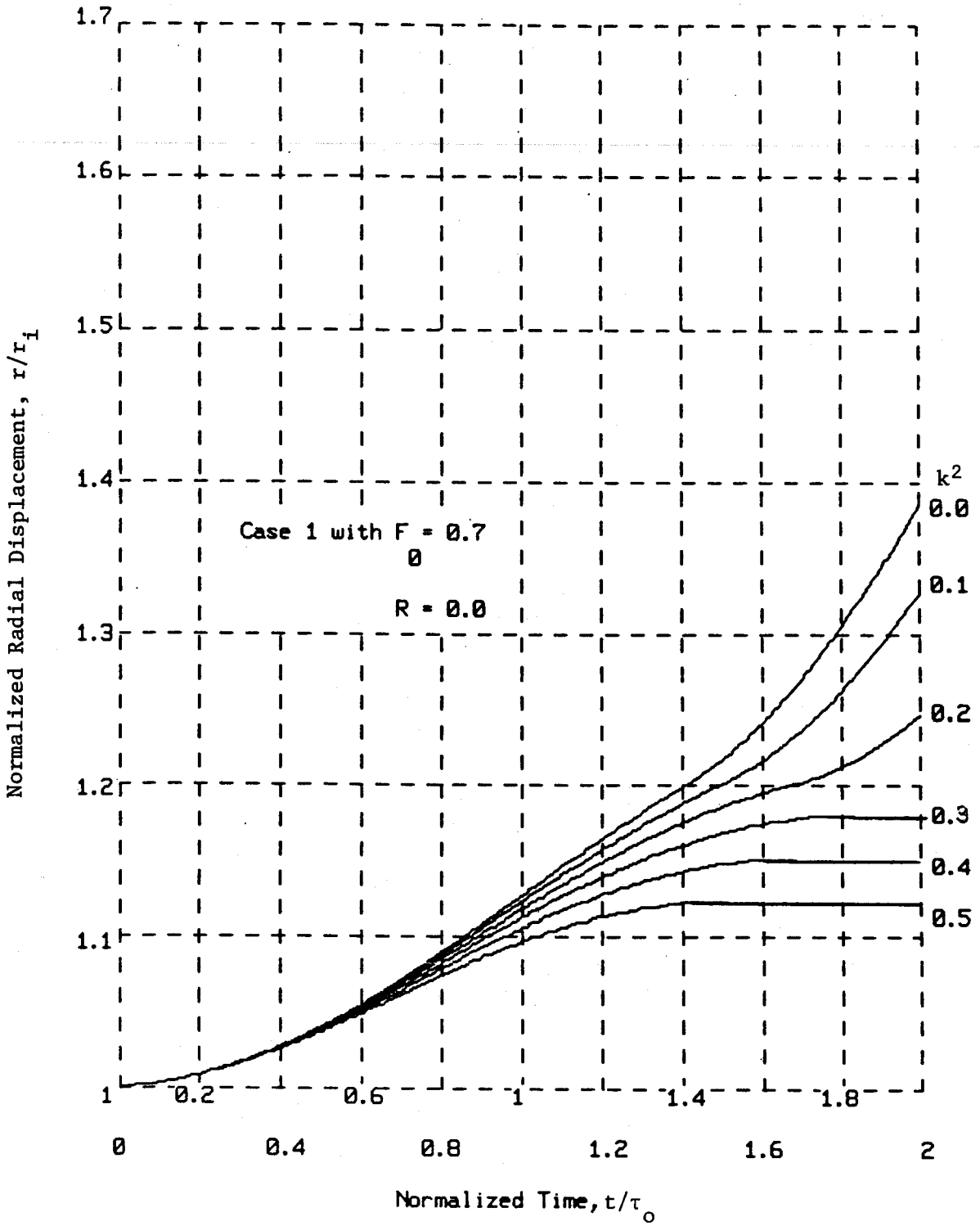

Figure 3.16 - Normalized Radial Displacement vs Time for F_0 = 0.7, R = 0 and Selected Values of Coupling Coefficient, k^2.

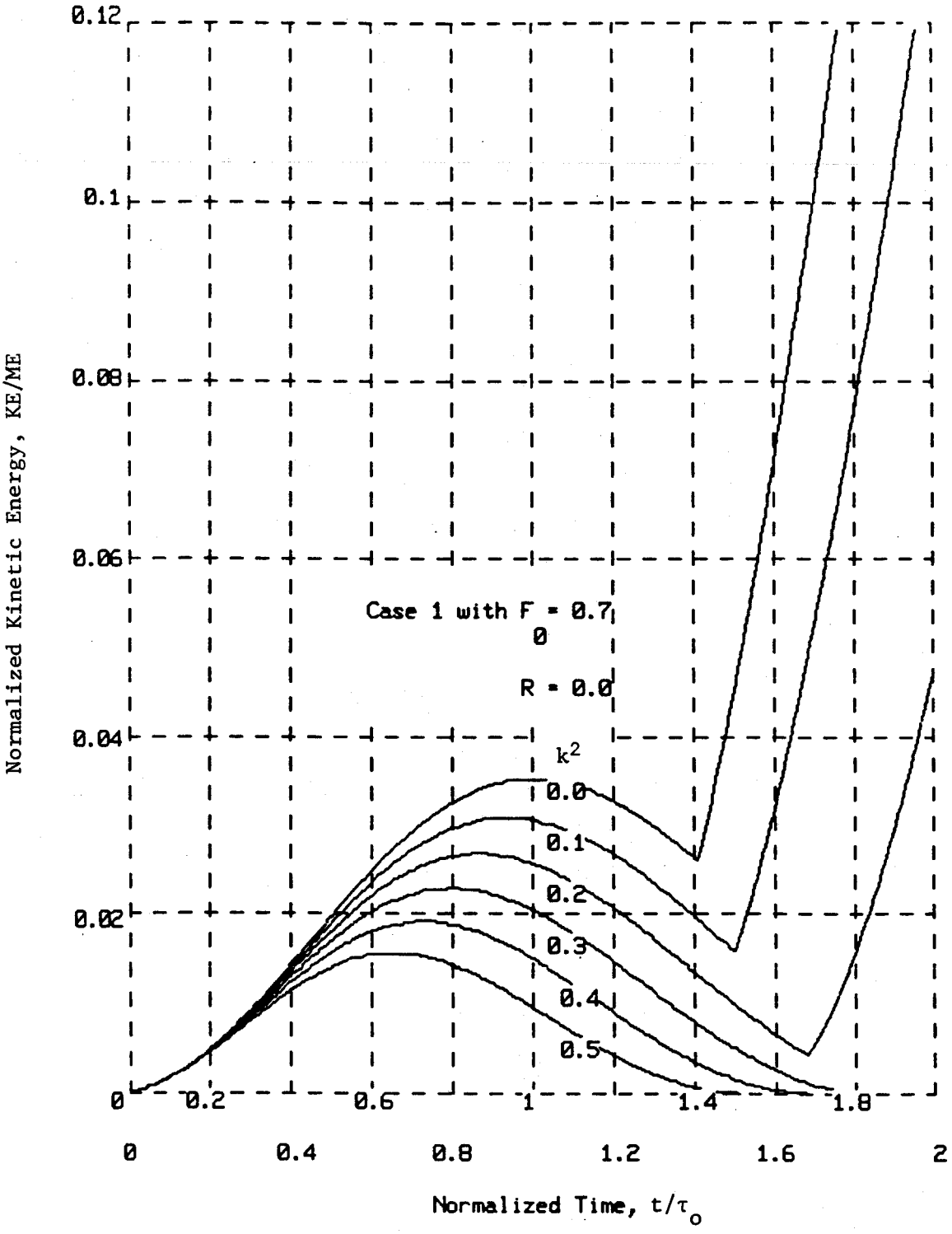

Figure 3.17 – Normalized Kinetic Energy vs Time for $F_0 = 0.7$, $R_0 = 0$ and Selected Values of Coupling Coefficient, k^2.

process returns to zero kinetic energy for $k^2 > 0.3$. Lower values of k^2 represent a condition where the secondary is unable to absorb sufficient energy for this level of F_o before the ultimate strain is reached and the winding ruptures.

This example, though simple, illustrates the potential advantage of using inductive coupling to restrain magnetic to kinetic energy conversion because it can be effective on a fast enough time scale with reasonable levels for coupling coefficients. Next year this will be developed further, in conjunction with the multiple circuit TF coil system characteristics described in Section 4.0.

4.0 DISCHARGE CHARACTERISTICS FOR MULTIPLE CIRCUIT TF COIL SYSTEMS

R.J. Thome, J.M. Tarrh, R.D. Pillsbury, Jr., W.R. Mann and W.G. Langton

4.1 Summary

The previous section closed with a simple model to illustrate the ability of a secondary circuit to be effective in restraining magnetic to kinetic energy conversion in the event of a structural failure in a primary circuit. In this section, the use of multiple circuits in a TF coil system will be studied since it presents a means for limiting the magnetic to thermal energy conversion in the winding, in the event of a quench.

Specific examples of this type have been considered by Yeh[1] and Green and Kazimi.[2] This section will discuss the general character of the process and the effect of the number of circuits on the voltage required for discharge of the first and the remaining circuits. This will be related to the allowable temperature rise, stored energy, operating current level, and current density in the windings.

Typically, results show that only a small fraction of the total energy needs to be removed if only one of k circuits is discharged because the bulk of the energy is retained by the (k-1) circuits which maintain constant flux throughout the transient. This procedure allows the first circuit to be discharged more rapidly for a given initial voltage and final temperature limit, thus allowing for a longer delay time before the dump is initiated or for operation at a higher current density. The remaining coils could then be discharged on a longer time scale. However, if the remaining circuits require rapid discharge shortly after the first, then the necessary voltage per coil may or may not be higher than for the first

circuit depending on the discharge sequence, number of coils and aspect ratio. The voltage to ground can be considerably lower than if a single system circuit were used. The general criteria governing the different reactions will be developed further next year.

The next section describes the model, which was the basis for a code developed in part under this program. The last section gives the result for a case based on a recent version of TFCX to illustrate its application.

4.2 Model Description

Figure 4.1 shows a plan view of 2N toroidal field coils. The total energy stored is independent of the circuitry and is given by the following (assuming all coils to be initially charged to the same current, i_o).

$$E = i_o^2 \left[NM'_{11} + \sum_{m=1}^{(2N-1)} \sum_{n=m+1}^{2N} M'_{mn} \right] \qquad (4.1)$$

where

$2N$ = total number of coils

i_o = current per coil

M'_{mn} = mutual inductance between coils m and n

If these coils are connected such that there are a total of k circuits then there are 2N/k coils per circuit.* Assume that the sequential coils in

* Where 2N/k is an integer, that is, there are an equal number of coils in each circuit.

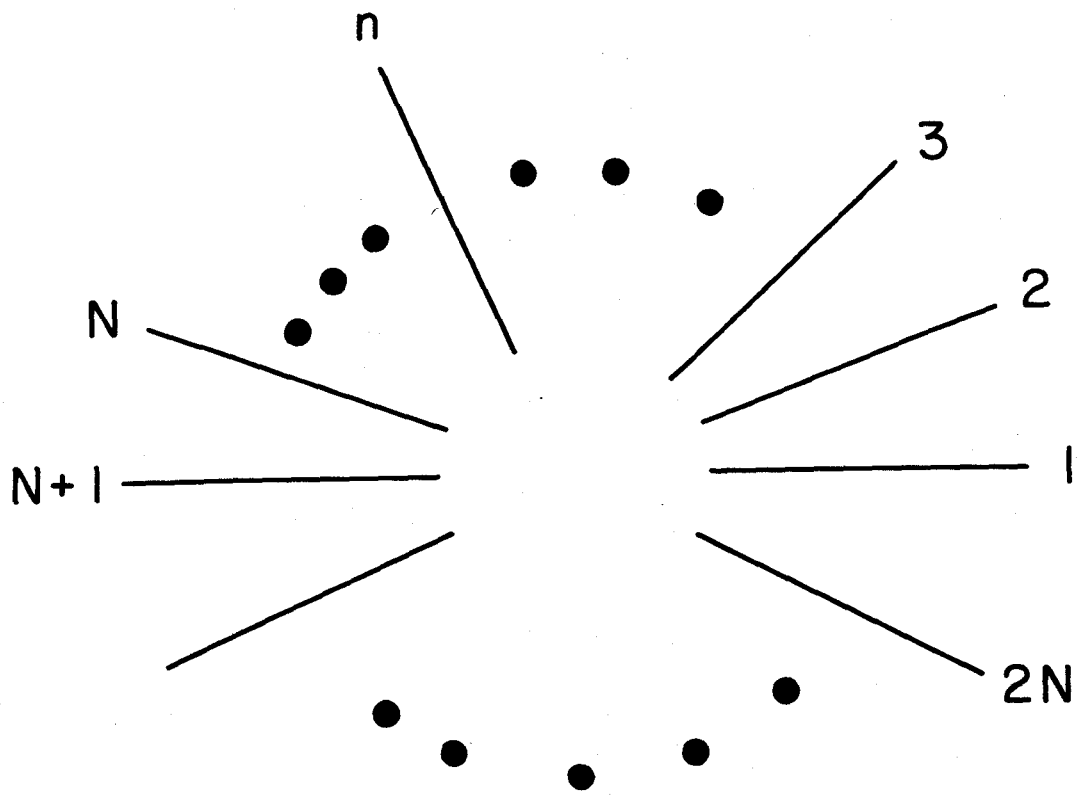

Figure 4.1 Plan view of midplanes of 2N TF coils.

Fig. 4.1 are in alternating circuits; that is, the mth circuit contains coil numbers m, m+k, m+2k, .., m+(2N-k) where m = 1, 2, .., k. The inductance between circuits m and m' (note: m = m' implies self inductance) is then given by

$$M_{mm'} = \sum_{j=0}^{(\frac{2N}{k} - 1)} \sum_{\ell=0}^{(\frac{2N}{k} - 1)} M'_{m+\ell k,\, m' + jk} \qquad (4.2)$$

Initially, each circuit links the same total flux given by:

$$\lambda_o = \lambda_m = \sum_{j=1}^{k} M_{1j}\, i_o;\ m=1, 2, .., k. \qquad (4.3)$$

If one circuit is discharged completely while the others maintain constant flux, then the final flux linked by circuit m is λ_{mf} given by:

$$\lambda_o = \lambda_{mf} = \sum_{j=2}^{k} M_{mj}\, i_{jf};\ m=2, 3, .., k. \qquad (4.4)$$

where i_{jf} = final current in circuit j

and it is assumed, without loss of generality, that circuit 1 is the first to be discharged. Since λ_o can be found from (4.3), then (4.4) represents a set of equaitons which can be solved for the unknown currents, i_{jf}.

The code developed to address this problem has been written for $k \leq 9$ and has been used for the sample case in Section 4.3. Many of the

advantages of the multiple circuit approach, however, occur for k=2 or 3 and k will probably be limited to a small number for practical circuit design and operation. The following, therefore, summarizes the final currents for k up to four circuits in terms of the coupling coefficient $k_{ij} = M_{ij}/M_{ii}$ (note that $M_{ii} = M_{jj}$ and $M_{ij} = M_{ji}$ for these systems).

Case A: $k = 2$

$$i_f = 0$$

$$i_{2f}/i_o = 1 + k_{12} \tag{4.5}$$

Case B: $k = 3$

$$i_{1f} = 0$$

$$i_{2f}/i_o = i_{3f}/i_o = \frac{1+2k_{12}}{1+k_{12}} \tag{4.6}$$

Case C: $k = 4$

$$i_{1f} = 0$$

$$i_{2f}/i_o = i_{4f}/i_o = \frac{(1+2k_{12} + k_{13})\,(1-k_{12})}{(1+k_{13}) - 2k_{12}^2} \tag{4.7}$$

$$i_{3f}/i_o = (i_{2f}/i_o)\,\frac{(1+k_{13} - k_{12})}{(1 - k_{12})} \tag{4.8}$$

In general, the final energy stored in the system is given by

$$E_f = \frac{M_{11}}{2} \sum_{j=2}^{k} i_{jf}^2 + \sum_{j=2}^{k-1} \sum_{j'=j+1}^{k} M_{jj'}\, i_{jf}\, i_{j'f} \tag{4.9}$$

and the final flux linked by the first circuit is

$$\lambda_{1f} = \sum_{j=2}^{k} M_{1j}\, i_{jf} \tag{4.10}$$

If we assume that all circuits are charged and at a current i_o for $t<t_d$ and that a transient is initiated at $t=t_d$ by inserting a resistance R_1 in the first circuit while all others have zero resistances, then the first circuit will decay with an exponential time constant, τ. All other circuits will approach their final current levels i_{mf} with the same time constant. This condition is expressed by the following for $t>t_d$.

$$i_1 = i_o\, e^{-(t-t_d)/\tau} \tag{4.11}$$

$$i_m = i_{mf} - (i_{mf}-i_o)\, e^{-(t-t_d)/\tau} \quad ;m\neq 1 \tag{4.12}$$

The inductance voltage across the terminals of Circuit 1 is given by

$$V_1 = \frac{d\lambda_1}{dt} = \frac{d}{dt}\left(\sum_{m=1}^{k} M_{1m} i_m\right) \tag{4.13}$$

Equations (4.11) to (4.13) may now be combined to show that

$$V_1 = \frac{2E}{i_o\tau}\left(\frac{M_{11}}{M_o}\right)\left[-1 + \sum_{m=2}^{k} \frac{M_{1m}}{M_{11}}\,(i_{mf}/i_o - 1)\right] e^{-(t-t_d)/\tau} \tag{4.14}$$

where:

M_o = circuit inductance if k=1

M_{11} = inductance of first circuit if k≠1.

$E = M_o i_o^2/2$

The maximum value of V_1 occurs at $t=t_d$ and (4.14) shows that for a given stored energy, initial current and discharge time constant, V_1 is always less for a multiple circuit system because:

(a) $M_{11} < M_o$ as indicated by (4.2)

(b) the absolute value of the term in brackets is reduced for k>1 because $M_{1m} < M_{11}$ for circuits of this type where $M_{11} = M_{mm}$ and because $i_{mf}/i_o > 1$ for $m \neq 1$

It is useful to define a characteristic voltage, V_c, as the maximum voltage which would be required to discharge the system if there were only one circuit, that is

$$V_c = \frac{2E}{i_o \tau} \tag{4.16}$$

Equation (4.14) and (4.16) can be combined to form the normalized maximum voltage for the first of k circuits to be discharged.

$$V_{1max} = \frac{V_{1max}}{V_c} = \left(\frac{M_{11}}{M_o}\right)\left[-1 + \sum_{m=2}^{k} \frac{M_{1m}}{M_{11}} \left(\frac{i_{mf}}{i_o} - 1\right)\right] \tag{4.17}$$

Equation (4.17) implies that V_{1max} is primarily a function of k and the overall geometrical characteristics of the coils which comprise the TF coil system. The effect of k is to strongly reduce V_{1max} with the most significant reduction occurring when k increases from one to two or three. Equation (4.5) can be used with (4.17) to illustrate the effect for k=2, with the result that:

$$V_{1max}\Big|_{k=2} = -(1/2)(1-k_{12}) \tag{4.18}$$

Since $k_{12} < 1$, (4.18) shows that the maximum voltage required to discharge the first of two circuits is less than one half that required to discharge

the system if it were connected in a single circuit. This arises primaryly because less than half the energy must be removed. The quantity V_{max} can be interpreted as the voltage to ground required in each case. The maximum voltage required to discharge the second circuit with the same time constant as that used for the first circuit is given by

$$V_{2max}\Big|_{k=2} = -\frac{2E_f}{i_{2f}\tau} \tag{4.19}$$

Equation (4.19) can be normalized to the characteristic voltage (4.16) and shown to be

$$V_{2max}\Big|_{k=2} = -1/2;\ \tau_1 = \tau_2 = \tau \tag{4.20}$$

Thus, the maximum voltage required to discharge the second circuit in a two circuit system is only half that required to discharge a one circuit system with the same time constant. Note that the voltage per coil would be the same in both situations, but that the maximum voltage to ground is reduced by a factor of two for the two circuit system relative to the single circuit system. However, because the second circuit is starting its transient from a higher current level, its discharge time constant should be shorter than τ if it is to be protected to the same temperature limit. This will be discussed further later in this section. The results for the maximum voltage for the second circuit in a two circuit system are

$$\frac{V_{2max}}{V_c} = \frac{(1 + k_{12})}{2};\ T_1 = T_2 = T_f \tag{4.21}$$

The main advantage of using the multiple circuit approach is the substantial reduction in the circuit voltage to ground which then reduces the risk of a ground fault. The main disadvantage with the system as described thus far is additional circuit complexity. Specifically, if either the time constant or temperature limit for discharge of the first and second circuits is to be the same then the resistor to be inserted in the second circuit, R_2 is not the same as that required for the first circuit, R_1, that is

$$R_1 = \frac{R_o}{2}(1-k_{12}) \tag{4.22}$$

$$R_2 = \frac{R_o}{2(1+k_{12})} \quad \text{if } \tau_1 = \tau_2 = \tau$$

or

$$R_2 = \frac{R_o(1+k_{12})}{2} \quad \text{if } T_1 = T_2 = T_f \tag{4.23}$$

where $R_o = M_o/\tau$ = resistor required if a single circuit system is used.

The selection of the required discharge time constant, τ, is dependent on the cause for discharge. In a superconducting magnet system, if a normal region forms and begins to propagate (i.e. - "quench"), a rapid discharge is usually initiated in order to limit the ohmic heating and corresponding temperature rise in the normal zone. Assume that the normal zone forms at t=0 with an instantaneous local transfer of current from the superconductor to its copper stabilizer which then has a current density j_{cu}. If the heating is adiabatic, then the local temperature rise is governed by the following

$$j_{cu}^2\, dt = \frac{1}{\rho_{cu} A_{cu}} (\Sigma_m\, \gamma_m\, C_m\, A_m)\, dT \tag{4.24}$$

where

ρ_{cu} = resistivity of copper = ρ_{cu} (T)

A_{cu} = copper cross-sectional area in conductor

A_m = cross-sectional area of material m which is capable of local heat absorption but is not a current carrier for t > 0 except when m = cu

C_m = specific heat of material m = C_m (T)

γ_m = density of material m

T = temperature

The left side of (4.24) can be integrated if a current transient is defined for all time and the right side can be integrated based on an initial temperature and material properties as a function of temperature after the geometric ratios A_m/A_{cu} are defined. For a specific conductor, the latter are known and the right side of (4.24) becomes a function of the final temperature only, that is, $G(T_f)$. To evaluate the left side of (4.24), assume the transient shown in Fig. 4.2 which assumes quench initiation at t=0 followed by a delay time, t_d, during which the current is held constant. A discharge of the circuit then occurs with a time constant, τ_d. Equation (4.24) can then be integrated to yield:

$$j_o^2(t_d + \frac{\tau_d}{2}) = G(T_f) \qquad (4.25)$$

where

j_o = initial current density in cu

If we further assume that the resistance of the normal region is small relative to the resistor inserted in the circuit at $t=t_d$ then τ_d in (4.25) can be set equal to the τ required earlier in this section with the result that

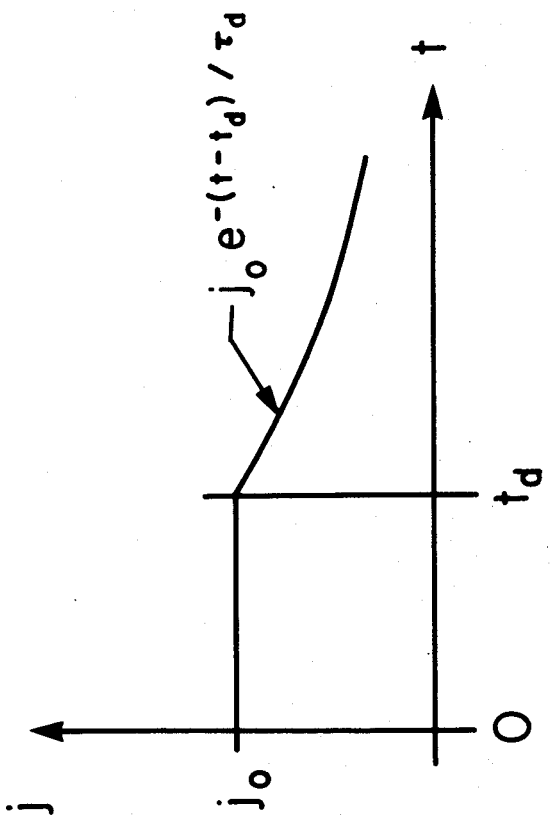

Figure 4.2 Illustration of conductor current density as function of time

$$\tau = 2\left[\frac{G(T_f)}{j_o^2} - t_d\right] \tag{4.26}$$

For a given conductor, final temperature and delay time (4.26) allows τ to be found for use in the voltage expressions derived earlier.

The concepts which have been developed are applied in the next section to a specific case to illustrate some of the effects of the multiple circuit approach. A substantial decrease of the voltage required for discharge of the first circuit relative to that required for a single circuit discharge can be achieved, with the main incremental benefit occurring for k=2 and 3. This can be done at the cost of increased circuit complexity because sequentially-discharged circuits require different dump resistor values if the discharge time constants are to be the same or, more realistically, if the same adiabatic temperature limit is applied for protection purposes. This trade-off problem will be considered further next year to develop general criteria for selection of circuit configurations.

4.3 Discharge Characteristics for TFCX TF Coils

The concepts discussed in the previous section have been incorporated in a code which was developed to study the discharge characteristics of a TF coil system from the coil protection standpoint. Cases for TFCX were considered where the entire coil set is discharged or where the coil set is divided into a number of circuits and only one of the circuits is discharged. In order to maintain a zero net out-of-plane force on any given coil, two circuits must be used with alternate coils in each circuit, such that the discharge of the first circuit still results in a TF distribution which is periodic about the machine axis. Using more than two circuits has other advantages but does not result in zero net out-of-plane forces. The

code was applied to a 10 T TFCX scale system with 12 or 16 coils to illustrate some of the features of this approach when discharge circuits of this type are used. The advantages, disadvantages, and system implications of using multiple circuits is still under evaluation.

An elevation view of the TF coil outline used in this study is shown in Fig. 4.3. It is the result of an early study and is somewhat larger than more recent design points. The ampere turns per coil and cross-section in the upper left of the figure correspond to a 16 coil configuration. The portion of this study based on a 12 coil set used the same TF coil outline in the rz plane, but with the ampere turns per coil increased by the ratio of 16/12.

The calculation of discharge characteristics requires circuit self and mutual inductances. These were obtained by computing the self and mutual inductances for and between individual coils in the complete set, then collapsing the inductance matrix according to the number of circuits. It was assumed that the coils were connected with each successive coil distributed sequentially among k circuits. Sixteen coils may, therefore, be connected in one circuit or with sequential coils in two, four or eight circuits with eight, four or two coils per circuit, respectively. Twelve coils on the other hand, may be connected in one circuit or with sequential coils in two, three, four or six circuits with six, four, three or two coils per circuits respectively.

Table 4.1 gives some of the characteristics if the system is charged to the operating level and one circuit is then discharged while the remaining (k-1) circuits maintain constant flux; that is, they are not discharged and remain superconducting. The first line gives the percent energy which

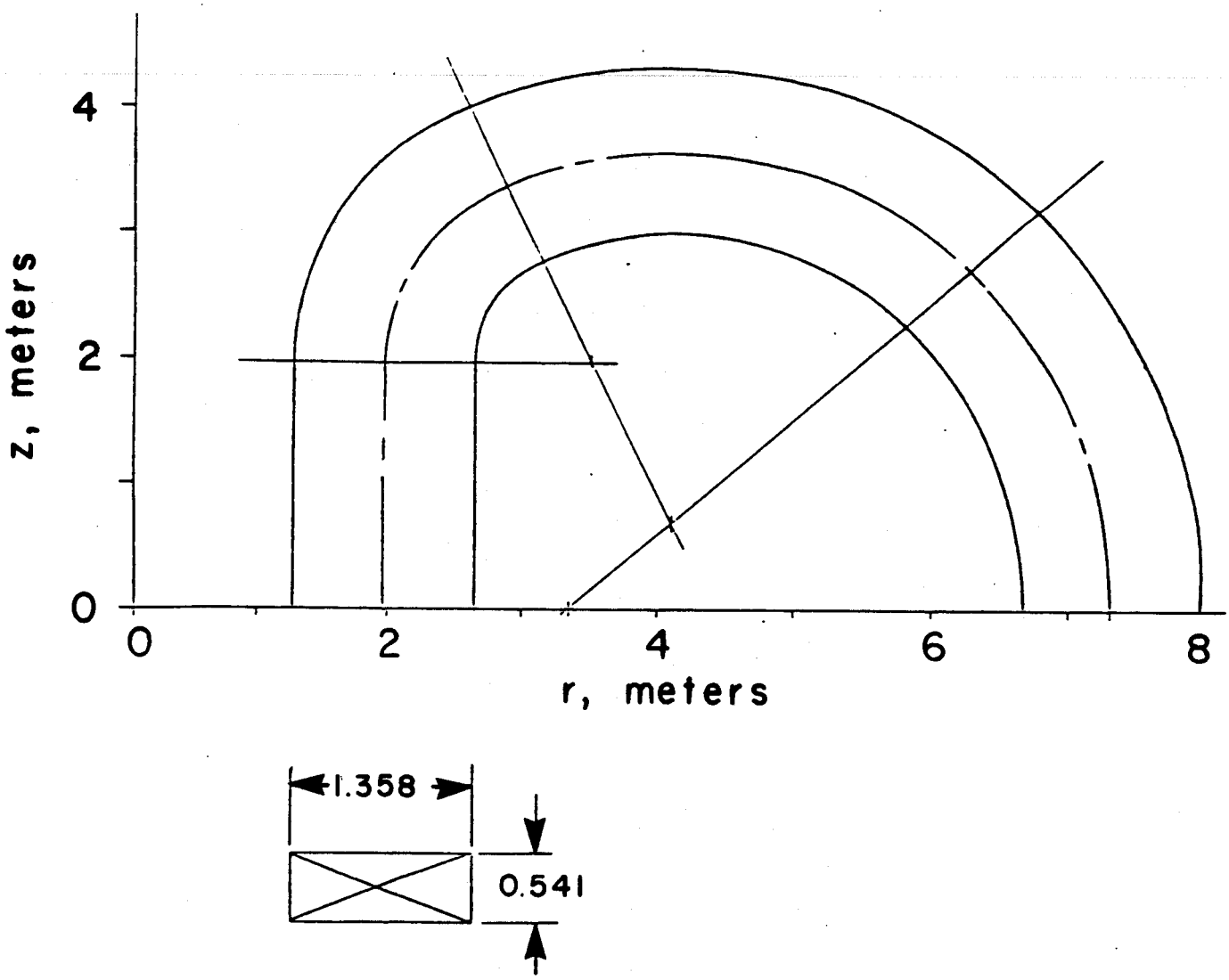

Figure 4.3 Typical TF Coil dimensions for TFCX.

TABLE 4.1
CHARACTERISTICS FOR DISCHARGE OF THE FIRST OF k CIRCUITS [a]

		Number of Coils	Number of Circuits, k					
			1	2	3	4	6	8
(1)	% Energy Removed or V_{max}/V_{maxi}	12	100	19.9	12.9	9.6	6.4	-
		16	100	13.1	-	6.4	-	3.4
(2)	B_f/B_i [c]	12	0	0.80	0.87	0.90	0.94	-
		16	0	0.87	-	0.94	-	0.97
(3)	I_f/I_i [d]	12	-	1.6	1.3	1.29	1.28	-
		16	-	1.74	-	1.36	-	1.35
(4)	$V_{max}\ \tau$ [10^5 V-sec]b	12	25.6	5.07	3.33	2.43	1.67	-
		16	24.5	3.19	-	1.60	-	0.83

[a] Coil Geometry as in Figure 4.3

[b] $E = 1.45 \times 10^{10}$ J for B = 10 T

[c] $\frac{\text{B Final}}{\text{B Initial}}$

[d] $\frac{\text{I Final (Adj. Circuit)}}{\text{I Initial}}$

must be removed from the system if one circuit is discharged as a function of the number of circuits, k. For one circuit, 100% of the energy must be removed in the event a fast discharge is required. If there are two circuits in a twelve coil system then about 20% of the total stored energy must be removed in discharging one circuit and the fraction drops to 13% in discharging one out of three circuits, 9.6% for one out of four circuits and 6.4% for one out of six circuits. The corresponding fractions are somewhat smaller for the 16 coil system because a smaller fraction of the total system is de-energized when discharging one circuit.

When one of the k circuits is discharged while (k-1) maintain constant flux, the currents in the circuits which remain "on" are altered somewhat from the initial condition. The second line gives the ratio of the final average toroidal field to the initial field level as a function of the number of circuits. The table indicates that 80% or more of the initial field level is maintained for the twelve coil system with two or more circuits when one is discharged and that 87% or more is maintained for the sixteen coil set.

All of the circuits which remain "on" do not necessarily have the same final current, because of differences in coupling between circuits. The ratio of final to initial current in the circuit adjacent to the one which is discharged is shown in line three. The increase is most dramatic for two circuits, where the ratio is 1.6 and 1.74 for 12 and 16 coil systems, respectively. For more circuits, the ratios are about 1.3 to 1.35. This current increase, coupled with the high field level which is retained as indicated in line two, illustrates the potential for forcing the coils to go normal in those circuits adjacent to the one being discharged. An

evaluation is required to determine whether or not this ability to initiate normal regions and distribute the energy dissipation more uniformly throughout the system is favorable under selected fault conditions. Alternatively, lines two and three may be used to determine the over-current capability required for the conductor if it is to be designed to remain superconducting in the circuits which are not discharged. Since conductors are often designed at about 70% of critical current, the table implies that k=2 would force circuit two to go normal, but k>3 could allow circuits 2 and 3 to remain superconducting if designed for this condition.

In a system with a given operating current and initial energy, line 1, the percent energy removed, is also the ratio of the maximum voltage which must be applied to the first circuit being discharged to the maximum voltage which must be applied if all coils are in one circuit. This illustrates one of the potential advantages of the multiple circuit system. For example, for two circuits, the maximum voltage which must be applied to discharge one of them to zero current is only 19.9% of the maximum voltage required to discharge all coils to zero current if they are all in only one circuit. This occurs because most of the energy is retained in the system by the coils which stay "on" and maintain constant flux. If, however, the remaining circuits subsequently require discharge with the same time constant or with a faster time constant to satisfy a specified adiabatic temperature rise limitation, then they might require a higher voltage per coil than applied to the first. The trade-off between the advantage of using a low voltage on the first circuit versus the likeihood of needing a subsequent rapid discharge of the remaining circuits is still under evaluation. Note that if there are three or more circuits, then the ratio of final to initial current in the circuit adjacent to

the discharged circuit is in the range of 1.3 to 1.35 (line 3). Since this is in the range of the ratio of critical current in operating current typically selected for TF conductors, the remaining charged circuits may be designed to remain superconducting thus allowing the bulk of the TF system energy to be maintained or removed over a longer period of time.

The last line in Table 4.1 applies for a total system stored energy of 1.39×10^{10} J and corresponds to a maximum field at the winding of 10 T. It gives the product of maximum discharge voltage and discharge time constant for this system for the first circuit to be discharged as a function of the number of circuits. The discharge time constant, τ, is usually specified on the basis of a protection criterion for allowable conductor temperature rise in the event of a normal front propagation. Since the time constant is the same for all cases in the table this indicates the potential advantage for the first discharge of using multiple circuits.

The use of multiple TF coil circuits has the potential for rapid discharge of a section of the TF system while maintaining some degree of out-of-plane force symmetry and allowing the bulk of the energy and field level to be decreased on a longer time scale. The system implications and impact of subsequent rapid discharge requirements on the remaining circuits is still under evaluation, but can be expected to be more advantageous as the scale of a system increases or as the current density increases.

References

1. H.T. Yeh, "Considerations of Coil Protection and Electrical Connection Schemes in Large Superconducting Toroidal Magnet Systems", ORNL/TM-5043, March 1976.

2. R.W. Green and M.S. Kazimi, "Aspects of Tokamak Toroidal Magnet Protection ", PFC/TR-79-6, July 1979.

5.0 SAFETY RELATED EXPERIMENTS

5.1 Arc Extinction Voltages Between Helium-Filled Electrodes at 300 K and 4.2 K - J. Borzikowski, T. Ishigohka, and Y. Iwasa

5.1.1 Introduction

A series of experiments to determine the arc extinction voltage was conducted in both room temperature gaseous helium and liquid helium environments.

The experimental concept was to initiate an arc within a helium-filled electrode gap by using an exploding wire technique. A DC current flowing through the resistive circuit was made to pass through a thin wire fuse, by manually opening a knife switch. The fuse would then heat rapidly and burn out, producing a partially ionized, high-density plasma in the gap. If the voltage across the electrodes was high, and the degree of ionization in the gap was sufficient, an arc would be sustained. Since we were interested only in whether or not an arc would be extinguished under specific initial conditions, no attempt to study steady-state arcing was made.

5.1.2 Experimental Apparatus and Procedures

Circuit Layout

Figure 5.1 shows the basic circuit used for all the tests. A 125 A, 40 V DC power was used in its constant voltage mode. The use of this "constant" supply rather than a capacitor bank as the source of electric current for the circuit is the major change from the circuit used in our previous measurements.[1] The major difficulty with the capacitor bank is that both supply voltage and current decrease rapidly during the critical moments of arc formation and extinction, and it was not absolutely clear if arc extinction occurred because of insufficient electrode voltage or because of insufficient arc current.

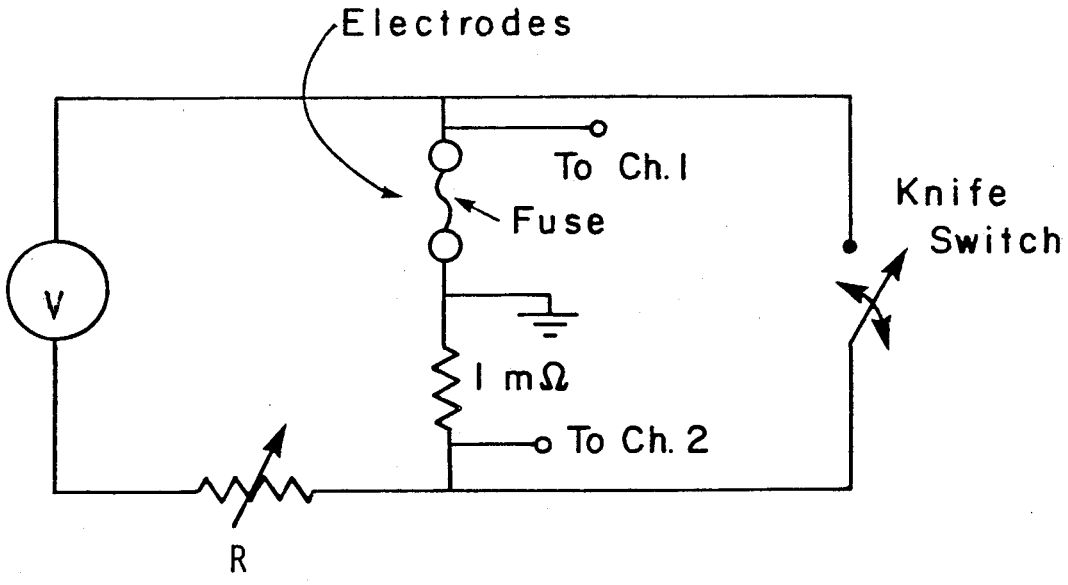

Fig.5.1 Circuit used for the measurements.

The load resistor, R, was made by soldering three, 1.8-m lengths of 304 stainless steel tubing each having a 0.25-mm wall thickness, using copper plumbing elbows. The negative end of this resistor served as a fixed terminal, while the other terminal was adjustable. The adjustable terminal consisted of a strip of braided copper wire, anchored by a steel hose clamp and attached to the positive lead by a spring clamp. The load, resistance variable in discrete steps, had a range of approximately 0.7 Ω. A given supply voltage, at fixed R, determined the initial current.

A 1-mΩ shunt resistor, placed in series with the electrode assembly, measured the electrode current. A manual single-throw knife switch was used to direct current flow to the electrode assembly.

A four-channel transient digital recorder monitored both the electrode current and voltage as a function of time. A digital volt meter (DVM), connected across the load resistor, measured V_R - an initial condition parameter used to compare data from different events. By later calibration, V_R could, given the actual value of R, be converted to initial circuit current.

As an additional diagnostic, an acoustic emissions (AE) sensor was installed on the electrode assembly. It was found that, since an arc generates strong AE signals, these sensors could confirm the presence of an arc. AE signal bursts typically describe a wave envelope which, in this application, lasted approximately 10 ms. For this reason their use in short arc events ($\lesssim$5 ms) was of limited value since the modulating envelope would mask any activity due to arcing.

Electrode Assembly and Fuse

As mentioned previously, the electrode assembly used in the room temperature gaseous helium environment is different from that used in the liquid helium environment, the one for LHe use being smaller than the room temperature assembly, in order to minimize liquid helium consumption.

Both assemblies consist of two electrically-insulated copper plates (the anode and cathode) separated by a fixed distance -- the electrode gap. A screw mounted in the probe secures the filament assembly (fuse) between the anode and cathode plates.

The fuse consists of an insulating square (1 cm) with a hole or slot machined at the center to accommodate a thin metal wire filament. The wire is threaded through the insulator, folded in step fashion, and then sandwiched between two copper squares. The fuse assembly is illustrated schematically in Fig. 5.2. This assembly is then secured between the anode and cathode plates by a screw mounted centrally through the anode.

Procedures

A. Room Temperature

1. Thread filament through and fold across insulator.
2. Slide copper plates across top and bottom of insulator keeping filament immobile.
3. Mount and secure fuse assembly in electrode assembly, using anode screw.
4. Replace bell bar cover and begin pumping, filling channel with helium.
5. Zero all transient digitizer signals and recheck settings.
6. Turn on supply current and monitor V_R.

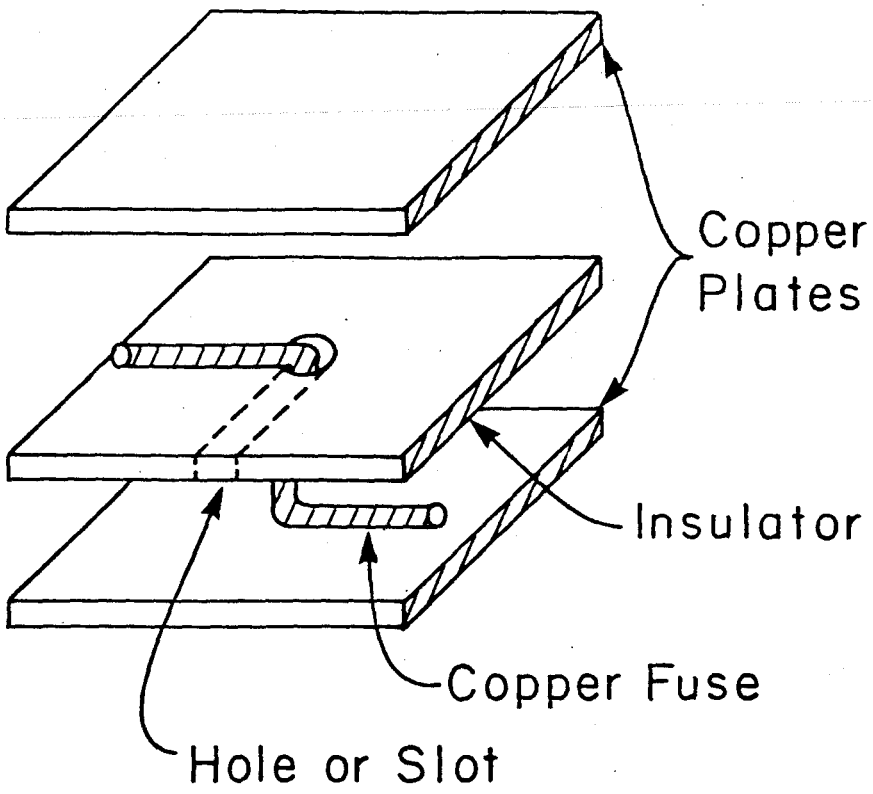

Fig.5.2 Fuse assembly schematic.

7. Adjust V_R to desired level.

8. When stabilized reading of V_R is obtained, shut off He line.

9. Open switch in a smooth, rapid motion, repeated from shot to shot.

10. Shut off current supply to prevent extending arcing or accidental shorting.

11. When voltage dies off, close knife switch.

12. Remove bell jar setting.

13. Lossen mount screw and remove filament assembly.

B. Liquid Helium (4.2 K)

1. Filament assembly as in above procedure.

2. Precool electrode assembly in liquid nitrogen bath.

3. Place electrode assembly in helium Dewar, and transfer liquid helium until the liquid level is above the electrode assembly.

4. Connect voltage leads and power lines.,

5. Follow steps 3-11 above.

6. Disconnect all leads.

7. Withdraw rod assembly from Dewar.

8. Warm electrical assembly using heat gun.

9. Loosen and remove fuse assembly.

5.1.3 Results

The effects of a number of parameters on the arc extinction voltages V_χ, obtained in an arc event lasting more than 5 ms have been investigated. V_χ is defined as the peak value of voltage at the instant of fuse burnout: if the

voltage across the electrodes exceeds V_χ, an arc is initiated at the instant of fuse burnout and the current across the elecrtrodes is sustained; if it is below V_χ, the current drops to zero.

The variable parameters are: (1) helium temperature; (2) insulator material and/or insulator configuration; (3) fuse material; (4) gap size; (5) current. A summary of data is presented in Table 5.1.

5.1.4 Discussion and Conclusions

As expected, increasing the gap size increases V_χ. A variety of theoretical models exist to correlate these parameters but most are expressed in terms of a "steady-state" arc voltage which is not directly applicable to these trials. A greater variety of gaps would have to be tested in order to better explain the relationship between V_χ and gap size.

The slightly lower voltages seen when using the tinned electrodes might be explained by the lower work functions of tin (7.4 V) and lead (7.4 V) compared with that of copper (7.7 V). For the same degree of electrode heating, surface ionization at a given current occurs more easily with tin and lead than with copper, resulting in lower plasma resistivity and thus a lower voltage at a given current.

In the case of the solder fuse, it seems that its higher resistivity and lower heat capacity in the solid state cause very rapid burnout. This reduces the amount of heating available to vaporize the metal and ionize the gas by thermionic emissions. The radiation loss associated with the reduced pool of highly energetic particles varies as Z^2, Z being the atomic number, which for tin ($Z = 50$) and lead ($Z = 82$) greatly exceeds that of copper

Table 5.1: Summary of Data

He	Insulator	Fuse	Gap (mm)	I(A)	V_x(V)	t_{arc}(ms)
300 K	G-10, hole	Cu	1.1	134	21	>30
"	"	"	"	120	20	>25
"	"	"	"	120	19	15
"	"	"	"	116	21	25
"	"	"	"	84	19	>35
"	"	"	"	68	19	11
"	G-10, slot	"	"	120	18	33
4.2 K	G-10, slot	Cu	1.1	170	21	<5
"	"	"		150	19	<5
"	"	"	"	150	19	<5
"	"	"	"	110	17	<5
"	"	"	"	78	16	35
"	"	"	"	76	17	<5
300 K	G-10, hole	Cu	1.9	180	27	>30
"	"	"	"	160	26	23
"	"	"	"	118	22	>25
"	"	"	"	112	23	>40
"	"	"	"	94	25	34
300 K	G-10, hole	solder	1.3	140	27	--
"	"	"	"	130	25	"
"	"	"	"	126	27	"
"	"	"	"	120	23	"
"	"	"	"	112	30	"
"	"	"	"	80	20	"
300 K	G-10, hole	solder	2.1	154	33	"
"	"	"	"	154	35	"

($Z = 29$, possibly poisoning the plasma with impurities.

The arc extinction voltage is virtually independent of helium temperature, agreeing with a conclusion of the previous measurement.[1] The most important finding of this series of measurments has been the absence of arcing following the burnout of a solder fuse, suggesting that, if present in the magnet winding and causing shorts, solder chips would be less troublesome than copper chips.

REFERENCES

1. O. Tsukamoto and Y. Iwasa, "Arc Extinction Voltage Between Copper Electrodes in Liquid Helium - Application to the High-Voltage Discharge of Superconducting Magnets", Proc., 9th Intl. Cryogenic Engr. Conf. (Butterworths, Surrey, UK), 497 (1982).

5.2 Small Football Coil Test - A.M. Dawson

The small football test coil described in detail in Section 5.2.2 below was completed in August 1983 and was instrumented prior to initial testing in the Plasma Fusion Center Component Test Facility in September 1983. A second small coil is being wound and will also be tested during FY84. Differences in the coil designs will be outlined below.

Tests that will be performed on these coils are designed first to determine fundamentals of conductor behavior and then to determine coil characteristics. These tests will include:

- strain effects on conductor characteristics including measurements of stability and critical current degradation with increased strain
- cyclic fatigue measurements which will simulate operation of the proposed Alcator DCT experiment. Deflections to be incurred by the coil sides during these tests are planned to be greater than those that the machine will experience. The deflection size will be increased until the following events are experienced:
  - (a) degradation of conductor performance and/or
  - (b) sheath failure and/or
  - (c) thermal burnout and/or
  - (d) internal over pressure during quench
- motion of conductors

5.2.1 Conductor Description

The small football test coil is wound from a sheath-enclosed cable of 27-strand, bronze matrix process Nb_3Sn copper stabilized conductor. Figure 5.3 is a photograph of a cross section through the conductor. Table 5.2 lists conductor parameters for this coil, while Table 5.3 lists conductor parameters for the proposed Alcator DCT machine. For both

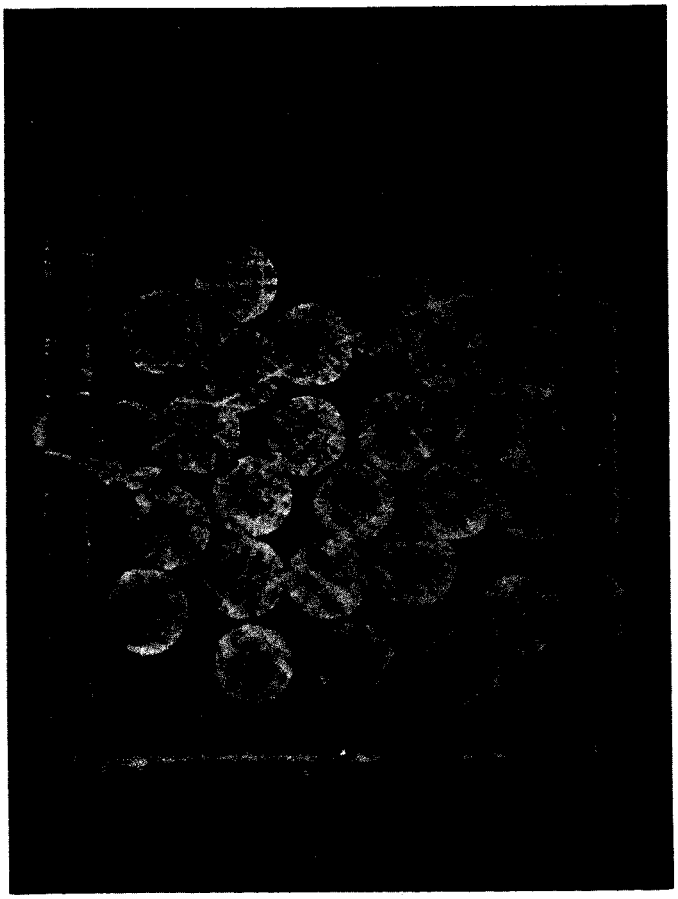

Figure 5.3 Cross section of conductor used in small football test.

TABLE 5.2
SMALL FOOTBALL COIL CONDUCTOR PARAMETERS

Material	Nb_3Sn, copper stabilized
Cu: Noncopper ratio	1.8
Void fraction	32%
Sheath	JBK - 75
Sheath wall thickness	0.015 in. (0.38 mm)
Sheath dimensions	0.192 " x 0.192" sq. (4.88 mm sq)
Short sample I_c, A	
10 T	1890
12 T	1140
Short sample J_c, A/mm^2 @ 1.5 μV/cm	
10 T	509
12 T	307
Strands	27
Strand diameter	0.7 mm

TABLE 5.3
ALCATOR DCT TF CONDUCTOR PARAMETERS

Material	Nb_3Sn, copper stabilized
Cu: Noncopper ratio	1.8
Void fraction	32 %
Sheath material	JBK - 75
Sheath wall thickness	1.73 mm
Sheath dimensions	2.1 x 2.1 cm
I_c, A (10 T)	40 kA
I_{op}, A (10 T)	23 kA
Copper area	1.19 cm^2
Strands	486
Strand diameter	0.7 mm

the test coil and the proposed Alcator DCT toroidal field coil conductor activation is 2-phase with a first phase of 4 days duration at 700 C and a second phase of 2 days duration at 730 C. This activation sequence was chosen based on work by Hong[1] which indicates that this dual reaction cycle achieves optimal current densities.

The Alcator DCT conductor, described in Table 5.3, is based on the conductor configuration for the Westinghouse LCP coil. Use of the small-scale conductor in a simple test coil configuration with unsupported sides provides an opportunity to perform long term cyclic tests and fatigue tests that can be extrapolated to predict Alcator DCT behavior. Such small-scale tests are flexible and comparatively inexpensive compared with full scale tests.

5.2.2 Small Football Test Coil Description

The coil is wound in bifilar fashion as indicated in Fig. 5.4, on a 304 stainless-steel mandrel. The conductor is laid into grooves machined into the mandrel. A total of 118 cm of conductor was used in total. The central coil region incorporating 75 cm of conductor is located in the high field region of the 6B, Bitter solenoid during experiments on the coil. The three coil turns are clamped in place by stainless-steel plates ~ 6 cm in width as shown in Fig. 5.5. The overall mandrel length from the hydraulic inlet/outlet tee joints to the base is ~ 45 cm.

The coil has been instrumented with three pairs of voltage taps. One pair is across the current leads, one pair is separated by 2.4 cm across a central turn, and the third pair is located across a sharp radius of the coil to monitor the effect of strain as the unsupported edge of the coil deflects under em loads.

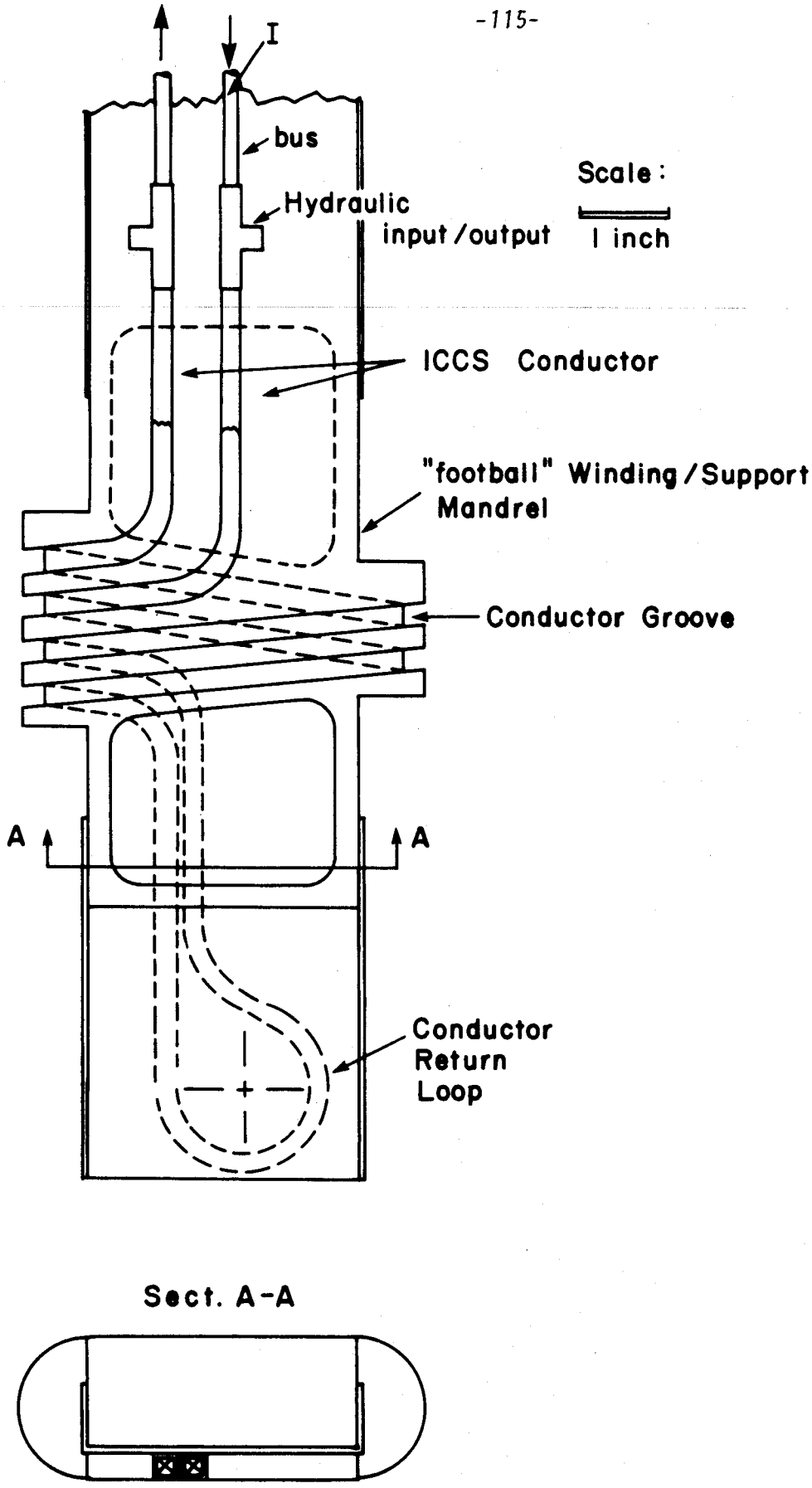

Figure 5.4 Outline of Mandrel for small football test.

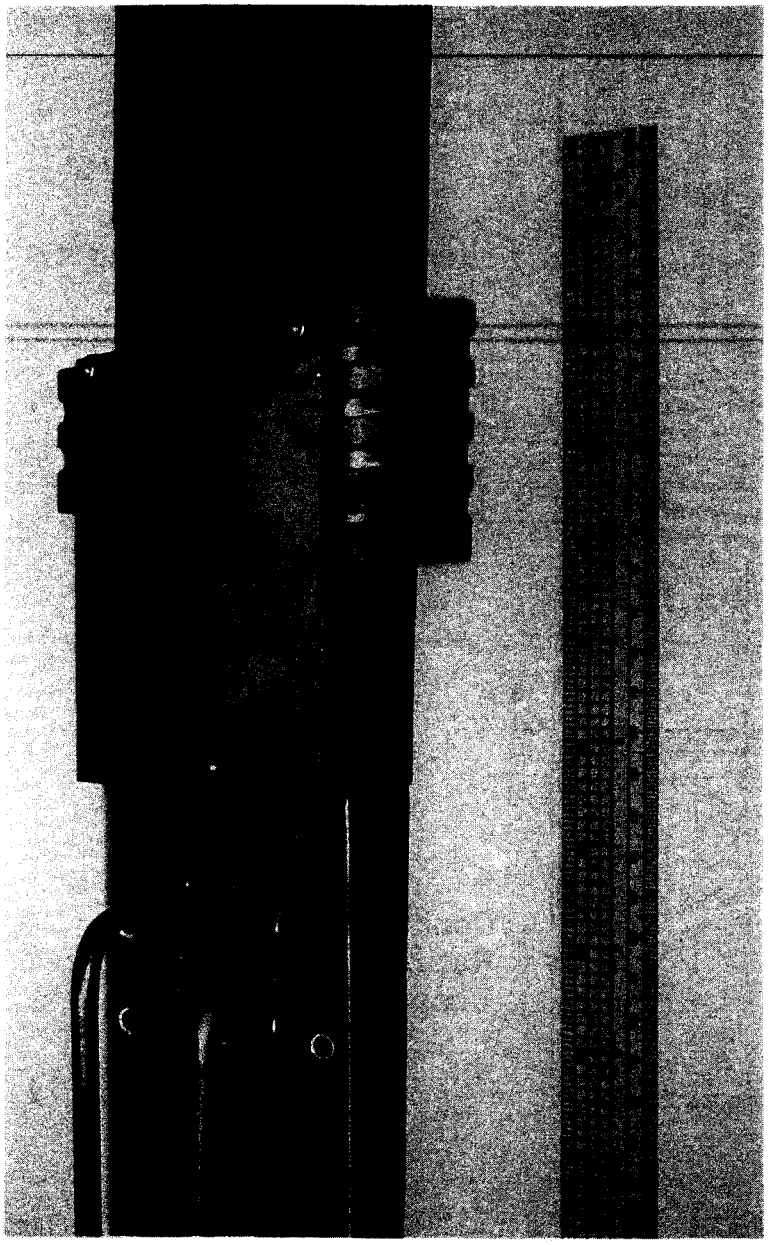

Figure 5.5 Photo of small football coil wound on mandrel with side support plates in place.

Piezoelectric acoustic emission sensors have been positioned at the center of the coil on the clamping plate and at the bottom of the sample holder. These will be used to detect conductor motion. A third pair of AE sensors may be added at the level of the buswork to the coil.

The coil is cooled both by internal helium within the sheath and by pool-cooling since the whole coil is placed in a Dewar within the 6B magnet which will provide background fields of 9, 10, and 11 T.

A small solenoid coil has also been wound of the same conductor. It will be used for stability tests.

Tests on these coils will begin in late October 1983.

Reference

1. M. Hong, I.W. Wu, J.W. Morris, Jr., W. Gilbert, W.V. Hassenzahl, C. Taylor, An Investigation on the enhancement of the critical current and densities in bronze-processed Nb_3Sn, Cryogenics, 23 435-444, 1983.

5.3 Hybrid Magnet Status Update - R.J. Thome

In last year's report we described a short circuit in the superconducting coil which is part of the 30 T Hybrid Magnet System at FBNML. Because of the well-cooled, highly stable nature (relatively low current density) of this coil, operations are not restricted provided the charge voltage is limited. Measured voltages at high and low charge rates were described last year and qualitatively predicted by computer analysis as part of this program in FY82.

During FY83, FBNML operations continued with the hybrid system. Several problems were encountered with the water cooled coil sections. These are traceable to the developmental nature of the advanced design of those segments and are studied and reported as part of the NSF activity which funds that program.

The superconducting magnet continued to operate as reported in FY82. It has logged approximately 300 hrs of operation and has experienced about 75 thermal cycles. The short circuit persists, but is not directly verified periodically. Its presence is inferred if the charge voltage is too high because the presence of the short causes voltage excursions beyond the compensation capability of the quench detection system and the protection circuit is triggered. The latter is prevented if the charge voltage is sufficiently low, which for this design, is still high enough so operations are not hampered.

Toward the end of FY83, the superconducting coil was being moved and one of the vacuum fittings to the vapor-cooled leads sprung a leak. In the process of removal, replacement and rewelding of the lead several voltage tap leads were severed. As a result, the main Dewar was opened

and leads repaired. Test results on the repaired system will be included in next year's report.

6.0 SAFETY RELATED ACTIVITIES

R.J. Thome

6.1 Joint MESA/MIT Safety Activity

MIT performed safety analyses this past year under a separate subcontract to MESA Corp. The prime contract was technically monitored by INEL and a separate report for this years activity is in preparation by MESA.

The activity focused on the LCTF at ORNL. The tasks performed by MIT were primarily concerned with short circuit analyses for the GE coil and participation in an evaluation of the protection circuits for the coils.

After construction, the coil wound by GE for the LCTF was found to have a short circuit across several turns by one of the instrumentation leads. Analyses performed under this program were able to show why earlier attempts to burnout the shorting wire failed and to specify the conditions necessary to burnout the short by either: (1) charging the main coil to a DC level and discharging it through a dump resistor or (2) applying AC power to the coil terminals. LCTF staff elected to use the latter method and successfully severed the shorting wire.

6.2 Japan/United States Workshop on Fusion Safety*

MIT participated in a joint Fusion Safety Workshop in Japan during January 24-27, 1983. This was performed under this program and involved a presentation

* "Proceeding of the Japan/United States Workshop on Fusion Safety", JAERI-Memorandum, 58-196 1983

1

on Superconducting Magnet Safety Issues and Research in the United States, participation in discussions on other workshop topics and tours of the Naka-site and Tokai-site fusion facilities of JAERI.